

**SYNTHESIS OF INTERMETALLICS AND CERAMICS  
WITH ULTRA-FINE MICROSTRUCTURES**

**FINAL PROGRESS REPORT**

**NARESH N. THADHANI**

**JUNE 1, 1997 TO NOVEMBER 30, 2000**

**U.S. ARMY RESEARCH OFFICE**

**GRANT NUMBER: DAAG55-97-1-0163**

**GEORGIA INSTITUTE OF TECHNOLOGY  
ATLANTA, GA 30332-0245**

**FEBRUARY 21, 2001**

**APPROVED FOR PUBLIC RELEASE;**

**DISTRIBUTION UNLIMITED**

**THE VIEW, OPINIONS, AND/OR FINDINGS CONTAINED IN THIS REPORT ARE  
THOSE OF THE AUTHORS(S) AND SHOULD NOT BE CONSTRUED AS AN  
OFFICIAL DEPARTMENT OF THE ARMY POSITION, POLICY, OR DECISION,  
UNLESS SO DESIGNATED BY OTHER DOCUMENTATION**

**20010409 106**

**REPORT DOCUMENTATION PAGE**Form Approved  
OMB NO. 0704-0188

Public Reporting burden for this collection of information is estimated to average 1 hour per response, including the time for reviewing instructions, searching existing data sources, gathering and maintaining the data needed, and completing and reviewing the collection of information. Send comment regarding this burden estimates or any other aspect of this collection of information, including suggestions for reducing this burden, to Washington Headquarters Services, Directorate for Information Operations and Reports, 1215 Jefferson Davis Highway, Suite 1204, Arlington, VA 22202-4302, and to the Office of Management and Budget, Paperwork Reduction Project (0704-0188,) Washington, DC 20503.

1. AGENCY USE ONLY (Leave Blank)

2. REPORT DATE  
February 15, 20013. REPORT TYPE AND DATES COVERED  
Final Technical Report, 6/1/1997 - 11/30/20004. TITLE AND SUBTITLE  
SYNTHESIS OF INTERMETALLICS & CERAMICS WITH ULTRA-FINE  
MICROSTRUCTURES5. FUNDING NUMBERS  
DAAG55-97-1-0163

6. AUTHOR(S)

Naresh N. Thadhani

7. PERFORMING ORGANIZATION NAME(S) AND ADDRESS(ES)

School of Materials Science and Engineering  
Georgia Institute of Technology  
Atlanta, GA 30332-02458. PERFORMING ORGANIZATION  
REPORT NUMBER

9. SPONSORING / MONITORING AGENCY NAME(S) AND ADDRESS(ES)

U. S. Army Research Office  
P.O. Box 12211  
Research Triangle Park, NC 27709-221110. SPONSORING / MONITORING  
AGENCY REPORT NUMBER

ARO 35591.2-MS

11. SUPPLEMENTARY NOTES

The views, opinions and/or findings contained in this report are those of the author(s) and should not be construed as an official Department of the Army position, policy or decision, unless so designated by other documentation.

12 a. DISTRIBUTION / AVAILABILITY STATEMENT

Approved for public release; distribution unlimited.

12 b. DISTRIBUTION CODE

13. ABSTRACT (Maximum 200 words)

The objective of our work has been to combine the beneficial effects of shock-compression of powders and solid-state structural and chemical changes for synthesis and fabrication of intermetallic alloys and ceramics with ultra-fine-grain microstructures. In particular, our research has focussed on studying the mechanisms and kinetics of shock-induced chemical reactions using simultaneous time-resolved stress and velocity measurements combined with shock recovery experiments. The possible shock-induced formation of otherwise difficult-to-synthesize carbon-nitride compounds has also been investigated. In addition, the reaction behavior of shock-compressed and subsequently activated powder mixtures has been investigated to determine its potential for synthesis of intermetallic alloys with highly refined microstructures. Finally, shock-compression has also been employed for fabrication of bulk compacts of nanocrystalline intermetallic alloys.

14. SUBJECT TERMS

shock-compression; shock synthesis; solid-state reaction synthesis; nanocrystalline intermetallics;  
shock compaction of powders; titanium silicides; molybdenum silicides; NiTi shape memory alloy;  
carbon-nitride

15. NUMBER OF PAGES

16. PRICE CODE

17. SECURITY CLASSIFICATION  
OR REPORT  
UNCLASSIFIED18. SECURITY CLASSIFICATION  
ON THIS PAGE  
UNCLASSIFIED19. SECURITY CLASSIFICATION  
OF ABSTRACT  
UNCLASSIFIED20. LIMITATION OF ABSTRACT  
UL

TABLE OF CONTENTS

A.	STATEMENT OF PROBLEM STUDIED	1
B.	BACKGROUND AND RATIONALE	2
C.	SUMMARY OF MOST IMPORTANT RESULTS	3
	C1. Shock-Induced Chemical Reactions in Mo-Si Powder Mixtures	3
	C2. Shock Synthesis Metastable $\beta$ -phase Carbon Nitride	5
	C3. Reaction Synthesis of Shock-Densified Ti-Si Powder Mixtures	6
	C4. Synthesis and Processing of Nanocrystalline Intermetallic Alloys	8
	C4.1 Nanocrystalline Titanium Silicide	8
	C4.2 Nanocrystalline Nickel Aluminide	9
	C4.3 Shape Memory NiTi Alloy	10
D.	INTERNATIONAL COLLABORATIONS	11
E.	DISSERTATIONS AND PUBLICATIONS	12
	E1. Graduate Thesis	12
	E2. List of Publications (Journals and Conference Proceedings)	12
F.	LIST OF PARTICIPATING SCIENTIFIC PERSONNEL	14
G.	HONORS AND AWARDS	14
H.	REFERENCES	14
I.	APPENDIX A – Re(pre)prints of Key Publications	15

## A. STATEMENT OF PROBLEM STUDIED

The objective of our work has been to combine the beneficial effects of shock-compression of powders and solid-state structural and chemical changes for synthesis and fabrication of intermetallic alloys and ceramics with ultra-fine-grain microstructures. In particular, our research has focussed on studying the mechanisms and kinetics of shock-induced chemical reactions using simultaneous time-resolved stress (with PVDF stress gauges) and velocity (with VISAR) measurements combined with shock recovery experiments. The possible shock-induced formation of otherwise difficult-to-synthesize carbon-nitride compounds has also been investigated. In addition, the reaction behavior of shock-compressed and subsequently activated powder mixtures has been investigated to determine the potential of this approach for synthesis of intermetallic alloys with highly refined microstructures. Finally, shock-compression has also been employed for fabrication of bulk compacts of nanocrystalline intermetallic alloys.

The results of this study indicate that "shock-induced" chemical reactions occurring in time scales of pressure equilibration, are most influenced by the crush-strength of the powders (stress at which full density is achieved), irrespective of the physical and thermal properties of reactants and products. Consequently, the reactions occur by solid-state mechanochemical mechanisms, at stresses much below those needed to cause melting of the precursor(s). In fact, the premature melting of a reactant during the powder crush-up process (e.g., melting of silicon in Mo-Si powder mixture) actually inhibits shock-induced reaction initiation. In such cases, powder mixtures can undergo post-shock or "shock-assisted" chemical reactions due to mean-bulk-temperature increases in time scales of temperature equilibration. Shock compression of sodium-dicyanamide mixed with sodium-azide and carbon-tetra-iodide powder precursors, shows synthesis of carbon nitride compound. Formation of the possible  $\beta$ -phase  $C_3N_4$  compound is inferred by diamond-like  $sp^3$  bonding between carbon and nitrogen atoms detected by electron energy loss spectroscopy, as well as an infra-red spectroscopy trace similar to that extrapolated from published spectrum of  $\beta$ - $Si_3N_4$ . Shock-densification of intermetallic-forming powder mixtures showed that the shock-compression approach can be used to generate a highly-activated dense-packed state of powders for subsequent reaction synthesis under controlled conditions. The reaction behavior of shock-densified Ti-Si powder mixture compacts at 5-7 GPa pressure, showed solid-state reaction synthesis at 1000°C leading to formation of single-phase  $Ti_5Si_3$  intermetallic alloys with higher than 99% density and less than 5  $\mu m$  grain size. A reaction synthesis model was developed to allow prediction of optimum conditions necessary to ensure that the reaction occurs by rapid solid-state diffusion and without being taken over by the combustion process. The model incorporates mass and heat balance, with the kinetics evaluated using experimentally determined apparent activation energies for solid-state and combustion reactions. Considering the decrease in activation energy (as measure of degree of shock activation), average particle size, and compact porosity, as the main variables, it was established that lowering the activation energy via shock-compression, influences the temperature above which the reaction may be taken over by the combustion-type process, and the overall time for reaction completion in the solid-state. Shock compression was also shown to be useful for fabrication of bulk compacts of nanocrystalline intermetallic alloy powders. While the nanocrystalline intermetallic alloy structure was retained following compaction and significant increases in hardness were attained, no increases in fracture toughness were observed. Nanocrystalline NiTi alloy also showed an increase in  $M_s$  temperature which is expected to influence its shape memory behavior.

## **B. BACKGROUND AND RATIONALE**

Shock-compression of powders (of elements, or their mechanical mixtures, or even compounds) is of interest due to possibilities of forming materials, either with non-equilibrium compositions and novel phases or with radically modified microstructures, resulting from the unique effects singularly possible by the shock-compression process [1-6]. While the former approach stems from the interest of synthesis of new high pressure phases, e.g.,  $C_3N_4$  or B-C-N [7,8], the latter approach can be used as an intermediate step to activate (or condition) the material for subsequent processing by conventional methods [5,6,9-11].

In shock synthesis experiments, powders are typically packed in solid containments at tap densities of ~40-50% TMD, or even statically pressed to green densities of ~50-85% TMD. Packed powders represent a configuration that is significantly different from that of distended (cellular) solids. Not only is the material highly porous (with ~15-60% void volume), but it also contains many particle-particle and void-particle contact interfaces. The shock-compression behavior of such highly-porous solids is thus, significantly different from that of solid-density or distended (cellular) solids, in that a large amount of extra energy is dissipated in plastic deformation and crushing of powders in the process of void annihilation [5]. Effective stresses at points of contact are significantly greater than the mean applied stress, which can lead to heterogeneous deformation and effects of shear localized at particle interfaces [2]. The high pressure, high-loading rates, and large amounts of strain, occurring during shock-compression of powders, generate an unusual combination of structural defects and powder packing characteristics [3]. The chemical reactivity of the constituents is also significantly enhanced, which can lead to the generation of a highly activated state and accelerated mass transport. Under such conditions, "shock-induced" physical and chemical changes can occur in powders (or their mixtures), leading to the formation of new phases or compounds during the high-pressure shock state [5]. Changes involving structural phase transformations have been proposed to initiate via electronic and displacive mechanisms, followed by reconstructive processes leading to completion of the phase change [12]. Shock-initiated chemical reactions, on the other hand, are less well understood and are believed to occur via mechanisms different from conventional formation and growth of nuclei from the liquid or the solid state [2,4]. The postulated mechanisms have included both solid-state [2-5] and liquid-state processes [13].

Instrumented experiments can be used to provide evidence of shock-initiated reactions, based on measurements of changes in properties (pressure or velocity) occurring during or immediately following the rise to peak pressure. However, no information about actual mechanisms involved in the reaction process, is revealed with simply instrumented experiments. Mechanistic information about the processes involved can be attained by microstructural characterization of recovered shock-compressed materials at conditions just below the threshold (initiation) conditions of reaction, since, once initiated, the resulting product often reveals characteristics of melting and re-solidification and no evidence of events leading to reaction initiation. Hence, a combination of instrumented and recovery experiments are essential to obtain a complete kinetic and mechanistic understanding of "shock-induced" chemical reactions [14].

During shock compression, powders undergo significant configurational changes [3], and intensive mixing of constituents [15] concomitant with the decrease in volume and densification to solid density. Processes responsible for such configurational changes and mixing, include shear-induced deformation and plastic flow, sliding at contact surfaces, and comminution and dispersion of the constituent(s) and fragments. XRD line broadening analysis of the shocked constituents [16] has shown high levels of retained plastic strain, corresponding to dislocation

densities of  $10^{13} \text{ cm}^{-2}$ , equivalent to those in heavily cold-rolled metals. The dense-packed and highly-activated state of the powder constituents, generated due to such processes, is expected to result in significantly increased reactivity of the material during subsequent thermal treatments, leading to accelerated kinetics of solid-state diffusion and phase formation [11].

In the following sections we summarize the most important results of our work which combines the beneficial effects of shock-compression of powders and solid-state structural and chemical changes for synthesis and fabrication of fine-grained intermetallics and ceramics.

- (a) mechanisms and kinetics of shock-induced chemical reactions in Mo-Si powder mixtures using simultaneous time-resolved measurements combined with shock recovery experiments;
- (b) possible shock-induced formation of otherwise difficult-to-synthesize  $\beta$ -phase carbon-nitride;
- (c) reaction behavior of shock-compressed and subsequently activated Ti-Si powder mixtures to determine the potential for synthesis of intermetallics with highly refined microstructures;
- (d) shock-compression of powders for fabrication of bulk compacts of nanocrystalline  $\text{Ti}_5\text{Si}_3$ , NiAl, and NiTi intermetallic alloys.

## **C. SUMMARY OF MOST IMPORTANT RESULTS**

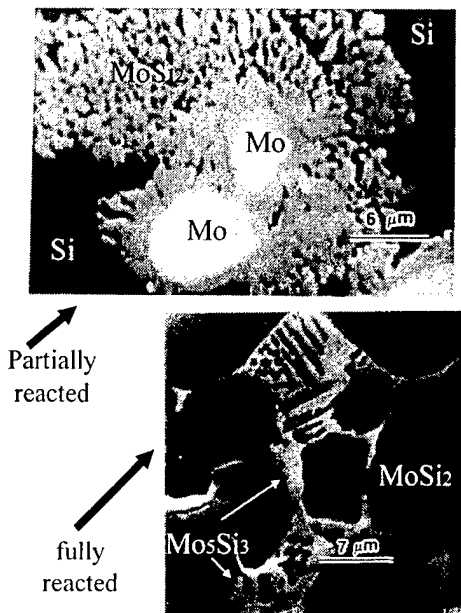
### **C.1. Shock-Induced Chemical Reactions In Mo-Si Powder Mixtures**

Chemical reactions occurring in Mo and Si powder mixtures under “shock-induced” (during the high-pressure shock state) and “shock-assisted” (subsequent to the shock event, but due to bulk temperature increases) conditions were investigated. Recovery experiments performed on Mo+2 Si powder mixtures employing cylindrical implosion geometry showed thermally initiated reactions yielding a mixed phase eutectic microstructure of  $\text{MoSi}_2$  and  $\text{Mo}_5\text{Si}_3$  in regions along the cylindrical axis, and partially-reacted surrounding region with  $\text{MoSi}_2$  spherules around molybdenum particles in a melted and solidified silicon matrix. Planar-pressure shock-recovery experiments showed a single phase  $\text{MoSi}_2$  microstructure formed due to a solid-state pressure-induced reaction process. Time-resolved instrumented gas-gun experiments performed on ~58% dense Mo+2Si powder mixtures, showed characteristics of powder densification and dispersed propagated-wave stress-profiles with rise-time  $>40 \text{ ns}$ , at input stresses less than 4 GPa (measured using poly-vinyl di-fluoride (PVDF) stress gauges). At input stress between 4-6 GPa, the powder mixtures showed propagated-wave stress-profiles having a sharp rise time ( $<10 \text{ ns}$ ), in addition to an expanded state of products revealing conclusive evidence of shock-induced reaction. At input stresses greater than 6 GPa, the powder mixtures showed a slower rise time and transition to a low-compressibility (melt) state indicating lack of shock-induced reaction. The results of this work indicate that (a) premature formation of a melt phase restricts mixing between reactants and inhibits “shock-induced” reaction initiation, although “shock-assisted” reactions can still occur in time scales of thermal equilibrium, and (b) the crush strength of powder mixtures is the most important parameter that controls initiation of a “shock-induced” reaction. Reaction synthesis experiments conducted on 55-95% dense Mo + 2 Si powder mixture compacts under an applied electric field showed that SHS reactions that would have normally become extinguished without the application of electric field, were observed to be self-sustained. Under such conditions, the reaction kinetics were observed to be enhanced and the reaction products showed a highly refined microstructure.

## SHOCK-INDUCED REACTIONS IN Mo-Si POWDERS

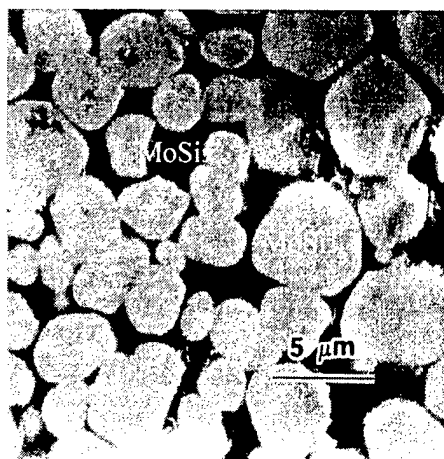
### Implosion Geometry

$P_{\text{bulk}} \sim 3.5\text{--}4\text{ GPa}$ ,  $P_{\text{axial}} \sim 13\text{--}15\text{ GPa}$   
 $T_{\text{bulk}} \sim 400^\circ\text{C}$ ,  $T_{\text{axial}} \sim 1500^\circ\text{C}$



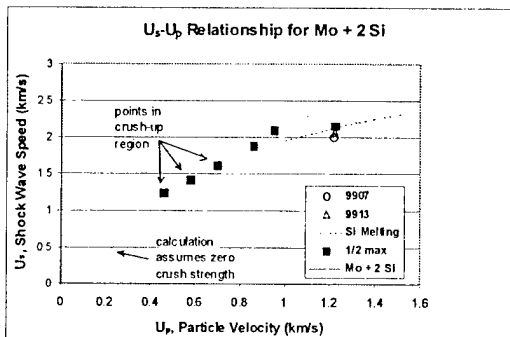
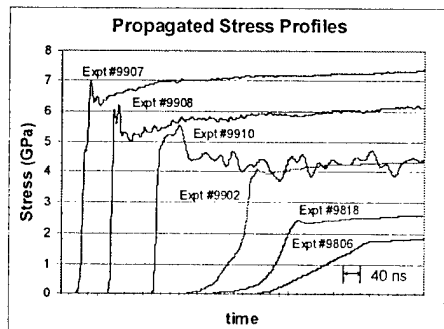
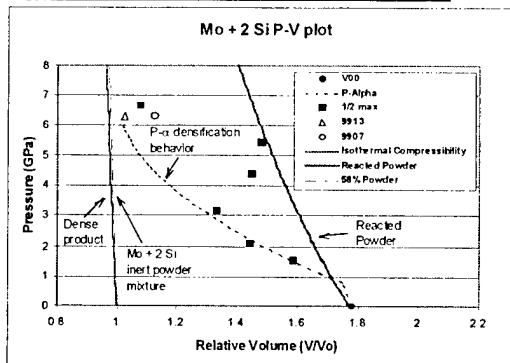
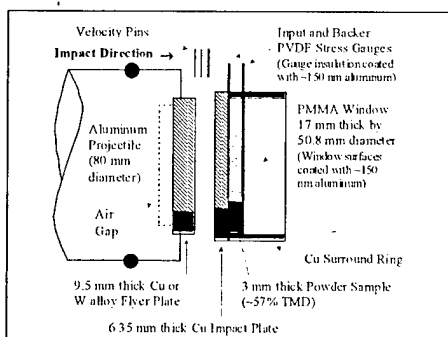
### Planar Pressure Geometry

$P_{\text{bulk}} \sim 22\text{ GPa}$ ,  $P_{\text{axial}} \sim 46\text{ GPa}$   
 $T_{\text{bulk}} \sim 400^\circ\text{C}$ ,  $T_{\text{edge}} \sim 650^\circ\text{C}$



Fully reacted  $\text{MoSi}_2 + \text{MoSi}_3$

## Time-Resolved Measurements of Shock-Induced Reactions in Mo-Si powders



## C2. Synthesis of $\beta$ - $C_3N_4$ By Shock-Compression of C-N Precursors

Synthesis of the theoretically predicted  $\beta$ -phase of carbon nitride ( $C_3N_4$ ) by shock compression of sodium dicyanamide mixed with sodium azides and carbon tetra-iodide was investigated. Shock-compression experiments were performed on the starting precursor blended with ~95 wt% Cu powder, statically pressed in steel capsules. The capsules were impacted under conditions of constant shock amplitude, but varying shock-pulse duration. Following shock-compression, the compacts were recovered by machining the steel capsules. Boiling concentrated nitric acid was used to dissolve the copper and product salts from the recovered shock-compressed material. Typical yields of residue recovered were ~50-100mg of fine black powder, collected by filtration on a fine glass frit. Implicit in this sample recovery procedure is the expected assumption that carbon nitride is insoluble in boiling concentrated nitric acid. The residue recovered from the shock-compressed samples after dissolving the copper and salts with acid treatment, was examined by transmission electron microscopy (TEM), energy dispersive spectroscopic (EDS) analysis, Parallel-detection Electron Energy Loss Spectroscopy (PEELS), and infra-red (IR) spectroscopy. TEM analysis showed crystallites of a cubic C-N compound dispersed in an amorphous matrix. Parallel-detection electron energy loss spectroscopy of the nitrogen-containing crystallites revealed diamond-like  $sp^3$  bonding, with N-content of ~8-13 at%. Infrared spectroscopy indicated absorption in the regions calculated to be appropriate to the  $\beta$ -phase  $C_3N_4$ . The synthesis of this possibly  $\beta$ -phase  $C_3N_4$  compound was observed to show increasing yield (based on increasing IR-peak intensity) in samples obtained from experiments performed with longer shock-pulse duration.

### SHOCK SYNTHESIS OF $\beta$ - $C_3N_4$ CARBON NITRIDE

Tetrahedral  $\beta$ - $C_3N_4$  - a predicted superhard material (Cohen, UC-B)

$$B = N_c/4 \{ (1971 - 220 \cdot I) / d^{3.5} \}$$

$N_c$  is coordination number = 3.43

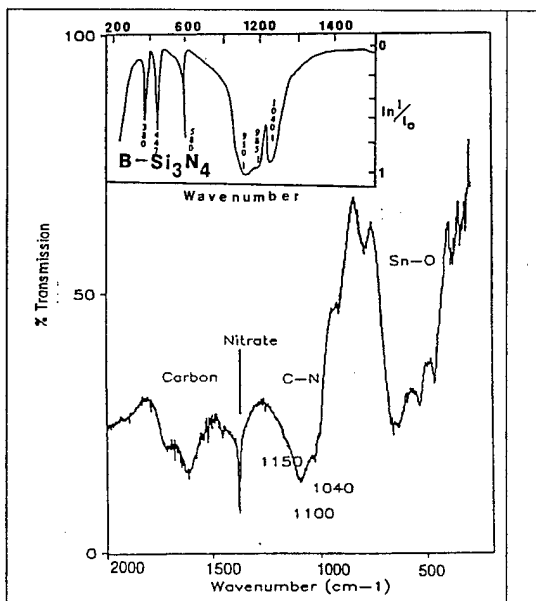
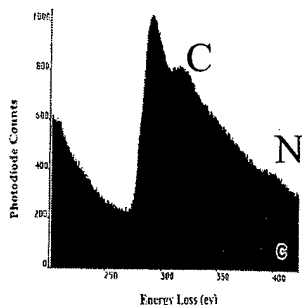
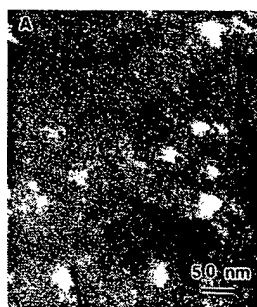
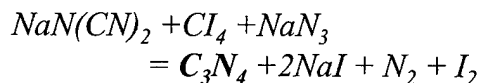
$d$  is bond length = 1.43 Å, and

$I$  is measure of ionicity = 0

Calc.  $\beta$ - $C_3N_4$  Bulk modulus = 419 GPa

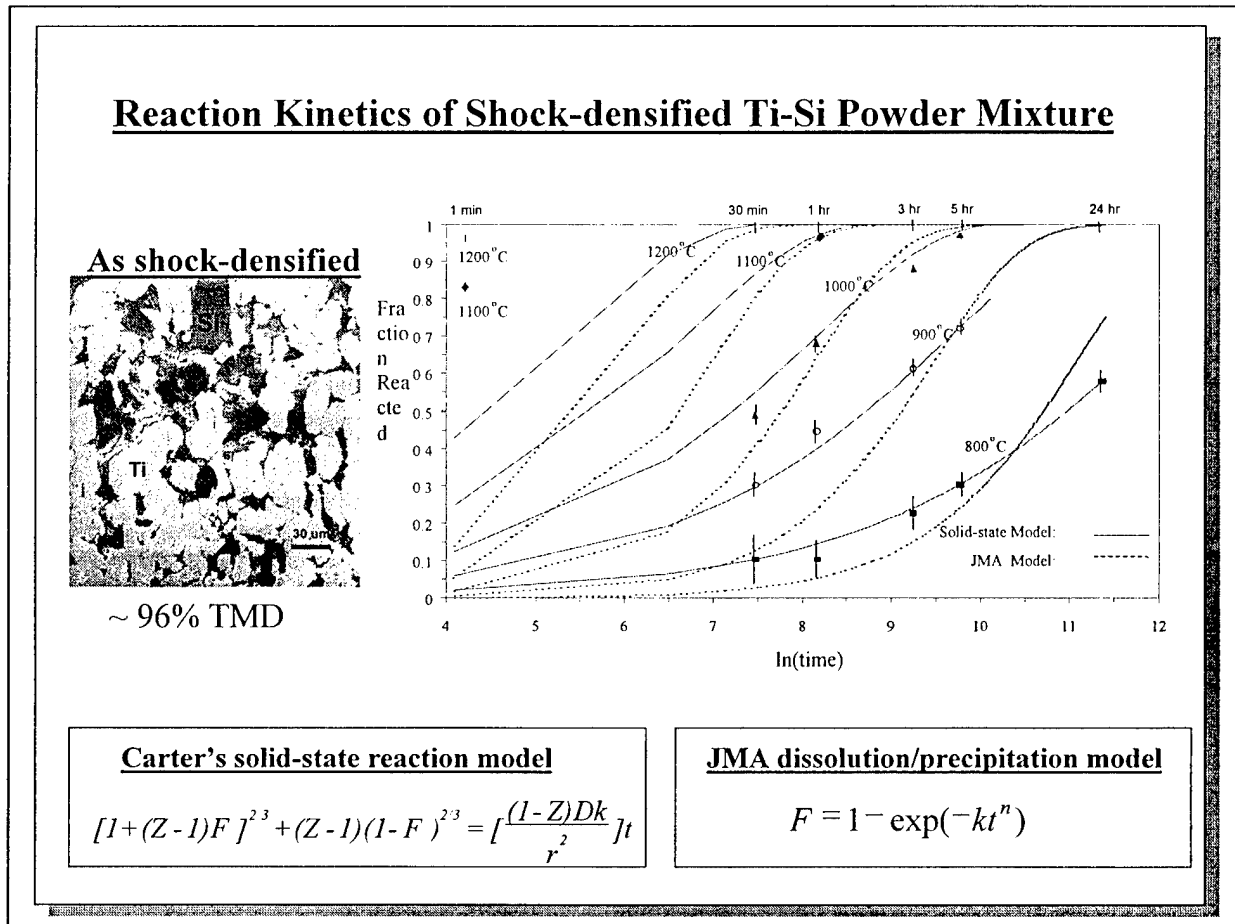
TEM/PEELS revealed K-edge absorptions of C at 292 ev and N at 401 ev, indicating  $sp^3$  diamond-like bonding.

$\beta$ - $C_3N_4$  phase evidenced by IR-spectroscopy based on correlation of IR-spectra of  $Si_3N_4$

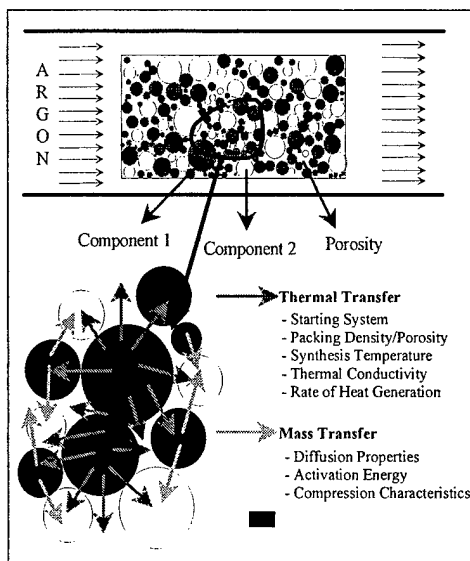


### C3. Reaction Synthesis of Shock-Densified Ti-Si Powder Mixtures

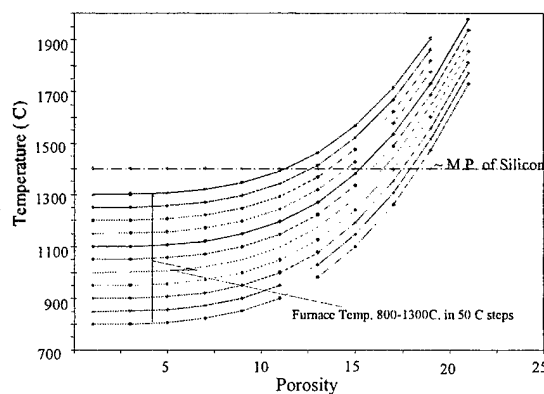
The reaction behavior of shock-consolidated Ti-Si powder mixture compacts, densified at 5-7 GPa pressure, was investigated to determine conditions required for solid-state reaction synthesis leading to formation of dense  $\text{Ti}_5\text{Si}_3$  intermetallic compound with fine-grained microstructure. It was observed that at temperatures greater than 1000°C, the heat released following reaction initiation in the solid-state exceeds the rate of heat dissipation causing a self-propagating combustion-type reaction to take over the synthesis process forming highly porous reaction products. A reaction synthesis model was developed to allow prediction of optimum conditions necessary to ensure that bulk of the reaction in dynamically-densified Ti-Si powder compacts, occurs by rapid solid-state diffusion and without being taken over by the combustion process. The model incorporates mass and heat balance, with the kinetics evaluated using experimentally determined apparent activation energies for solid-state and combustion reactions. Considering the decrease in activation energy (as measure of degree of shock activation), average particle size, and compact porosity, as the main variables, the model plots the fraction reacted as a function of time for various post-shock reaction-synthesis temperatures, illustrating the dominant reaction mechanism and kinetics. The results show that while changes in average particle size and compact porosity influence the synthesis temperature above which the reaction may be taken over by the combustion-type process, lowering of the activation energy via shock-compression, influences the time for reaction completion in the solid-state.



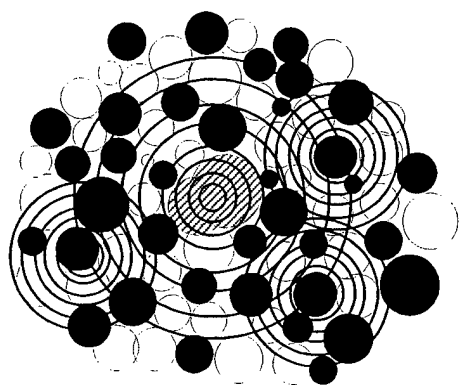
## THERMAL EQUILIBRIUM AND TEMPERATURE RISE



### Increase in temperature upon equilibration of heat of reaction



## REACTIONS IN SHOCK-DENSIFIED Ti-Si COMPACTS

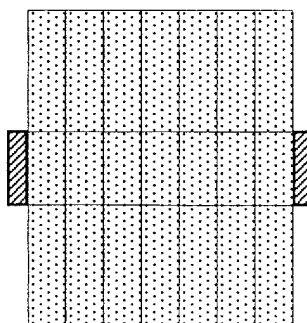


Generation and Redistribution of heat due to enhanced solid-State Diffusion

Product (hatched circle) Reactant A (open circle) Reactant B (solid black circle)

Product (hatched circle) Reactant Powder Layer (dotted circle)

Model used for calculation of temperature(s) due to the generation and redistribution of heat



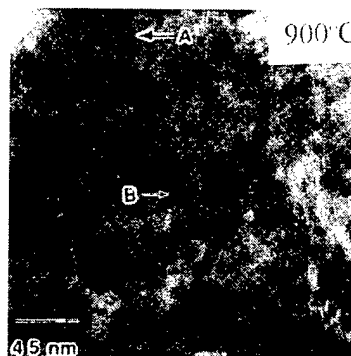
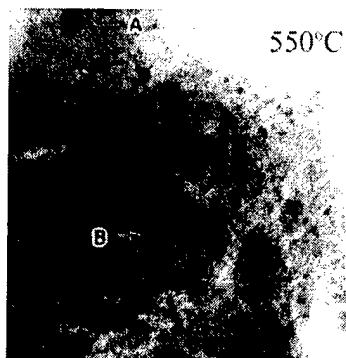
$$\frac{T_1 - T_o}{T_1 - T_o} = 2 \sum_{n=0}^{\infty} \frac{(-1)^n}{(n + \frac{1}{2})\pi} \exp\left[-\left(n + \frac{1}{2}\right)^2 \pi^2 \frac{\alpha t}{b^2}\right] \cos\left[\left(n + \frac{1}{2}\right) \frac{\pi y}{b}\right]$$

## C4. Synthesis of Nanocrystalline Intermetallic Alloys

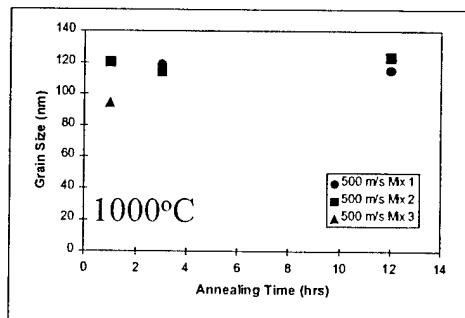
### C4.1 Nanocrystalline Titanium Silicide

Dynamic densification was used to consolidate mechanically amorphized Ti-Si alloy powders, using a 3-capsule, plate-impact, gas-gun loading system at velocities of 300, 500, and 700 m/s. The dense compacts were subsequently crystallized at annealing temperatures in the range of 800° to 1200°C, for time periods of 1 to 12 hours. The compacts were observed to crystallize to a typically single-phase  $\text{Ti}_5\text{Si}_3$  compound and an ultra-fine grain microstructure, based on TEM and XRD analysis. The average grain size changed from ~50 nm upon heat treatment at 800°C for 1 hr, to ~160 nm at 1200°C for 3 hrs, however, it remained stable (~115-125 nm) during annealing at a constant temperature of 1000°C and increasing heat treatment time from 1 to 12 hours. In-situ crystallization studies performed by heating the dynamically-densified samples in the TEM at temperatures up to 900°C, revealed that the increase in fraction of amorphous to crystalline phase was occurring by an increase in the number density of nucleating crystallites, and not via significant growth of existing crystallites since their growth is inhibited by the impingement of the crystals. Vickers microhardness measurements showed values of 1200-1400 kg/mm<sup>2</sup> for grain size ranging from ~60 to 160 nm. While these microhardness values are ~80% higher than those for microcrystalline shock-densified  $\text{Ti}_5\text{Si}_3$  alloy, the fracture toughness values measured using the indentation method were observed to be ~2-4 MPa√m, which is typical of that of brittle ceramics.

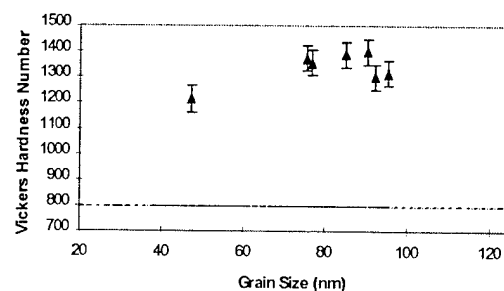
#### BULK NANOCRYSTALLINE $\text{Ti}_5\text{Si}_3$ INTERMETALLIC



*Crystallization of shock-densified alloy occurs via nucleation of new crystallites rather than growth of existing ones, forming single-phase nanocrystalline  $\text{Ti}_5\text{Si}_3$  alloy*



Crystallite size v/s annealing time

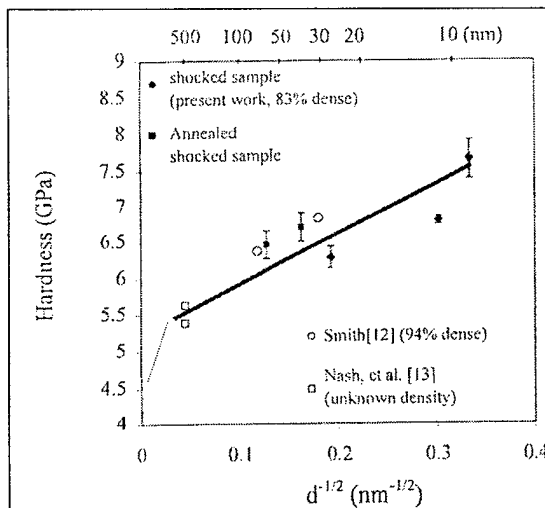


Vickers Hardness v/s Crystallite size

## C4.2 Nanocrystalline Nickel Aluminide

The synthesis, microstructural characterization, and strengthening mechanisms were studied in this work. Nanophase NiAl powders were prepared by mechanical alloying of elemental Ni and Al powders under an argon atmosphere for different times (0-48 h). The alloyed nanocrystalline powders were then consolidated by shock compaction at a peak pressure of 4-6 GPa, to 83% dense compacts. Characterization by transmission electron microscopy (TEM) revealed that the microstructure of the shock-consolidated sample was retained at the nanoscale. The average crystallite size measurements revealed that mechanically alloyed NiAl grain size decreased from  $48 \pm 27$  to  $9 \pm 3$  nm with increasing mechanical alloying time from 8 to 48 h. The long-range-order parameters of powders mechanically alloyed for different times were determined, and were observed to vary between 0.82 for 5 h and 0.63 for 48 h of milling time. Following shock compaction, the long-range-order parameter was determined to be 0.76, 0.69 and 0.66, respectively, for the 16, 24 and 48 h alloyed specimens. Both the mechanically alloyed nanocrystalline NiAl powder and the shock-consolidated bulk specimen showed evidence of grain boundary dislocations, subgrains, and distorted regions. A large number of grain boundaries and defects were observed via high resolution TEM (HRTEM). Shear bands were also observed in the mechanically alloyed NiAl intermetallic powders and in the shock-consolidated compacts. Microhardness measurements of shock-consolidated material showed increasing microhardness with increasing crystallite size refinement, following Hall-Petch behavior.

### STRENGTHENING MECHANISM IN SHOCK-CONSOLIDATED NANOCRYSTALLINE NiAl INTERMETALLIC ALLOY



#### NiAl Compact Characteristics

- B2 phase, 0.35-3.2 at%Fe
- Misfit elastic strain  $\epsilon = 15.2\%$
- $\tau_y = \{G \cdot \epsilon^{3/2} \cdot \sqrt{c}\} / 700 = 40$  MPa VHN
- Hall-Petch strengthening mechanism based on disl. generation at gb ledges

$$\sigma_y = \sigma_o + \alpha \mu b \left[ \frac{8m}{\pi d} \right]^{1/2}$$

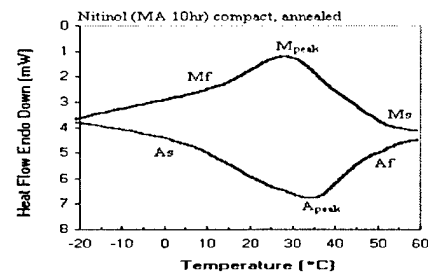
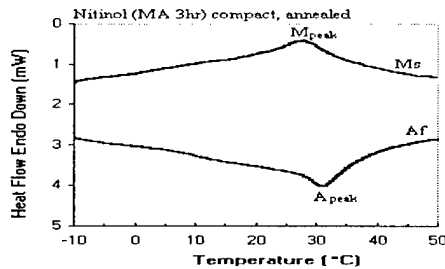
#### Hall-Petch Slope (Strengthening Mechanism)

9-70 nm = 7 GPa ( $\sqrt{\text{nm}}$ ) - (consistent w/ ledge model)

### C4.3 Shape Memory Nickel Titanium Alloy

In this study, the influence of nanocrystalline grain size on the shape memory behavior has been investigated. Nanocrystalline B2-phase NiTi alloys were synthesized by ball-milling Ni+Ti powder mixtures as well as pre-alloyed Nitinol alloy. The pre-alloyed Nitinol ( $\text{Ni}_{50.88}\text{Ti}_{49.12}$ ) powder was mechanically amorphized using a SPEX 8000 mixer/mill in an Ar atmosphere, and subsequently shock consolidated at 5-9 GPa and annealed to prepare compacts of bulk nanocrystalline alloy. With a reduced grain size in the nanometer range, the martensitic transformation start temperature ( $M_s$ ) was determined to increase. The increase in the martensitic transformation temperature in the nanocrystalline shock-consolidated samples, can be contributed to the reduction in grain size. Earlier work by other authors has reported an increase in  $M_s$  temperature with decreasing grain size in microcrystalline  $\text{Ni}_{48}\text{Ti}_{42}$  (weight percentage) alloy and Cu-Zn-Al alloys, respectively. The thermodynamics of martensitic transformation can be facilitated by local elastic energy. This local elastic energy is mainly due to the interaction between the newly formed martensitic plates and the grain boundaries. Since materials with smaller grains possess a larger portion of grain boundaries, it can be expected that there will be more local elastic energy between the martensitic plates and the grain boundaries. In addition, the degree of anisotropy also increases with decreasing grain size due to more different orientations of grains. Both factors contribute to greater internal stress, which assist the martensitic transformation and result in a higher  $M_s$  temperature for NiTi alloy with smaller grain size.

## **Transformation Temperatures**



Sample	Grain size	Cooling					Heating					
		$R_s$	$R_{peak}$	$M_s$	$M_{peak}$	$M_f$	$A_s$	$A_{peak}$	$A_{R_s}$	$A_{R_{peak}}$	$A_{R_f}$	$A_f$
As-received powder	$\sim 40 \mu\text{m}$	29	24	17	13	0	7	23	42	49	55	--
Annealed, shock consolidated MA 3hr compact	58nm	--	--	36	28	21	28	32	--	--	--	40
Annealed, shock consolidated MA 10hr compact	44nm	--	--	48	30	14	6	34	--	--	--	56

## **Thermodynamic Analysis**

Average Chemical Energy:  $\Delta H_{chem} = T_o \Delta S$

Average Entropy Variation:  $\Delta S = \frac{1}{2}(S_M + S_A)$

$$S_M = 2 * Q_M / (M_s + M_p) \text{ \& } S_A = 2 * Q_A / (A_s + A_p)$$

Equilibrium Temperature:  $T_o = \frac{1}{2}(M_s + A_p)$

Elastic Energy Increase:  $\Delta H_{el} = \Delta H_{chem} - Q$

$Q = \frac{1}{2}(Q_M + Q_A)$  = measured average heat absorbed

	T <sub>0</sub> (K)	Q (J/G)	ΔS (J/GK)	ΔH <sub>CH</sub> (J/G)	ΔH <sub>EL</sub> (J/G)
As-received unshocked	309	4.376	0.015	4.591	0.215*
BM -3hr SC	311	1.413	0.005	1.454	0.041
BM-10hr SC	325	0.909	0.003	0.971	0.063

\* Gil-mur and co-workers, 1995 -  $\Delta H_{el} \downarrow$  with grain growth (0.22-0.1 J/g)

### **D. INTERNATIONAL COLLABORATION**

We continue to maintain international collaboration with researchers at The University of Tokyo and Kumamoto University in Japan. As a result of this, we have had exchange of scientists at different levels and the principal investigators have made frequent visits to respective institutions to discuss about the latest developments in their research activities. Joint experiments have also being performed, making use of unique facilities of each institution. The collaboration with the University of Tokyo has involved interactions with Prof. Tatsuhiko Aizawa, who has developed unique facilities for rapid mechanical milling of powders, which is observed to show low threshold for shock-induced reaction synthesis. Our collaboration has included information exchange before results are published, defining of approaches to pursue common goals, and conducting shock-compression experiments performed using the Georgia Tech gas gun on powder mixtures prepared with the rapid milling set-up at the University of Tokyo. Collaboration with the Kumamoto University has involved exchange of scientists in addition to performing joint experiments. Dr. Tetsuyuki Hiroe, Professor, Department of Mechanical Engineering and Materials Science, Kumamoto University, spent the period from June 21 to August 14, 1999, at Georgia Tech, working on "Analysis of Dynamic Tensile Spall Strength of Al7075-T6 alloy."

## E.     DISERTATIONS AND PUBLICATIONS

### E1. DISSERTATIONS COMPLETED

1. Shantanu Namjoshi, "Reaction Synthesis of Dynamically-Densified Ti-Based Intermetallic and Ceramic Forming Powders," Ph.D. dissertation, Georgia Inst. of Tech., April 1999. *{currently Post-doctoral Research Fellow at Air Force Institute of Technology, WPAFB}*
2. Kevin Vandersall, "Investigation of Shock-Induced and Shock-Assisted Chemical Reactions in Mo-Si Powder Mixtures," Ph.D. dissertation, Georgia Inst. of Tech., December 1999. *{currently Post-doctoral Research Fellow Lawrence Livermore National Laboratory}*
3. Tao Chen, "Synthesis and Characterization of Mechanically Alloyed and Shock Consolidated Nanocrystalline NiAl Intermetallic Alloy," Ph.D. dissertation (partial support), Georgia Inst. of Tech., June 2000. *{currently Research Scientist at Delta Air Lines, Atlanta}*
4. Xiao Xu, "Shock Consolidation and Reaction Synthesis of Nanocrystalline NiTi Shape Memory Intermetallic Alloy," Ph.D. dissertation, Georgia Institute of Technology *{in progress – to be completed in Summer 2001}*.

### E2. LIST OF PUBLICATIONS

1. T. Aizawa and N.N. Thadhani, "Shock Synthesis of  $\text{MoSi}_2$  -  $\text{SiC}_p/\text{SiC}_w$  Composites from Mechanical Alloying Pretreated Precursors," Ceramic Trans., Vol. 94, 1998, pp. 273-284.
2. N.N. Thadhani, "Shock-Assisted Synthesis of  $\text{Ti}_5\text{Si}_3$  Intermetallic Compound," Journal of Materials Processing Technology, Elsevier, Vol. 85, 1998, pp. 74-78.
3. K. Vandersall and N.N. Thadhani, "Dynamic Densification of Mo-Si Powder Compacts and their Solid State Processing," in Proceedings of Shock Compression of Condensed Matter - 1997, eds. S.C. Schmidt, D.P. Dandekar, and J.W. Forbes, AIP - 1998, pp. 647-650.
4. K. Vandersall and N.N. Thadhani, "Shock-induced and Shock-assisted Reaction Product Formation in Shock-Compressed Mo-Si Powder Mixtures," in Proc. Of TMS Symposium on Molybdenum and its Alloys, TMS Meeting San Antonio, February 1998, 61-69.
5. T. Chen, J. Hampikian, and N.N. Thadhani, "Synthesis, Microstructure, and Properties of Shock Compacted Nanocrystalline NiAl alloy," Acta Mater., Vol. 47(8), 2567-2579, 1999.
6. A.H. Advani and N. N. Thadhani, "Shock-induced Reaction Synthesis of Isomorphous (Cu-Ni) And Immiscible (Cu-Nb) Compounds," Metallurgical and Materials Transactions, Vol. 30A, 1999, pp. 1367-1379.
7. P.J. Coughlin, A. Crawford, and N.N. Thadhani, "Influence of Dynamic Densification on Nanostructure Formation in  $\text{Ti}_5\text{Si}_3$  Intermetallic Alloy and Its Bulk Properties," Materials Science and Engineering, A267, pp. 26-35, 1999.
8. S.A. Namjoshi and N.N. Thadhani, "A Study of Reaction Kinetics in Dynamically Densified Ti-Si Powder Mixtures," Scripta Materialia, Vol. 40(12), pp. 1347-1352, 1999.
9. H.A. Grebe and N.N. Thadhani, "Influence of Dynamic Densification on Microstructure and Properties of Reaction Synthesized TiC Ceramic," J. Materials Synthesis & Processing, Vol. 7, No. 1, 1999, Kluwer Academic/Plenum Publ Corp New York NY USA, pp. 49-61

10. H. Xue, K. Vandersall, E Carrillo-Heian, N.N. Thadhani, and Z.A. Munir, "Initiation of Self-Propagating Combustion Waves in Dense Mo-2Si Reactants Through Field-Activation, J. American Ceramic Society, Vol. 82 (6), pp. 1441-46, 1999.
11. N.N. Thadhani, "Effects of Shock-compression of Powders on Materials Synthesis," in P/M: Research and Technology Briefs, P/M Science and Technology Briefs: The Latest Developments in Powder Metallurgy and Particulate Materials, edited by A. Bose, Metal Powder Industries Federation, Princeton, NJ, Vol. 1, No. 4, Nov 1999, pp. 26-30.
12. T. Chen, J.M. Hampikian, and N.N. Thadhani, "The Effect of Nanostructure on the Strengthening of NiAl," Mat. Res. Soc. Symp. Proc., No. 552, 1999, pp. KK8.3.1-KK8.3.5
13. N.N. Thadhani, "Materials Synthesis by Shock-Induced Chemical and Phase Changes," in Proc. of Workshop on Industrial Applications of Explosion, Shock-Wave, and High-Strain-Rate Phenomena, Kumamoto University, Japan, March 1999, pp. 1-6.
14. S.N. Namjoshi and N.N. Thadhani, "Modeling the Reaction Synthesis of Shock-densified Titanium-silicon Powder Mixture Compacts," Metallurgical and Materials Transactions, Vol. 31, No. 2, 2000, pp. 307-316..
15. Kevin Vandersall and N.N. Thadhani, "Time-Resolved Measurements of Shock-Induced Reactions in Mo-Si Powder Mixtures," in Shock-compression of Condensed Matter - 1999, Proceedings of APS Topical Group Meeting, eds. M.D. Furnish, L. Chabildas, and R. Hixson, AIP. -505, 2000, pp. 763-766.
16. N.N. Thadhani, T. Chen and J. Hampikian, Shock Compaction of Nanocrystalline NiAl Intermetallic and its Effect on Strengthening Mechanism," in Shock-compression of Condensed Matter - 1999, Proceedings of APS Topical Group Meeting, eds. M.D. Furnish, L. Chabildas, and R. Hixson, AIP - 505, 2000, pp. 733-736.
17. N.N. Thadhani, "Shock Compression Effects on Materials Synthesis," Proc. of Int. Conf. On High Pressure Science and Technology, AIRAPT - 17, eds. M. Manghanani, W. Nellis, and M. Nicol, 2000, pp. 233-236
18. X. Xu and N.N. Thadhani, "Synthesis of Nanocrystalline NiTi Shape Memory alloy, by Shock Consolidation of Mechanically Amorphized Nitinol Powder," in Ultrafine Grained Materials, eds. R.S. Mishra, et al., TMS, 2000, pp. 23-32.
19. C. Collins, N. Thadhani and Z. Iqbal, "Possible synthesis of beta-C<sub>3</sub>N<sub>4</sub> by shock-compression of C-N precursors," CARBON, 2001, **in press**.
20. N.N. Thadhani, "Mechanochemical Synthesis of Intermetallic Compounds," in Intermetallic Compounds: Principles, Processes, and Applications, eds. J.H. Westbrook and R. Fleischer, John Wiley and Sons, **in press** (to be published in April 2001).
21. X. Xu and N.N. Thadhani , "Synthesis and Characterization of Nanocrystalline NiTi Shape-Memory Alloy by Shock Compression," in Proceeding of EXPLOMET - 2000, Metallurgical and Materials Applications of Shock Waves and High Strain Rate Phenomena, eds., K.P. Staudhammer, L.E. Murr, and M.A. Meyers, 2001, **(in press)**.
22. K. S. Vandersall and N. N. Thadhani, "Investigation of shock-induced chemical reactions in Mo-Si powder mixtures," in Proceeding of EXPLOMET - 2000, Metallurgical and Materials Applications of Shock Waves and High Strain Rate Phenomena, eds., K.P. Staudhammer, L.E. Murr, and M.A. Meyers, 2001, **(in press)**.
23. X. Xu and N.N. Thadhani, "Shock Synthesis and Characterization of Ultrafine Grained NiTi Shape Memory Alloy," Scripta Materialia, 2001 **(in press)**.

## **F. LIST OF PERSONNEL SUPPORTED**

Faculty: Prof. Naresh N. Thadhani  
Tech.: Rod Russell (Research Technician/MSE)  
Grad Studts: Shantanu Namjoshi (Ph.D'99/MSE), Kevin Vandersall (Ph.D'99/MSE), and  
Xiao (Chris) Xu (Ph.D./MSE)  
UG Stud: Alice Crawford (Physics) and Andy Gapin (MSE)

## **G. HONORS AND AWARDS**

- Kevin Vandersall received outstanding GRA/GTA awards at Georgia Tech, 1998, 1999.
- Naresh Thadhani, promotion to Full Professor in MSE at Georgia Tech, 1999.
- Naresh Thadhani, elected Fellow of ASM International, October 2000

## **H. REFERENCES**

- [1]. G. Duvall, Chairman, *National Materials Advisory Board Report No. 414*, National Academy Press, Washington D.C., 1984.
- [2]. A. N. Dremin and O.N. Breusov, *Russian Chemical Reviews*, **37** (5), 392-402 (1968).
- [3]. R.A. Graham, in *Proc. of 3rd International Symposium on High Dynamic Pressures*, edited by R. Charet, Assoc. Francaise de Pyrotechnie, Paris, 1989, pp. 175-180.
- [4]. N.N. Thadhani, *Progress in Materials Science*, **37** (2), 117-226, (1993).
- [5]. N.N. Thadhani, *J. Appl. Phys.*, **76**, 2125-38 (1994) .
- [6]. R.A. Graham and N.N. Thadhani, in *Shock Waves in Materials Science*, ed., A.B. Sawaoka, SpringerVerlag, 1993, pp. 35-65.
- [7]. C. Collins and N.N. Thadhani, in *Processing and Fabrication of Advanced Materials V*, TMS, 1996, pp. 569-579.
- [8]. T. Komatsu, Y. Kakudate, S. Fujiwara, *J. Mater. Chem.*, **6** (1996) 5067.
- [9]. J. Barrington and O.R. Bergmann, *J. Amer. Ceram. Soc.*, **49** (1966) 502.
- [10]. E.K. Beauchamp and M.J. Carr, *J. Amer. Ceram. Soc.*, **73** (1990) 49.
- [11]. J.-H. Lee and N.N. Thadhani, *Journal of Materials Research*, Vol. 3, No. 11, 1998, pp. 3160-3173.
- [12]. Y. Syono, K. Kusaba, T. Atou, and K. Fukuoka, "Phase Changes in Solids during Shock Loading and Unloading," in *Shock Waves*, Proceedings of 18<sup>th</sup> International Symposium on Shock Waves, Sendai, Japan, 21026, 1991, ed. K. Takayama, Springer Verlag, pp. 121-128.
- [13]. M. A. Meyers, K. S. Vecchio, Li-Hsing Yu, *Acta Metall. Mater.* **42**, 701-714 (1994), and 715-729 (1994).
- [14]. N.N. Thadhani, R.A. Graham, T. Royal, E. Dunbar, M.U. Anderson, and G.T. Holman, "Shock-induced Chemical Reactions in Ti-Si Powders of Different Morphologies: Time-Resolved Measurements & Materials Analysis," *J. of Appl. Phys.*, **82**(3), 1997, pp. 1113-1128.
- [15]. B. Morosin and R.A. Graham, *Mat. Sci. and Eng.*, **66**, 73-87, (1984).
- [16]. A.H. Advani and N. N. Thadhani, *Metall. and Matls. Trans.*, **30A**, (1999) 1367.

## APPENDIX A - RE(PRE)PRINTS OF KEY PUBLICATIONS

- A1. K. S. Vandersall and N. N. Thadhani, "Investigation of shock-induced chemical reactions in Mo-Si powder mixtures," in Proceeding of EXPLOMET – 2000, Metallurgical and Materials Applications of Shock Waves and High Strain Rate Phenomena, eds., K.P. Staudhammer, L.E. Murr, and M.A. Meyers, 2001, **(in press)**.
- A2. C. Collins, N. Thadhani and Z. Iqbal, "Possible synthesis of beta-C<sub>3</sub>N<sub>4</sub> by shock-compression of C-N precursors," CARBON, 2001, **in press**.
- A3. S.N. Namjoshi and N.N. Thadhani, "Modeling the Reaction Synthesis of Shock-densified Titanium-silicon Powder Mixture Compacts," Metallurgical and Materials Transactions, Vol. 31, No. 2, 2000, pp. 307-316.
- A4. P.J. Coughlin, A. Crawford, and N.N. Thadhani, "Influence of Dynamic Densification on Nanostructure Formation in Ti<sub>5</sub>Si<sub>3</sub> Intermetallic Alloy and Its Bulk Properties," Materials Science and Engineering, A267, pp. 26-35, 1999.
- A5. T. Chen, J. Hampikian, and N.N. Thadhani, "Synthesis, Microstructure, and Properties of Shock Compacted Nanocrystalline NiAl alloy," Acta Mater., Vol. 47(8), 2567-2579, 1999.
- A6. X. Xu and N.N. Thadhani, "Shock Synthesis and Characterization of Ultrafine Grained NiTi Shape Memory Alloy," Scripta Materialia, 2001 **(in press)**.

## **APPENDIX A1 - PREPRINT**

K. S. Vandersall and N. N. Thadhani, “Investigation of shock-induced chemical reactions in Mo-Si powder mixtures,” in Proceeding of EXPLOMET – 2000, Metallurgical and Materials Applications of Shock Waves and High Strain Rate Phenomena, eds., K.P. Staudhammer, L.E. Murr, and M.A. Meyers, 2001, **(in press)**.

{To be published in Proceeding of EXPLOMET – 2000, Metallurgical and Materials Applications of Shock Waves and High Strain Rate Phenomena, eds., K.P. Staudhammer, L.E. Murr, and M.A. Meyers, 2001, (in press)}.

## **Investigation of shock-induced chemical reactions in Mo-Si powder mixtures**

Kevin S. Vandersall and Naresh N. Thadhani

School of Materials Science and Engineering, Georgia Institute of Technology, Atlanta, GA 30332-0245.

Shock-induced chemical reactions in ~58% dense Mo+2Si powder mixtures were investigated using time-resolved instrumented experiments, employing PVDF-piezoelectric stress gauges placed at the front and rear surfaces of the powders to measure the input and propagated stresses, and wave speed through the powder mixture. Experiments performed on the powders at input stresses less than 4 GPa, showed characteristics of powder densification and dispersed propagated wave stress profiles with rise time  $> \sim 40$  nanoseconds. At input stress between 4-6 GPa, the powder mixtures showed a sharp rise time ( $< \sim 10$  ns) of propagated wave profile and an expanded state of products revealing evidence of shock-induced chemical reaction. At input stresses greater than 6 GPa, the powder mixtures showed a slower propagated-stress-wave rise time and transition to a low-compressibility (melt) state indicating lack of shock-induced reaction. The results illustrate that premature melting of silicon, at input stresses less than the crush-strength of the powder mixtures, restricts mixing between reactants and inhibits "shock-induced" reaction initiation.

### **1. INTRODUCTION**

The propagation of shock waves in powder mixtures can introduce physical, chemical, and physiochemical changes in time scales of the peak pressure state (of microsecond duration) [1]. These "shock-induced" [2] changes result in the formation of metastable phases, non-equilibrium compounds, or simply radically modified microstructures and are of interest in applications relevant to synthesis of ceramics and intermetallic compounds.

The Mo-Si system is an interesting intermetallic-forming powder mixture system for study of shock chemistry, because of large differences in properties of the constituents (e.g., density, sound speed, yield strength, and melt temperature), and a high heat of reaction. Prior shock synthesis studies on Mo-Si have been performed by Meyers et. al. [3-4], Marquis and Batsanov [5], Montilla [6] and Aizawa et. al. [7], in which reaction products having a variety of microstructures have been observed. While, the microstructures provide possible evidence of how the product phase may have been formed, it is difficult to ascertain whether the phases were formed due to "shock-induced" reactions in time scales of pressure equilibrium, or subsequent to the shock event in time scales of temperature equilibrium via "shock-assisted" processes [2]. Inference of "shock-induced"

chemical reactions can only be obtained via in-situ measurements of shock-properties using time-resolved experiments [8-13]. In the present work instrumented experiments employing PVDF stress gages were used to study the reaction behavior during shock compression of Mo+2Si powder mixtures. This work follows a series of recovery experiments, the results of which are explained elsewhere [14].

### **2. EXPERIMENTAL PROCEDURE**

Molybdenum (Cerac No. M2000) and Silicon (Cerac No. S1053) powders ( $\sim 325$  mesh,  $< 44 \mu\text{m}$ ) were mixed in a stoichiometric ratio corresponding to  $\text{MoSi}_2$  (using a mechanical V-blender) and pressed into fixtures at a density of  $\sim 58\%$  TMD. The experimental setup for the instrumented experiments is shown schematically in Figure 1 [15]. PVDF piezoelectric stress gauges were placed in intimate contact with front and back powder-capsule planar surfaces to monitor both "input-shock" and "propagated-wave" characteristics. The propagation of the shock wave sensed by the "input" gauge and "propagated" gauge at their respective locations, also provided precise data of the transit time through the  $\sim 3$  mm thick (50.8 mm diameter) powder-mixture samples. OFHC-copper flyer plates were used for experiments #9806, #9818, and #9902 and a tungsten alloy (MIL-T-21014) flyer plate was used in all other

Table 1  
Summary of results

Expt. No.	Packing Density (g/cm <sup>3</sup> , %TMD)	Projectile Velocity (mm/μs)	Input Stress (GPa)	Input Risetime (ns) (10%-90%)	Equilibrium Propagated Stress (GPa)	Propagated Risetime (ns) (10%-90%)	Wave Speed (mm/μs) (toe-toe-10%, ½ max)	Relative Volume (toe-toe-10%, ½ max)
9806	2.59, 57	0.507	1.52	11.5	1.82	186	1.28, 1.23	1.58, 1.50
9818	2.50, 55	0.700	2.09	7.5	2.36	86	1.43, 1.41	1.43, 1.39
9902	2.69, 59	0.964	3.15	6.5	3.95	76.5	1.66, 1.61	1.13, 1.08
9910	2.70, 59	0.851	4.36	8.5	4.29	10, 14†	1.87, 1.87	1.46, 1.45
9908	2.71, 59	0.940	5.4	4.5	5.18	6	2.10, 2.10	1.55, 1.55
9907	2.71, 59	0.966	6.3*	‡	6.16	8, 7†	1.99*	1.13*
9913	2.50, 55	0.967	6.3*	‡	5.07	22.5	2.07+	1.02
9919	2.51, 55	0.914	6.65	5	4.74	25.5	2.17, 2.15	1.10, 1.08

\* indicates a calculated value, ‡ indicates no measurement obtained, † indicates a two slope wave structure, + indicates toe-to-toe at shock arrival instead of 10%

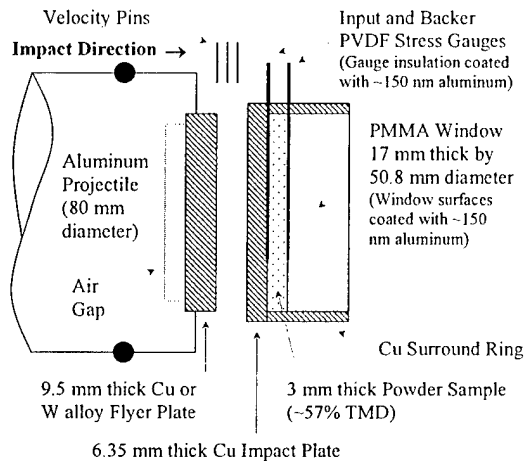


Figure 1. Schematic showing the experimental setup used.

experiments for generating higher pressures. The projectile velocity was measured using shorting pins, spaced 12.7 mm apart and the digital oscilloscopes were triggered from standoff pins placed 6.35 mm from the impact surface. It should be noted that the loading geometry is such that in all experiments a planar-parallel shock wave propagates through the powders without longitudinal or radial attenuation.

### 3. RESULTS AND DISCUSSION

A summary of the experimentally determined parameters obtained from the instrumented experiments is listed in Table 1. These

include, the input stress and the input pulse rise-time (from 10% to 90% of peak) measured by the input shock gauge; the equilibrated propagated stress and propagated pulse rise-time recorded by the propagated stress gauge; wave speed determined based on the travel time through the powder layer (with time through gauge insulation subtracted), using both the toe-to-toe and half-max values of input- and propagated-wave profiles; the relative volume calculated using the values of initial powder density, measured input stress, shock wave speed (both toe-to-toe and ½ max), and shock jump conditions for conservation of mass and momentum.

A plot displaying the measured input-stress profiles from all experiments is included in Figure 2. The propagated stress traces for all three low velocity experiments are provided in Figure 3 (a) and the remaining traces from the higher velocity experiments are shown Figure 3 (b). The varying amplitudes of the different input-stress profiles correspond to experiments performed at different impact velocities. It can be clearly seen that the rise time of the input stress pulse is less than 10 ns under all impact conditions. In contrast, the propagated stress wave shows effects of wave dispersion, with rise time varying between 6 to 186 ns. The lower amplitude stress waves show the longest rise time, indicating the behavior being dominated by powder densification at low-pressure.

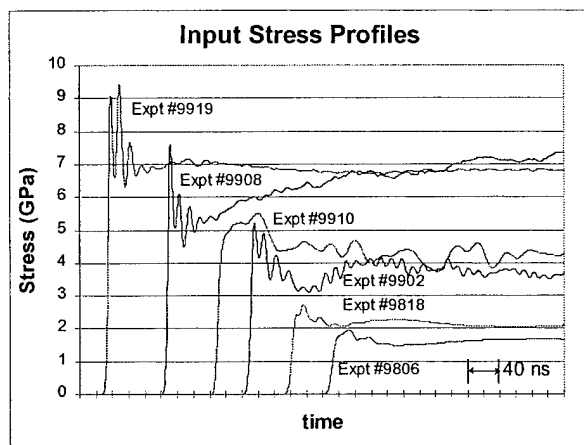


Figure 2. Combined plot of input stress traces.

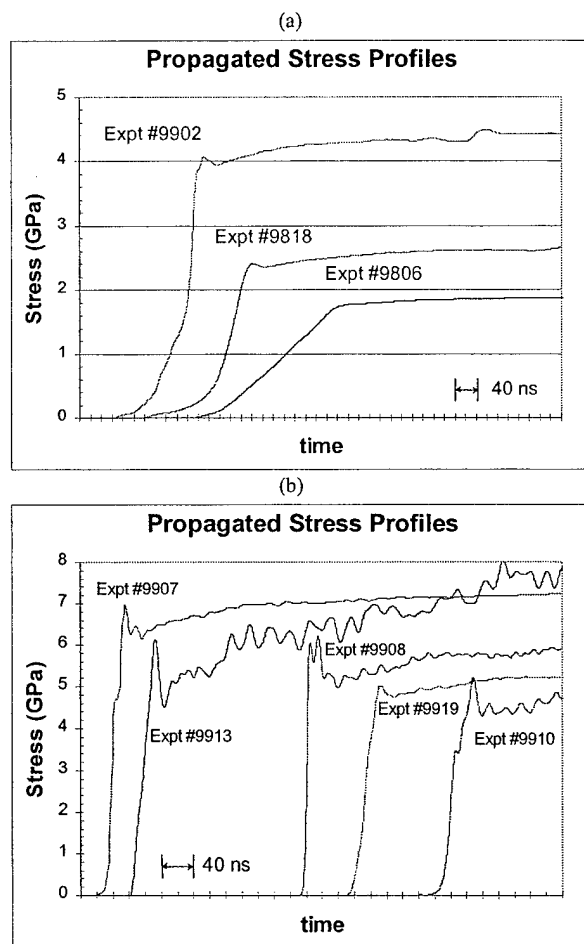


Figure 3. Propagated stress traces for (a) three low velocity experiments and (b) higher velocity experiments.

### 3.1 Pressure Volume Compressibility Behavior

Since the stress pulses propagating through the 3 mm thick powder mixtures have a structure characteristic of wave-dispersion effects (as observed in Figure 3 and 4), calculation of the relative volume based on jump conditions applied to a steady-state shock wave, may not be completely appropriate. However, given the very large compression achieved with such porous materials, one can use the calculated relative volume along with measured input stress to obtain first-order effects of shock-compression of Mo + 2Si powder mixtures.

The plot of measured input stress as a function of calculated relative volume for the Mo + 2Si powder mixture is shown in Figure 4 (a). Data corresponding to the measured input stress versus wave speed (based on toe-to-toe and half-max values) is plotted in Figure 4 (b). The two sets of data points for each pressure correspond to relative volumes calculated using the two values of the wave speeds based on toe-to-toe and one-half max measurements. The data point corresponding to the initial relative volume of the powder, and the calculated Hugoniot compressibility curve of solid density Mo + 2 Si, are also indicated in the plot. Calculation of the mixture Hugoniot [10], considers densification of the Mo + 2 Si powder from  $V/V_0=1.78$  to  $V/V_0=1$ , occurring at practically zero stress, in other words the Hugoniot calculation assumes that the crush strength of the powder mixture is zero.

The crush strength represents the stress at which the powder mixture constituents compress to solid density. Even metallic powders are expected to have a non-zero crush strength. It is during this process of powder crush up to full density, that a configuration of extensively deformed, intimately mixed, and highly activated state of reactants is generated. Consequently, at pressures approaching the crush strength, reactive powder mixtures can undergo shock-induced chemical reactions. Occurrence of such reactions in highly exothermic material systems, which result in generation of high temperature in the process of compound formation, would be expected to show evidence of reaction in the overall pressure-volume compressibility behavior.

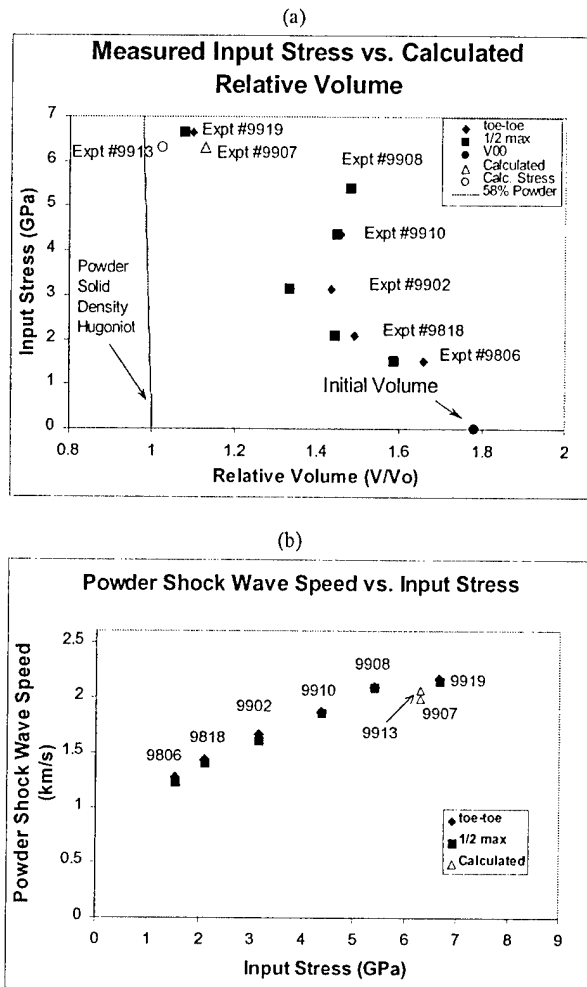


Figure 4. Plots of (a) measured input stress versus calculated relative volume and (b) measured input stress as a function of powder wave speed, for Mo + 2 Si powder mixture. Solid line at relative volume of 1, indicates the calculated powder Hugoniot for the 58% dense Mo + 2 Si mixture. Data for Experiment #9907 based on calculated values of wave speed and input stress and that for Experiment #9913 based on calculated value of input stress and measured wave speed.

The input stress versus relative volume plot in Figure 4 (a) shows clusters of data points illustrating three different (possible) trends. Hence, a single curve cannot be used to fit the data points to illustrate the overall compressibility behavior. To obtain clear distinction between the different regions corresponding to the different clusters of data points, calculations of (a) crush-up or powder densification behavior and (b) the shock-induced reaction product Hugoniot, were performed and fit with the experimentally obtained data points. The results of

the calculations and their fit with the measured data points (re-plotted with just the half-max values) are shown in Figure 5.

#### (a) Powder Crush-up Behavior

Densification of the powder mixture from an initial to final solid density was considered first, using the P- $\alpha$  pore collapse model [16]. The P- $\alpha$  model uses a distension parameter  $\alpha$  defined by:  $\alpha = V/V_s$ , where  $V$  is the specific volume of porous material and  $V_s$  is the specific volume of the solid.

Accordingly, the P- $\alpha$  model is expressed by the equation given below [16]:

$$\alpha = 1 + (\alpha_p - 1) \left[ (P_s - P) / (P_s - P_E) \right]^p \quad (1)$$

where  $\alpha_p$  is the density achieved during elastic compression,  $P_E$  is the pressure where elastic compression is observed, and  $P_s$  is the crush strength. Because the P- $\alpha$  model is rather empirical, the parameters  $\alpha_p$ ,  $P_E$ , and  $P_s$  were adjusted to best fit the experimentally obtained data. Figure 5 displays the P- $\alpha$  model curve superimposed to fit the three low pressure data points on the P-V curve for Mo + 2Si. The value of  $P_E$  was found to be 0.8 GPa,  $\alpha_p$  was 1.75, and  $P_s$  (for 99% densification) was ~6 GPa for the best fit of the P- $\alpha$  densification curve to the three data points. It can be seen that the model becomes rather asymptotic close to the solid density and leads to an over estimate of the crush strength. A more realistic value of the crush strength was then considered to be at ~99% final density, which yields a crush strength of ~6 GPa for 58% dense Mo + 2 Si powder mixtures, as illustrated in Figure 5.

#### (b) Calculation of Reaction Product Hugoniot

Fitting the three low-stress data points with the crush up behavior modeled on the basis of the P- $\alpha$  powder densification model leaves two sets of higher-pressure data points that do not fall on the crush-up path. One set of two data points (4-6 GPa) shows a highly expanded state and the other set of data ( $P > 6$  GPa) shows behavior following that of unreacted (inert) Mo + 2 Si powder mixtures. Prior work on powder mixtures of Ti-Si [8] and Sn-S [9], attributed the expansion to a shock-induced reaction resulting in generation of high temperature and consequent volume increase. As mentioned earlier, the possibility of shock initiation of reaction would

be most favorable during densification in the process of crush up to full density. The resulting volume expansion due to reaction would be expected to depend on the exothermicity of the system, the volume change between reactants of products, and the degree of reaction occurring during the shock state. Hence, it was desired to calculate a pressure-volume curve for a fully reacted  $\text{MoSi}_2$  product formed during shock-compression of 58% dense Mo + 2 Si powder mixture.

A thermodynamic consideration was used to generate the pressure-volume (Hugoniot) curve of a fully reacted  $\text{MoSi}_2$  product, based on the model recently developed by Bennett and Horie [17], based on a constant pressure adjustment of the reference state. The important concept of this analysis is that it actually determines a calculated Hugoniot of the products formed via "shock-induced" reaction in a powder mixture.

Figure 5 shows the pressure-volume space with the calculated curves representing the P- $\alpha$  densification behavior and the pressure-volume data points obtained from the PVDF gauge experiments, re-plotted with the calculated compressibility curve of the fully reacted  $\text{MoSi}_2$  product formed from Mo + 2Si reactants at ~58% density. It can be seen that while the cluster of the three data points at pressures less than 3.1 GPa follow the trend representing the P- $\alpha$  densification behavior (as described earlier), the two data points at 4.3 and 5.3 GPa show significant expansion as they approach the fully reacted powder (forming  $\text{MoSi}_2$  product) Hugoniot curve. Hence, it can be reasoned that the 5.3 GPa data point corresponds to almost 100% shock induced reaction occurring in the 58% dense powder mixture and the 4.3 GPa data point represents a shock pressure state in which the 58% dense Mo + 2 Si powder mixture undergoes an appreciable (but not complete) shock-induced reaction.

From Figure 5, if the 5.3 and 4.3 GPa data points are respectively considered to represent evidence of complete and partial shock-induced chemical reaction in 58% dense Mo + 2 Si powder mixtures, then the cluster of data points corresponding to the three experiments at 6.2-6.6 GPa, which show minimal expansion and remain close to the inert Mo + 2 Si mixture Hugoniot can be considered to reveal very limited or practically no shock-induced reaction.

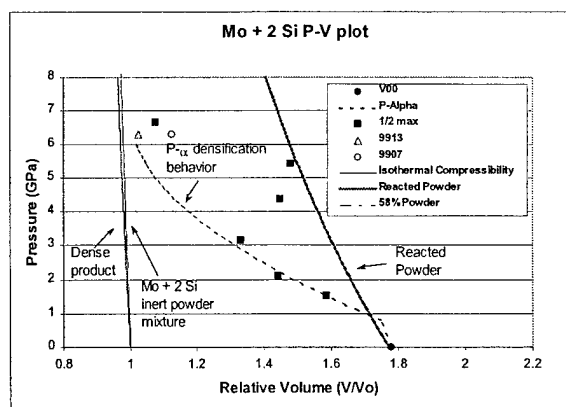


Figure 5. Data points of measured input stress versus calculated relative volume (based on half-max values) re-plotted with the isothermal compressibility curves of dense  $\text{MoSi}_2$  alloy, Mo+2Si inert mixture with zero crush strength, P- $\alpha$  densification densification behavior, and reacted product Hugoniot.

Such anomalous behavior would be expected in these otherwise higher-pressure experiments if the mixing between reactants is restricted (due to other dissipative mechanisms), which consequently inhibit reaction initiation during the shock compression process.

While the input stress (pressure) versus relative volume compressibility behavior illustrated in Figure 5, is based on use of jump conditions, which may be argued to only representing first order effects of shock compression, the correlation between measured shock wave speed and input stress provides a behavior which is independent of assumptions. The experimentally obtained data points of wave speed versus input stress (Figure 4 (b)), are re-plotted in Figure 6 along with the calculated curve corresponding to the 58% dense inert Mo + 2 Si powder mixture (illustrated as a dashed line). It can be seen that the experimental data points appear to follow the inert Hugoniot curve at stresses < 6 GPa. At higher stresses, the data points actually show lower wave speed corresponding to that of low-compressibility melt phase of Si (obtained from [10]). As shown in Figure 6, it can be seen that the Hugoniot of melted silicon (dashed-dot line) intersects the Mo + 2 Si inert Hugoniot curve at  $P_m$  (~5 GPa) which represents the stress at which Si in the ~58% dense Mo + 2 Si powder mixture undergoes melting. The data points corresponding to experiment numbers 9919, 9907, and 9913 are found to lie more closely on the silicon melt Hugoniot than on the Hugoniot of the Mo + 2 Si powder mixture or

its product. The cluster of these data points is also the same as the group of data points on the input stress versus relative volume plot in Figure 5, which were considered to correspond to un-reacted states. Hence, it can be concluded that experimental data points that reveal evidence of melting of Si, also show lack of shock-induced reaction, which suggests that melting of Si inhibits occurrence of shock-induced reaction in Mo + 2 Si powder mixtures. The wave speed versus input stress data points in Mo + 2 Si were converted to a linear plot of wave speed versus particle velocity (where particle velocity,  $U_p = P/\rho_0 U_s$ ). Figure 7 shows the  $U_s$ - $U_p$  plot with the experimentally obtained data and the calculated curves for product and inert reactant mixture, as well as the Hugoniot of silicon melt obtained from Ref. 10. It can be seen that the three experimental data points at lower particle velocities show higher shock wave speeds than that calculated for the inert Mo + 2 Si curve. This is again since the calculated curve is based on an assumed crush strength being zero. The next two data points between  $U_p = 0.8$  and  $1.0$ , closely approach the calculated curve. With further increase in particle velocity, the data points show a decrease in shock wave speed and in fact fall on the  $U_s$ - $U_p$  curve of un-reacted and melted Si.

A similar result has also been observed in the prior work on ~55% dense Nb-Si powder mixtures [10], in which the authors in fact observed that in experiments performed at the same shock pressure (and thus particle velocity) the data points fell on either of two branches. One set of data fell along the  $U_s$ - $U_p$  curve of melted Si, corresponding to no reaction. The other set of data points fell along the calculated curve of product Nb + Si, corresponding to complete reaction. Hence, premature melting of silicon (observed in some cases) was considered to inhibit shock-induced reaction, while in other cases under similar conditions, lack of melting of silicon led to shock-induced reaction in Nb + Si powder mixtures, at stresses in the vicinity of the crush strength. Thus, results on Mo + 2 Si and Nb+Si powder mixtures show similar trends, with melting of silicon at higher stresses resulting in lack of reaction.

In recent modeling work of Tamura and Horie [18] on reaction initiation in Nb + Si powder mixtures inside regions of an adiabatic shear band, they observed that increasing shear rate resulted in

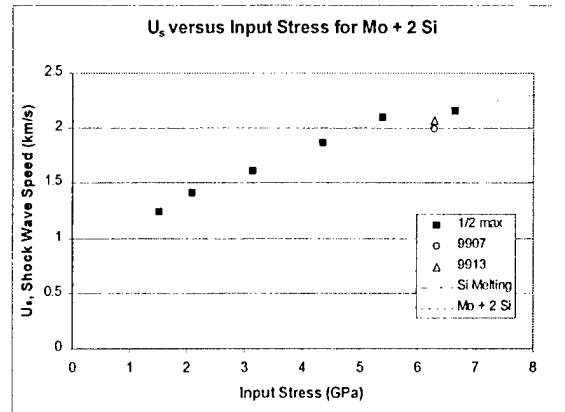


Figure 6.  $U_s$ -P plot with mixture curve and silicon behavior

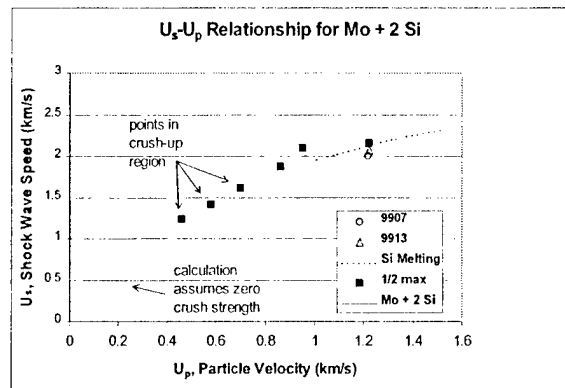


Figure 7.  $U_s$ - $U_p$  curve for Mo + 2 Si (~58% dense).

greater degree of thinning (deformation) of reactants and consequently both mixing and increased propensity for shear-induced solid-state reaction initiation. However, with increased shearing rate, if temperature of silicon was allowed to increase (due to its lower product or density with heat capacity ( $\rho C_p$ ) value) and exceed its melt temperature, then the degree of mixing between solid niobium and liquid silicon was reduced which inhibited reaction initiation. In fact, they observed a critical shear rate, above which premature melting of silicon was always observed which resulted in loss of its shear and tensile strength resulting in its behaving more like a fluid and inhibiting reaction.

Solid-state shock-induced reaction mechanisms have been proposed by Dremin and Bruesov [1], and by Graham [19]. In both cases, generation of intimate contact between well-mixed and highly activated reactants as they reconfigure following shearing past

each other, is essential for reaction initiation. Hence, considering a solid-state mechanism being responsible for shock-induced reactions occurring at pressures in the range of the crush strength of the powder mixture, reaction initiation will be possible only following intimate mixing of the reactants, due to deformation and flow, or fracture and dispersion of reactants, resulting in an highly activated state. Premature melting of silicon during this process and its capillary flow around Mo particles will result in insufficient deformation and plastic flow of the latter, due to its being subjected to more hydrostatic rather than deviatoric compression. Consequently, the mixing between Mo + 2 Si reactants will be limited which will result in inhibiting the initiation of shock-induced reaction.

The shock-induced reaction pressure threshold is observed to be correlated with the crush strength of the powder mixtures based on results of present work on Mo-Si powder mixtures as well as of past work on Ti-Si powder mixtures. The crush strength in turn scales with yield strength differential between reactants. For example the yield strength differential of Mo-Si ( $\Delta\sigma_{Y}^{Mo-Si} = 400-93$  MPa) is greater than that of Ti-Si ( $\Delta\sigma_{Y}^{Ti-Si} = 59-93$  MPa), consequently the crush strength of Mo-Si powder mixture is greater than that of Ti-Si, which is also the reason why the threshold stress of shock-induced reaction initiation in Ti-Si powder mixtures ( $\sim 1.2$  GPa) is lower than that in Mo-Si powder mixtures ( $\sim 5$  GPa). The crush strength also depends on other extrinsic parameters such as powder morphology (size and shape), packing density, and volumetric ratio of reactants, as observed in the prior work on Ti-Si [8]. Hence, for a given system, varying the extrinsic parameters can alter the crush strength of the powder mixtures.

Considering the influence of melting of silicon with the powder densification process, it can be seen that if the crush strength of the powder mixture is greater than the melt pressure of Si, then premature melting of silicon during the crush-up process can be expected, which will limit mixing between reactants and consequently inhibit the initiation of shock-induced reaction. If on the other hand, the melt pressure of silicon is greater than the crush strength, then shock-induced reaction initiation in the powder mixture would be expected to occur at stresses in the vicinity of the crush strength of the powder mixture.

#### 4. CONCLUSIONS

Time-resolved experiments performed on  $\sim 58\%$  dense Mo + 2 Si powder mixtures at input stresses less than the crush strength (measured to be  $\sim 4$  GPa), show characteristics of densification represented by the P- $\alpha$  behavior. The measured propagated wave stress profiles show characteristics of wave dispersion with rise time  $> \sim 40$  nanoseconds. In experiments at input stress between 4-6 GPa, the powder mixtures show evidence of shock-induced reaction, based propagated wave profiles showing a sharp rise time ( $< \sim 10$  ns), and the data points of shock states revealing expansion and approaching the pressure-volume compressibility curve of thermodynamically determined Hugoniot of reacted powder.

Experiments on Mo+2Si powder mixtures at input stresses greater than 6 GPa, showed lack of shock-induced reaction which is inferred based on the following: (a) propagated stress profiles showing a slower rise-time, (b) reduced wave speeds recorded in these experiments performed at even higher pressures, (c) data points falling on the pressure-volume compressibility curve corresponding to unreacted (inert) Mo + 2 Si powder mixture in the P-V plane, as well as along the melted silicon Hugoniot curve in the wave speed versus input stress and wave speed versus particle velocity planes.

Hence, the overall results illustrate that premature melting of silicon during the powder crush up process, inhibits initiation of shock-induced reaction. Consequently, "shock-induced" reaction initiation may only be possible during the crush up process at pressures less than the  $\sim 6$  GPa melt pressure of silicon.

#### 5. ACKNOWLEDGEMENTS

This research was funded by the Army Research Office under Grants DAAH0495-1-0235 and DAAG55-97-1-0163. We also gratefully acknowledge the partial stipend (for KV) support provided by the Georgia Institute of Technology Molecular Design Institute, under prime contract N00014-95-1-1116 from ONR.

## REFERENCES

1. A.N. Dremin and O.N. Bruesov, "Processes Occurring in Solids Under the Action of Powerful Shock Waves," *Russian Chemical Reviews*, **37** [5] (1968) 392-402.
2. Thadhani, N. N., *J. Appl. Phys.* **76**, 2129-2138 (1994).
3. Meyers, M.A., Yu Li-Hsing, and Vecchio, K. S., *Acta metall. mater.* **42**, 701-714 (1994).
4. Vecchio, K. S., Yu Li-Hsing, and Meyers, M. A., *Acta metall. mater.* **42**, 715-729 (1994).
5. Marquis, F. D. S. and Batsanov, S. S., "Advances in Shock-induced Synthesis and Densification of Metal Silicides", in *Powder material: current Research and Industrial Practices*, TMS, 113-128 (1999).
6. Montilla, K., PhD. Thesis, California Institute of Technology, 1997.
7. Aizawa, T. and Yen, B. K., "Shock-induced Reaction Mechanism to Synthesize Refractory Metal Silicides" To be published in APS meeting of Shock Compression of Condensed Matter-1997
8. Thadhani, N.N., R.A. Graham, T. Royal, E. Dunbar, M.U. Anderson, and G.T. Holman, "Shock-induced Chemical Reactions in Ti-Si Powder Mixtures of Different Morphologies: Time-Resolved Pressure Measurements and Materials Analysis," *Journal of Applied Physics*, Vol. 82 (3), (1997) pp. 1113-1128.
9. S.S. Batsanov, G.S. Doronin, S.V. Klockhov and A.I. Teut, *Combustion, Explosion, and Shock Waves*, **22** (6), 134-139 (1986).
10. Yoshida, M., and Thadhani, N. N., "Study of Shock-induced Solid State Reaction by Recovery Experiments and Measurements of Hugoniot and Sound Velocity," in *Shock Waves in Condensed Matter-1991*, edited by S.C. Schmidt, R.D. Dick, J.W. Forbes, and D.G. Tasker, Elsevier Science Publishers, B. V., 1992, pp. 586-592.
11. M.F. Gogulya, I.M. Voskoboinikov, A.Yu Dolgoborov, N.S. Dorokhov, and M.A. Brazhnikov, *Sov. J. Chem. Phys.*, **11**, 343-347 (1992).
12. K.R. Iyer, L.S. Bennett, F.Y. Sorrell, and Y. Horie, "Solid State Chemical Reactions at the Shock Front" in *High-Pressure Science and Technology - 1993*, edited by S.C. Schmidt, J.W. Shaner, G.A. Samara, and M. Ross, AIP Conference Proceedings 309, Part 2, 1993, pp. 1337-1340.
13. L.E. Bennett, K.R. Iyer, Y. Horie, in *Shock Compression of Condensed Matter - 1991*, eds. S.C. Schmidt, R.D. Dick, J.W. Forbes, and D.G. Tasker, Elsevier, (1992), pp. 605-608.
14. Vandersall, K.S., and Thadhani, N.N., in *Molybdenum and Molybdenum Alloys Symposium held at the 126<sup>th</sup> TMS Annual Meeting and Exhibition*, in San Antonio, TX, February 16-19, 1997, TMS Press, pp. 61-69.
15. Graham, R.A., Anderson, M.U., Horie, U., You, S-K, Holman, G.T., "Pressure measurements in Chemically Reacting Powder Mixtures with the Bauer Piezoelectric Polymer Gauge," *Shock Waves* **3**:79-82, 1993.
16. Carroll, M. M. and Holt, A. C., *J. Appl. Phys.*, Vol.43, No.4, April 1972.
17. Bennett, L.S. and Horie, Y., "Shock-induced inorganic reactions and condensed phase detonations," *Shock Waves* (1994) **4**:127-136.
18. Tamura, S., and Horie, Y., *J. Appl. Phys.*, Vol. **84**, No. 7, 1 October 1998, pp. 3574-3580.
19. R. A. Graham, in *Proceedings of the 3<sup>rd</sup> International Symposium on High Dynamic Pressures*, edited by R. Charet (Assoc. Francaise de Pyrotechnie, Paris, 1989), pp. 175-180.

## APPENDIX A2 - PREPRINT

C. Collins, N. Thadhani and Z. Iqbal, "Possible synthesis of beta-C<sub>3</sub>N<sub>4</sub> by shock-compression of C-N precursors," CARBON, 2001, **in press**.

# **SHOCK-COMPRESSION OF C-N PRECURSORS FOR POSSIBLE SYNTHESIS OF $\beta$ -C<sub>3</sub>N<sub>4</sub>**

Charles Collins,\* Naresh Thadhani,\* and Zafar Iqbal\*\*

\*School of Materials Science and Engineering,  
Georgia Institute of Technology, Atlanta GA 30332

\*\*Research & Technology, Allied Signal Inc., Morristown NJ 07962

## **ABSTRACT**

We report on the possible synthesis of the theoretically predicted  $\beta$ -phase of carbon nitride (C<sub>3</sub>N<sub>4</sub>) by shock compression of sodium dicyanamide mixed with sodium azides and carbon tetra-iodide. Shock-compression experiments were performed on starting precursor blended with ~95 wt% Cu powder, statically pressed in steel capsules. The capsules were impacted under conditions of constant shock amplitude, but varying shock-pulse duration. TEM analysis of the recovered shock-compressed residue showed crystallites of a cubic C-N compound dispersed in an amorphous matrix, with overall yield of the crystalline phase being a function of the shock-pulse duration. Parallel-detection electron energy loss spectroscopy of the nitrogen-containing crystallites revealed diamond-like sp<sup>3</sup> bonding. Infra-red spectroscopy indicated absorption lines in regions calculated to be appropriate for  $\beta$ -C<sub>3</sub>N<sub>4</sub>.

Keywords: A. Carbon Nitrides      B. Shock Synthesis      C. TEM and EELS Analysis

D. Infra-red Spectroscopy

***TO BE PUBLISHED IN CARBON, 2001 (in press)***

## 1. INTRODUCTION

Various types of pressure-less<sup>1,2</sup> as well as static and dynamic high-pressure techniques,<sup>3,4</sup> have been successfully employed for synthesizing the two hardest known materials - diamond with  $sp^3$  type carbon bonding and the cubic-phase of boron nitride. Synthesis of these super-hard materials has been accomplished not only via transformation of graphitic or amorphous precursors into the cubic phase, but also via chemical reaction between decomposing carbonaceous precursors with other reactants.<sup>3</sup> The high-pressure shock-compression loading technique has proven to be an important method, not only for fundamental studies of structural and chemical changes, but also for the post-mortem characterization and property evaluation of the recovered high-pressure phases and metastable compounds<sup>5,6</sup>.

The metastable tetrahedral phase of carbon nitride ( $\beta$ - $C_3N_4$ ) has been predicted by Cohen<sup>7</sup> using both a semi-empirical scaling relationship and a pseudo-potential total energy calculation, to have bulk modulus approaching that of diamond and exceeding that of cubic boron nitride. The semi-empirical model,<sup>7</sup> expresses the bulk modulus,  $B$ , in GPa as:  $B = N_c/4 \{ (1971 - 220 \cdot I) / d^{3.5} \}$ , where  $N_c$  is coordination number,  $d$  is bond length in Å, and  $I$  is a measure of the ionicity of the compound. The form of the equation shows a strong dependence on bond length and a weak dependence on degree of ionicity. Thus, for diamond, assuming  $I = 0$ ,  $N_c = 4$ , and  $d = 1.54$  Å, one obtains  $B = 435$  GPa, which is in good agreement with an experimental value of bulk modulus equal to 443 GPa. Similarly, predictions for c-BN reveals bulk modulus exactly the same as the experimental value of 369 GPa, and for  $\beta$ - $Si_3N_4$  a predicted value of 230 GPa compared to the experimental value of 250 GPa. Based on a crystal structure of  $\beta$ -phase  $C_3N_4$ , with coordination number equal to 3.43 and bond length of 1.43 Å, the bulk modulus of this compound is calculated to be 414 GPa. Likewise pseudopotential calculations predict the bulk modulus of  $\beta$ - $C_3N_4$  to be equal to 427 GPa.<sup>7</sup>

Synthesis of the theoretically predicted  $\beta$ - $C_3N_4$  super-hard material is complicated because, unlike

diamond, it involves two chemical components:  $sp^3$ -bonded carbon and  $sp^2$ -bonded nitrogen. Several attempts have been made to synthesize carbon nitride using a variety of techniques.<sup>8-17</sup> Most of the approaches, in general, have resulted in the formation of hydrogenated or partially crystalline compounds, or non-stoichiometric (nitrogen deficient) compounds. Haller et al<sup>8</sup> patented the synthesis of  $\beta$ - $C_3N_4$  and  $\alpha$ - $C_3N_4$  compounds by sputter deposition. Their synthesized films had a nominal composition of  $C_3N_2$  (40 at.% N) with approximately 12 at.% oxygen. Chen et al<sup>9</sup> also attempted the synthesis of carbon-nitride compounds by sputter deposition. They obtained mixtures of amorphous and crystalline forms which were nitrogen deficient (29 at.% N) on average, and contained about 3 at.% oxygen. Niu et al<sup>10</sup> reported the synthesis of  $\beta$ - $C_3N_4$  by pulsed laser ablation of graphite targets combined with an intense atomic nitrogen source with kinetic energies exceeding 1 eV. Up to 40 at.% N was incorporated on average, and photoelectron spectroscopy confirmed C-N covalent bonds.

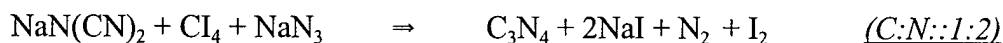
Shock compression of C-N-H containing precursors has been studied by Wixom<sup>15</sup> to prepare  $\beta$ - $C_3N_4$ . While no carbon-nitride compounds were formed, their results were very encouraging. Products of decomposition of the precursor materials, containing well-ordered diamond were recovered. Later, the results of Ricci et al.<sup>16</sup> and Sekine et al.<sup>17</sup> using plasma enhanced chemical vapor deposition and shock synthesis, respectively, indicated that the presence of hydrogen in the precursor was severely detrimental to the synthesis process. The results obtained by Wixom<sup>15</sup> and Sekine et al<sup>17</sup> demonstrated that decomposition of organic precursors and subsequent chemical reactions do occur during shock-compression. Their results also affirmed that metastable reaction products, such as the ordered diamond phase, can be kinetically captured if just enough shock energy is used to decompose the reactants and quench the accompanying thermal energy.

In the present work, synthesis of possible metastable  $\beta$ -phase  $C_3N_4$  was studied by a method employing shock-induced decomposition and chemical reaction in precursors of a compound containing

C-N seed molecules and excess carbon and nitrogen, but no hydrogen. Recent theoretical studies as well as experimental investigations of time-resolved measurements have revealed that chemical reactions resulting in the formation of compounds (in highly activated state) can indeed occur during the micro-second duration of the high-pressure shock-compression state.<sup>18-22</sup> The influence of shock-pressure pulse-duration on the yield of the recovered compound was also studied by performing impact experiments using projectiles of two different flyer-plate thicknesses.

## 2. EXPERIMENTAL PROCEDURE

The precursor selected in the present work was hydrogen-free, and contained constituents (other than carbon and nitrogen) that would form either stable diatomic gases or ionic salts. Hence, sodium dicyanamide [NaN(CN)<sub>2</sub>] was selected as the main precursor which would also provide a seed for heterogeneous nucleation of the CN compound, and carbon tetra-iodide (CI<sub>4</sub>) and sodium azide (NaN<sub>3</sub>) were included as additional sources of carbon and nitrogen, respectively. Compounds of commercial purity were purchased from Aldrich and mixed to produce appropriate atomic ratios of carbon and nitrogen. The expected reaction, stated below, was based on the assumptions that the azide group would lose a nitrogen molecule, sodium and iodine would form an ionic salt, and excess nitrogen would form a diatomic gas.



The precursor mixture was then blended with 95 wt.% copper powder (added to quench the heat generated during shock-compression and exothermic chemical reaction) and packed in steel capsules at ~85% theoretical maximum density (TMD) for shock synthesis experiments.

Shock-compression experiments performed in a previous study by Wixom<sup>15</sup> used extreme pressures (~100 GPa), typical of those appropriate for diamond synthesis via phase transformation of

graphite. The present work was based on chemical reaction between products of decomposing organic precursors, which are expected to occur at much lower shock pressures. Hence, the experiments were performed using a 3-capsule gas-gun impact fixture (shown schematically in Figure 1) at an impact velocity of  $\sim 700$  m/s, using projectiles with flyer plates of two thicknesses (4.75 mm and 9.5 mm) to yield different pulse durations. The incident one-dimensional shock pressure for the gas-gun impact experiments at 700 m/s impact velocity, was calculated to be  $\sim 2$  GPa, and the maximum peak pressure generated due to two-dimensional radial wave focusing effects was determined to be 20-25 GPa. The corresponding shock pulse durations for the two gas gun experiments were calculated to be  $\sim 1.8$   $\mu$ s with the 4.75 mm flyer thickness and 3.6  $\mu$ s with the 9.5 mm thickness flyer plate. It should be noted that these estimated shock conditions are those for pressed copper powder (95 wt% of total mass). The small fraction of organic precursor used and lack of their available Hugoniot characteristics, precluded determination of the shock conditions in the precursors. Hence, the differences in shock conditions are only for qualitative comparison.

Following shock-compression, the compacts were recovered by machining the steel capsules. Boiling concentrated nitric acid was used to dissolve the copper and product salts from the recovered shock-compressed material. Typical yields of residue recovered were  $\sim 50$ -100mg of fine black powder, collected by filtration on a fine glass frit. Implicit in this sample recovery procedure is the expected assumption that carbon nitride is insoluble in boiling concentrated nitric acid. The residue recovered from the shock-compressed samples after dissolving the copper and salts with acid treatment, was examined by transmission electron microscopy (TEM), energy dispersive spectroscopic (EDS) analysis, Parallel-detection Electron Energy Loss Spectroscopy (PEELS), and infra-red (IR) spectroscopy.

### **3. RESULTS AND DISCUSSION**

Table I summarizes the gas-gun shock-compression experimental conditions and results of microstructural observations of the two recovered samples which will be discussed below.

Table I - Experimental Conditions and Results of Observations of Recovered Samples

Sample #	Packing Density	Impact velocity (Pulse duration)	Critical Results and key Observations
4-2	~92%	700 m/s (1.8 $\mu$ s)	C & N containing amorphous product observed by TEM/EDX, and IR signal showed $\beta$ -phase
5-2	~88%	700 m/s, 3.6 $\mu$ s	C & N containing nano-crystallites in amorphous matrix observed by TEM, EDX, & EELS analysis, IR signal showed $\beta$ -phase

TEM characterization coupled with EDS and PEELS analysis, was used to identify phases formed in Sample # 5-2. The recovered powder residue was suspended on a carbon-coated Cu grid. Dark field imaging showed presence of isolated bright-contrast diffracting particulates (of approximately 40 nm) dispersed in an amorphous matrix, as shown in Figure 2 (a). The crystallinity of the dispersed phases was confirmed by the SAED pattern which revealed diffraction spots of cubic symmetry (Fig. 2 (b)). The particles were unstable under the electron beam, thus, making the diffraction pattern highly transitory in character. However, the most significant result was exhibited by TEM/PEELS analysis of the diffracting crystallites observed in Figure 2 (a). As shown in Figure 2 (c), the K-edge absorptions of carbon at 292 eV and nitrogen at 401 eV, reveals an  $sp^3$  type atomic bonding, characteristic of diamond-like<sup>23</sup> material with high hardness and bulk modulus. Considering the ionization cross-section ratio for C:N to be 2.5:2.0, it appears that the region with crystallites embedded in a carbon matrix contains ~8-13 at% N, indicating

that the material is nitrogen-containing  $sp^3$  bonded carbon phase.

Infra-red (IR) spectroscopy was also employed in an attempt to characterize the bulk composition and bond structure. Samples of the shock-compressed organic residue were examined by pressing it with KBr to form pellets. A typical IR spectrum of Sample # 4-2, is shown in Figure 3. The envelope of lines between 300 to 400  $cm^{-1}$  and also between 470 to 710  $cm^{-1}$  can be assigned to the  $SnO_2$  impurity, which came from the Sn-impurity present in the commercially acquired Cu powder. No  $SnO_2$  lines above 800  $cm^{-1}$  are expected.<sup>24</sup> The broad envelope of lines between 900 and 1300  $cm^{-1}$  can be assigned to a  $\beta-C_3N_4$  structure, based on comparing the envelope with that of the published IR spectra of  $\beta-Si_3N_4$ .<sup>25,26</sup> Three lines at 910, 985, and 1040  $cm^{-1}$  are observed in this region of the spectrum of  $\beta-Si_3N_4$ , as shown in the insert in Figure 3. Assuming that these lines are associated primarily with Si-N stretching motions, we can predict the shift of these lines for  $\beta-C_3N_4$ , replacing Si with C. Thus, considering, the scaling factor to be the ratio of stretching frequencies ( $\omega$ ) related to reduced-mass ( $\mu$ ) ratios for  $\beta-Si_3N_4$  and  $\beta-C_3N_4$ , we have:

$$(\omega_{Si-N}/\omega_{C-N}) = (\mu_{C-N}/\mu_{Si-N})^{1/2}$$

This calculation gives a scaling factor of 0.8322, with which we find the corresponding positions for carbon nitride to be 1093, 1183 and 1249  $cm^{-1}$ . Three spectral features are indeed observed in this range at 1040, 1100, and 1150  $cm^{-1}$  in the IR spectrum of Sample # 4-2, as shown in Fig 3. The agreement with the calculated frequencies is fairly good considering that the shock synthesized product most probably does not have an ideal  $\beta-C_3N_4$  structure and that the absolute values of the force constants for  $C_3N_4$  may be somewhat different from that of  $Si_3N_4$ .

IR spectroscopy of these shock-compressed samples also showed the dependence of the yield of  $\beta$ -phase  $C_3N_4$  on the duration of the shock-pressure pulse. The IR spectra of the short duration Sample # 4-2, and the long duration Sample # 5-2, shown in Figure 4 (a) and (b), respectively, reveal clear

indication of IR structure analogous to that of  $\beta$ -phase  $\text{Si}_3\text{N}_4$ , described above. The peaks in the 1960 to 2140  $\text{cm}^{-1}$  region of the spectrum arise due to  $\text{C}=\text{N}$  stretching vibrations from perhaps unreacted sodium dicyanamide precursor. The sharp line at 1380  $\text{cm}^{-1}$  can be assigned to un-extracted copper nitrate. The broad absorption around 1080  $\text{cm}^{-1}$ , as well as the three sharp absorption lines at 470, 500, and 590  $\text{cm}^{-1}$ , are attributed to  $\beta$ -phase  $\text{C}_3\text{N}_4$  bonded similarly to  $\beta$ - $\text{Si}_3\text{N}_4$ .

Comparison of the IR traces from samples of the two gas gun experiments shows that there is larger volume fraction of the crystalline  $\beta$ - $\text{C}_3\text{N}_4$  phase in the recovered product obtained from the longer duration experiment. This is indicated by the increased intensity of absorption in the longer duration sample. The increased crystallinity in the longer duration sample suggests the influence of an imposed kinetic constraint on the formation (or retention) of crystalline  $\beta$ -phase carbon nitride during shock-compression.

#### **4. SUMMARY AND CONCLUSIONS**

Organic precursors containing sodium dicyanamide, sodium azide, and carbon tetra-iodide, mixed with 95 wt% Cu powder, were shock-compressed under different pressure-pulse duration, and shown to result in the possible formation of  $\beta$ -phase carbon nitride. TEM characterization showed presence of crystallites dispersed in an amorphous matrix, with PEELS analysis of the nitrogen-containing crystallites showing diamond-like  $\text{sp}^3$  bonding, with N-content of  $\sim 8\text{-}13$  at%. Infrared spectroscopy indicated absorption in the regions calculated to be appropriate to the  $\beta$ -phase  $\text{C}_3\text{N}_4$ . The synthesis of this possibly  $\beta$ -phase  $\text{C}_3\text{N}_4$  compound was observed to show increasing yield (based on increasing IR-peak intensity) in samples obtained from experiments performed with longer shock-pulse duration.

## **ACKNOWLEDGMENTS**

The authors acknowledge the help of Prof. Kent Barefield, for useful discussions with respect to precursor selection and preparation, and Prof. Z.L. Wang and Ms. Yolande Berta for their help with TEM and PEELS characterization. The infra-red spectroscopy analysis was performed at Allied-Signal, Inc. This research was funded by ARO Grants DAAH04-94-6-0192 and DAAG55-97-1-0163.

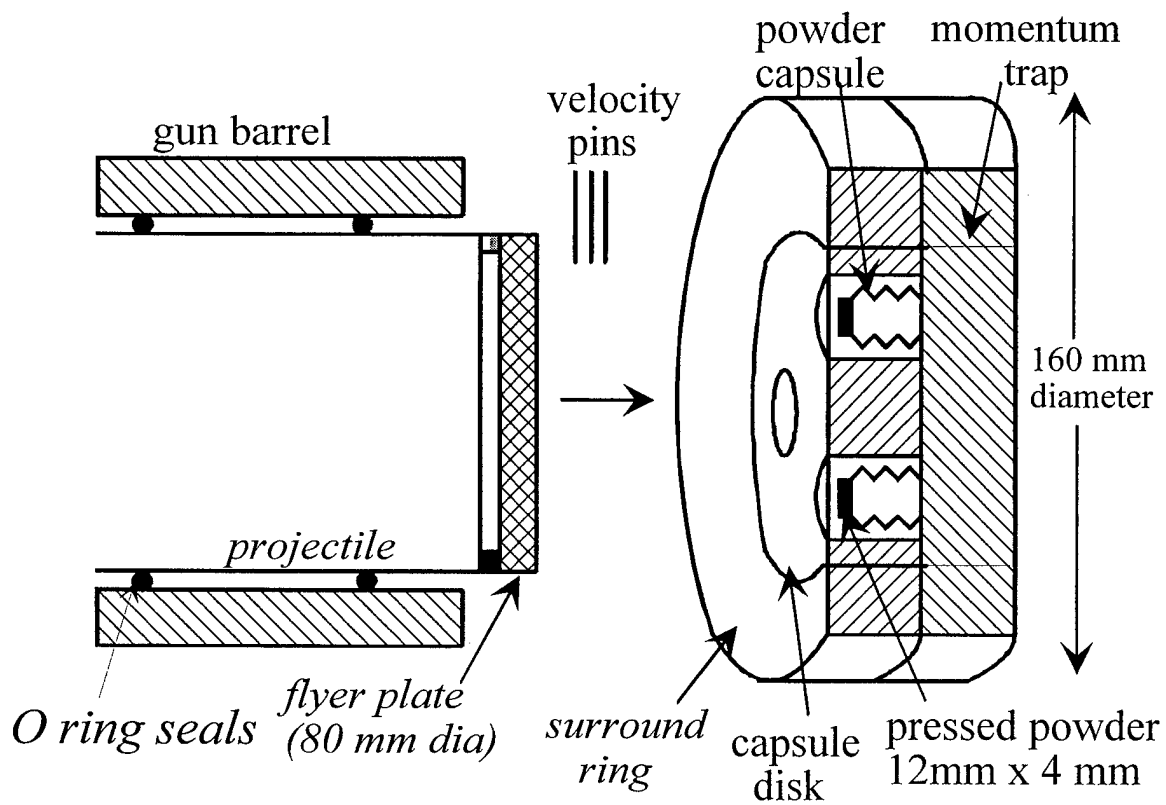
## **LIST OF REFERENCES**

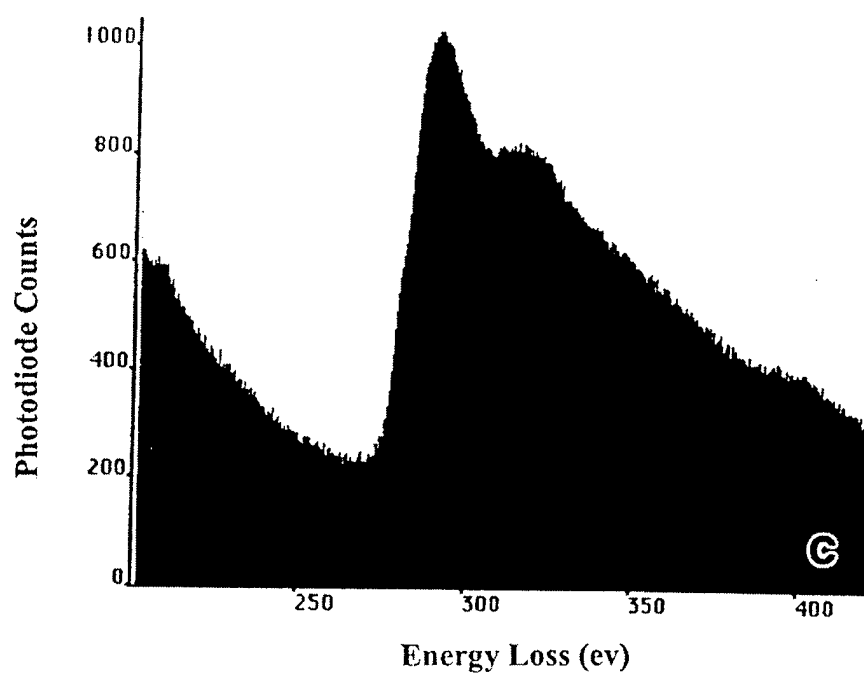
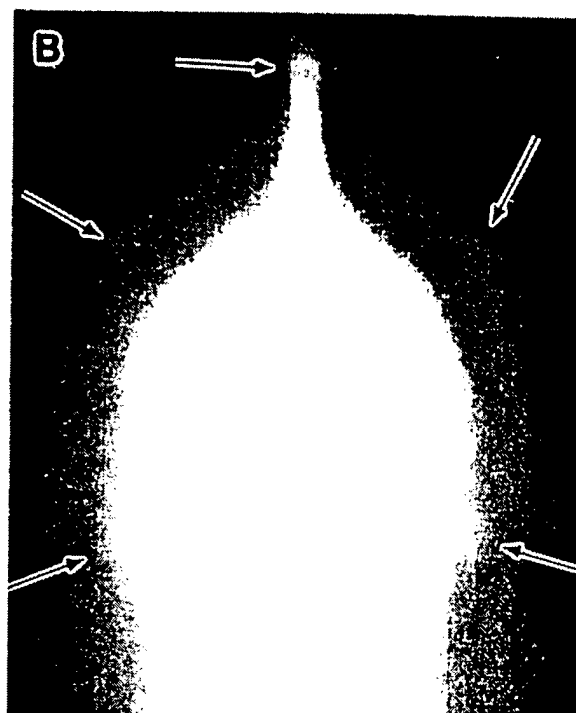
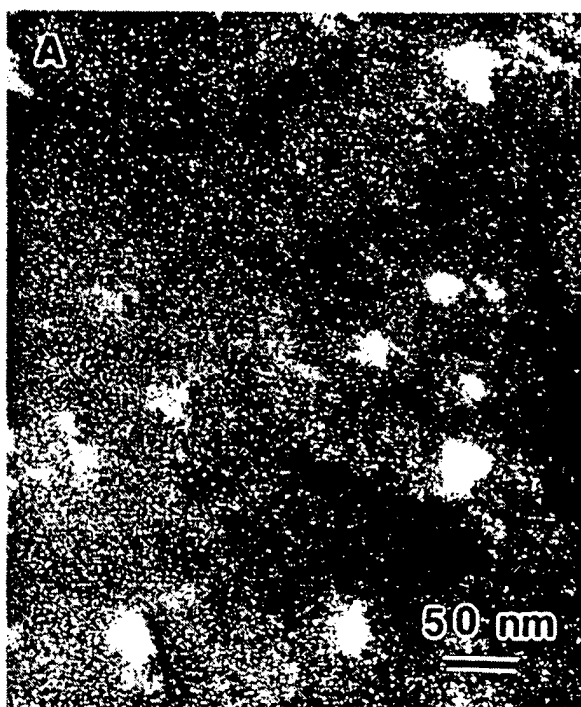
- [1]. Yarbrough WA, and Messier R, Science, 247 (1990) 688.
- [2]. Angus JC and Hayman CC, Science, 214 (1988) 913.
- [3]. DeCarli PS and Jamieson JC, Science, 133 (1961) 1821.
- [4]. Sekine T, J. Mat. Sci. Lett., 8 (1989) 61.
- [5]. Duvall G (Co-ordinator) "Shock Compression Chemistry in Materials Science Synthesis and Processing," Report of the Committee of the National Materials Advisory Board Commission on Engineering and Technical Systems, National Research Council, Publication NMAB-4 14, Washington, D.C., (1984).
- [6]. Horie Y and Sawaoka AB, Shock Compression Chemistry of Materials,
- [7]. Cohen ML, Science, 234 (1986) 549, 245 (1989) 8, and 261 (1993) 307.
- [8]. Haller EE, Cohen ML and Hansen WL, U. S. Patent No. 5,110,679, "Hard Carbon Nitride and Method for Preparing Same," May 5, 1992.
- [9]. Chen MY, Lin X, Dravid VP, Chung YW, Wong MS, and Sproul WD, Surface and Coatings Technology, 54/55 (1992) 360.
- [10]. Niu C, Lu YZ and Lieber CM, Science, 261 (1993) 334.

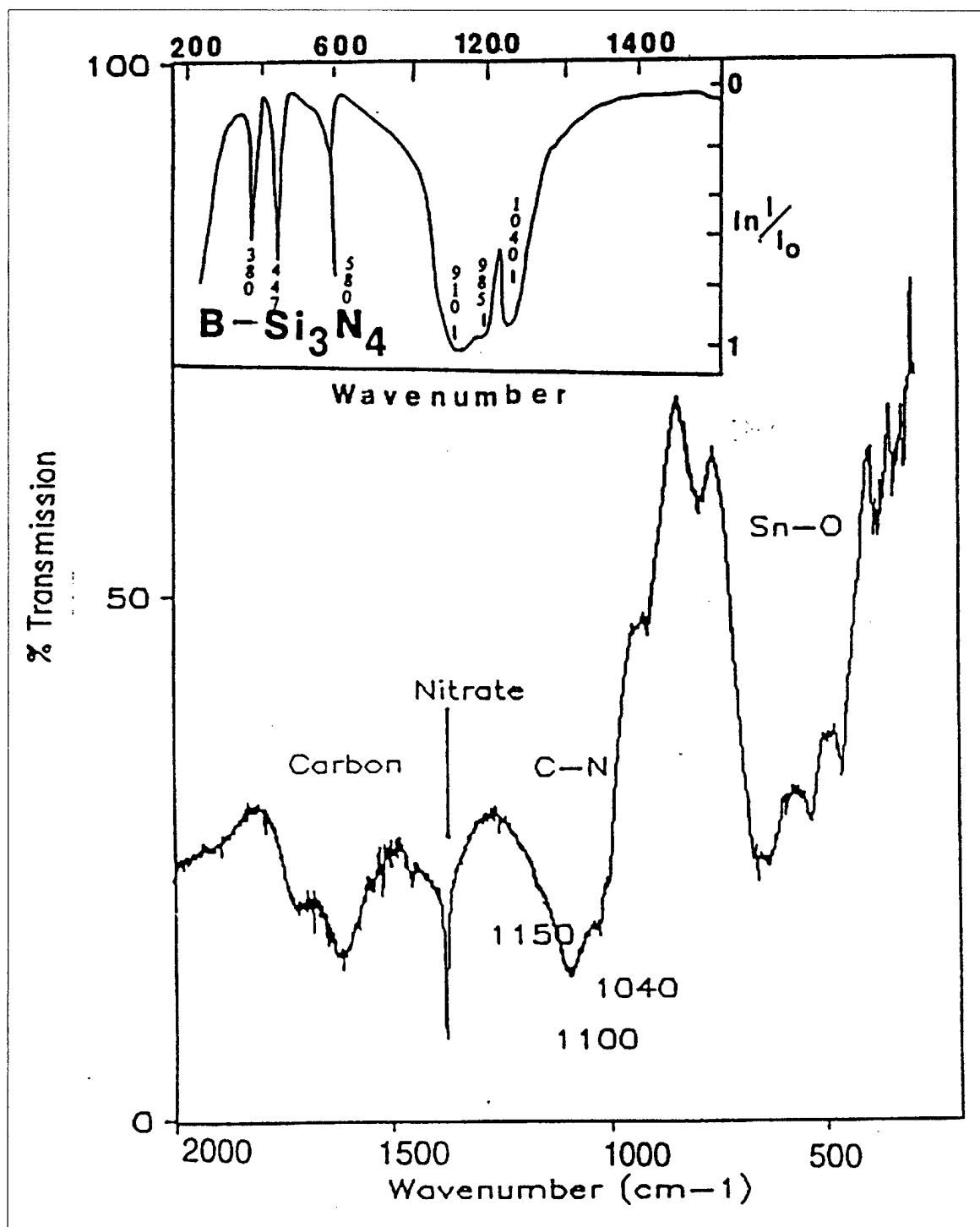
- [11]. Maya L., Cole D. R and Hagama E. W. n, J. Am. Ceram. Soc., 74 (1991) 1686.
- [12]. Kouvetakis J. , Bandari A, Todd M., Wilkens B. , and Cave N., Chem. Mater., 6 (1994) 811.
- [13]. Miyamoto Y., Lonic S.G., and Cohen M.L., Phys. Rev. Lett., 76 (1996) 2121.
- [14]. Qin Z. C., Yu R. C, Xu L-W, Zhang X.Y. , Xu Y.F , Phil. Mag. Letts., Vol. 78 (6), pp. 453-459, (1998).
- [15]. . Wixom M. R, J. Am. Ceram. Soc., 73 (1990) 1973.
- [16]. Ricci M., Trinquescoste M. ,Auguste F. , Canet R., and Delhaes P., J. Mat. Res., 8 (1993) 480.
- [17]. Sekine T., "Synthesis of Inorganic and Organic Materials," Proceedings of ARO workshop: Shock Synthesis of Materials, Georgia Tech, Atlanta, May 1994.
- [18]. Batsanov SS, Mater. Sci. and Eng. - A, A210, (1996) 57-63.
- [19]. . Iyer KR, Bennett LS, Sorrell FY, and Horie Y, "Solid State Chemical Reactions at the Shock Front" in High-Pressure Science and Technology - 1993, edited by Schmidt SC, Shaner JW, Samara GA, and Ross M, AIP Conference Proceedings 309, Part 2, 1993, pp. 1337-1340.
- [20]. Thadhani NN, Graham RA, Royal T, Dunbar E, Anderson MU, and Holman GT, Journal of Applied Physics, Vol. 82 (3), (1997) pp. 1113-1128.
- [21]. Horie Y and Sawaoka AB, Shock-Compression Chemistry of Materials, KTF Scientific Publishers, Tokyo, Chapter 6, 1993.
- [22]. Bennett LS and Horie Y, Shock Waves: An International Journal, 4, 127-136 (1994).
- [24]. Wibbelt M, Kohl H , and Kohler-Redlich P, Phys. Rev. B, Vol. 59 (18), pp. 11739-45, 1999.
- [25]. Katiyar et. al., J. Phys. C. Solid St. Physics, 4 (1971) 2421.
- [26]. Wada et. al., J. Non-crystalline Solids, 43 (1981) 7.
- [27]. Borgen O and Seip HM, Acta Chem. Scand., 8 (1961) 15.

## LIST OF FIGURES

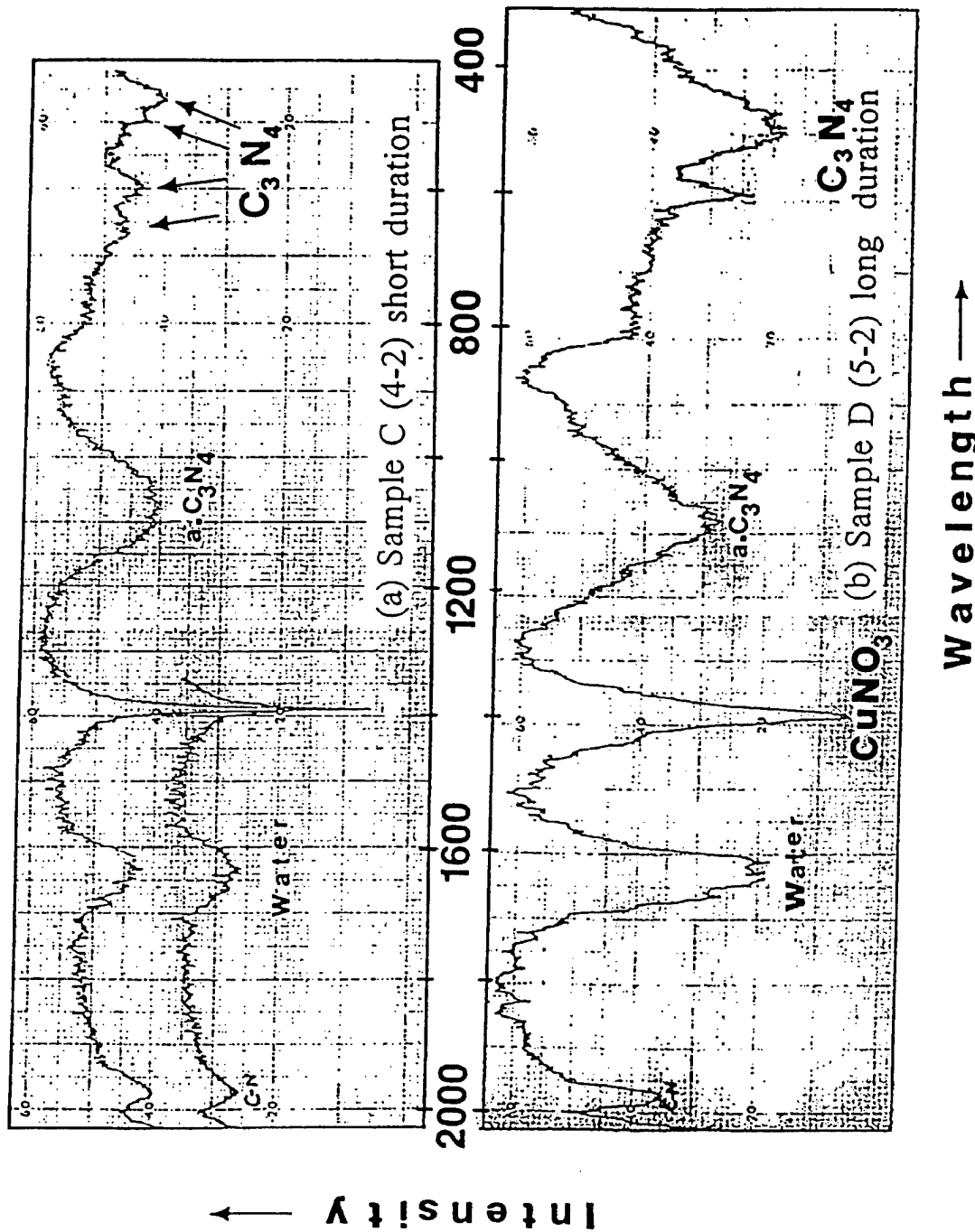
- Figure 1. Schematic showing the loading configuration employed using the 3-capsule gas-gun shock-compression recovery fixture.
- Figure 2 (a) Dark field image showing diffraction of nitrogen containing particles in shock-synthesized residue of Sample # 5-2, along with corresponding (b) diffraction pattern and (c) PEELS spectrum of carbon- and nitrogen-containing crystallite, showing characteristic K-edges, indicating diamond-like  $sp^3$  bonding.
- Figure 3 - Typical IR spectrum for Sample # 5-2 showing C-N bond structure analogous to that of  $\beta$ -phase  $Si_3N_4$ , inferred from published IR pattern of  $\beta$ - $Si_3N_4$  shown in the insert.<sup>23,24</sup>
- Figure 4 - IR spectra of (a) Sample # 4-2 (short duration) and (b) Sample # 5-2 (long duration), showing higher intensity  $\beta$ -phase  $C_3N_4$  peaks (indicating increasing yield) in longer shock-pressure pulse-duration sample.







# IR SPECTRA OF MIX II - $\text{NaN}(\text{CN})_2 + \text{Cl}_4 + \text{NaN}_3$



## **APPENDIX A3 - PREPRINT**

S.N. Namjoshi and N.N. Thadhani, "Modeling the Reaction Synthesis of Shock-densified Titanium-silicon Powder Mixture Compacts," Metallurgical and Materials Transactions, Vol. 31, No. 2, 2000, pp. 307-316.

# Modeling the Reaction Synthesis of Shock-Densified Titanium-Silicon Powder Mixture Compacts

S.A. NAMJOSHI and N.N. THADHANI

The reaction behavior of shock-consolidated Ti-Si powder mixture compacts, densified at 5 to 7 GPa pressure, was investigated to determine conditions required for solid-state reaction synthesis leading to the formation of dense  $\text{Ti}_5\text{Si}_3$  intermetallic compounds with fine-grained microstructure. It was observed that at temperatures greater than 1000 °C, the heat released following reaction initiation in the solid state exceeds the rate of heat dissipation causing a self-propagating combustion-type reaction to take over the synthesis process forming highly porous reaction products. A reaction synthesis model was developed to allow the prediction of optimum conditions necessary to ensure that the bulk of the reaction in dynamically densified Ti-Si powder compacts occurs by rapid solid-state diffusion and without being taken over by the combustion process. The model incorporates mass and heat balance with the kinetics evaluated using experimentally determined apparent activation energies for solid-state and combustion reactions. Considering the decrease in activation energy (as measure of degree of shock activation), average particle size, and compact porosity as the main variables, the model plots the fraction reacted as a function of time for various postshock reaction-synthesis temperatures, illustrating the dominant reaction mechanism and kinetics. The results show that although changes in average particle size and compact porosity influence the synthesis temperature above which the reaction may be taken over by the combustion-type process, lowering of the activation energy *via* shock-compression influences the time for reaction completion in the solid state.

## I. INTRODUCTION

REACTION synthesis processes involving highly exothermic self-sustained combustion-type chemical reactions (occurring in mixtures of elemental or thermite-type powder mixtures) result in the formation of compounds of high purity, fine grain size, and even metastable phases.<sup>[1-4]</sup> However, the large volume change accompanying product formation, the violent gas expulsion, and shrinkage occurring during solidification from the melt can lead to considerable retained porosity in the reaction product. Reaction synthesis followed immediately by dynamic densification, while the product is hot and plastic, has been applied with some success<sup>[5-8]</sup> to form bulk materials. However, the brittle nature of ceramics and intermetallics can lead to their cracking due to thermal stresses generated during cooling of the densified reaction products through the ductile-to-brittle transition temperature. An alternative, which combines the benefits of reaction synthesis and dynamic densification, is to use the latter process to first densify powder mixtures into green-density compacts for subsequent reaction synthesis.

Dynamic densification, employing shock compression of powders, produces a dense-packed highly activated state of mixture constituents. The plastic flow, dispersion, and mixing of reactants, intimate contacts between cleansed surfaces of abraded powder particles, and grain size reduction *via* fracture and/or subgrain formation<sup>[9,10]</sup> resulting from shock compression can significantly enhance the chemical reactivity of the reactants.<sup>[11]</sup> One can advantageously use this highly activated dense-packed state of powders to impose

thermodynamic and kinetic limitations on the combustion reaction and, at the same time, accelerate the kinetics of solid-state reactions. Thus, dynamic densification offers the opportunity to precondition the material and control the post-shock reaction synthesis process thereby avoiding problems inherent to self-sustaining combustion reactions and forming dense compounds with refined microstructures.

Figure 1 schematically illustrates three situations showing fraction reacted as a function of temperature corresponding to the behavior that may be observed during reaction synthesis of highly exothermic elemental powder mixtures. Curve 1 shows the case corresponding to where no reaction product is formed until the melting of one of the constituents (or the eutectic), upon which a combustion-type reaction almost instantaneously converts all reactants to products. Such a reaction behavior is typical of loosely packed powder mixtures of highly reactive systems, in which the rate of heat dissipation is much lower than the rate of heat generation. Curve 2 shows an initial constant-rate increase in reaction fraction due to a solid-state reaction followed by an abrupt change whereby the remaining reactants are instantaneously converted to products due to a combustion-type reaction. Such a reaction may occur, *e.g.*, in a dense-packed powder compact, if the heat released from the solid-state reaction exceeds the rate of heat dissipation and becomes localized. Both of these cases of reaction synthesis represent situations that need to be prevented because their consequence is the formation of a highly porous reaction product. Curve 3 shows no abrupt changes in the slope and corresponds to the most desirable case, whereby the reaction fraction increases at a steady rate as a function of temperature, and almost all reactants convert to products *via* solid-state diffusion. Such a condition would be possible if the kinetics of the initial solid-state reaction is rapid so that at any reaction temperature, the heat evolved is insufficient to melt the reactants

S.A. NAMJOSHI, Graduate Student, and N.N. THADHANI, Professor, are with the School of Materials Science and Engineering, Georgia Institute of Technology, Atlanta, GA 30332-0245.

Manuscript submitted September 16, 1999.

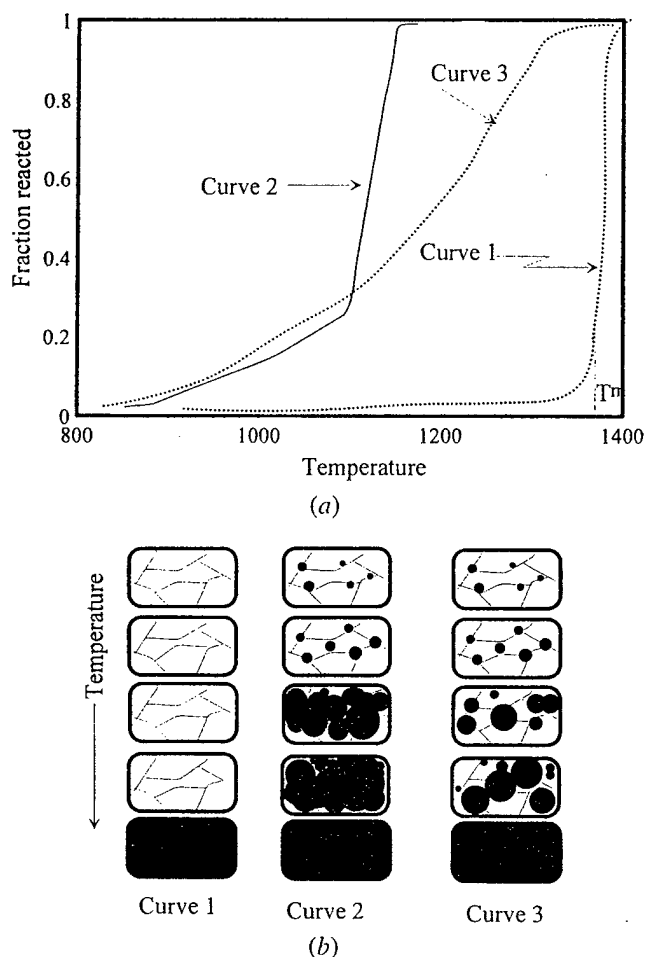


Fig. 1—(a) and (b) Schematics illustrating three situations corresponding to fraction reacted as a function of temperature. Curve 1 corresponds to the case where no reaction product is formed until the melting of one of the constituents (or the eutectic), upon which a combustion-type reaction almost instantaneously converts all reactants to products. Curve 2 shows an initial steady-state reaction followed by an abrupt increase in fraction reacted due to being taken over by a combustion-type reaction. Curve 3 shows the reaction fraction increases at a steady rate as a function of temperature, with all reactants converting to products *via* rapid solid-state diffusion.

either due to a lack of heat generation or a more rapid rate of heat dissipation.

Past work on the reaction synthesis of shock-densified intermetallic- and ceramic-forming powder mixtures has shown solid-state chemical reactions occurring at significantly lower temperatures (*e.g.*, in Ni-Al alloys<sup>[12]</sup> as well as lowering of the activation energy for solid-state diffusion by four to six times (*e.g.*, in Ti-C powder mixtures<sup>[13]</sup>). However, it has been observed that even with such levels of activation, at any stage of the solid-state reaction, if the rate of heat released exceeds that of heat dissipation leading to temperature localization, then a combustion-type self-sustained reaction is initiated in the dynamically densified compacts<sup>[14]</sup> similar to the case illustrated by curve 2 in Figure 1. The formation of products then occurs *via* a dissolution and reprecipitation mechanism yielding products with high residual porosity.

It is, therefore, necessary to be able to predict, for a given powder mixture system, compact density, and degree of

shock activation, the optimum postshock heat-treatment conditions required for preventing the onset (or controlling the extent) of a combustion-type reaction following an initial solid-state reaction. The reaction between Ti and Si forming  $\text{Ti}_5\text{Si}_3$  involves heat of reaction,  $\Delta H_R = -72.5 \text{ J/g} \cdot \text{atom}$ , volume change from reactants to products,  $\Delta V = -28 \text{ pct}$ , and the adiabatic reaction temperature exceeding the melting point of  $\text{Ti}_5\text{Si}_3$  (*i.e.*, 2130 °C). Prior work<sup>[15,16]</sup> on reaction synthesis and mechanical alloying of Ti-Si powder mixtures has shown a behavior dominated by particle size effects. In general, rapid heating rates and coarse particle sizes favor reaction synthesis occurring *via* the combustion mode forming a single-phase  $\text{Ti}_5\text{Si}_3$  reaction product, whereas slow heating rates and fine particle sizes favor solid-state diffusion reactions forming multiple Ti-Si intermetallic phases.

In the present work, the reaction behavior of Ti-Si powder mixtures was modeled based on experimental determination of activation energies (obtained from DTA analysis) and analysis of reaction kinetics based on reaction fraction measurements performed on shock-densified samples reacted in a furnace at different temperatures and hold times. The model incorporated heat and mass transport balance to establish the dominant reaction mechanism and determine how the reaction mechanism is influenced by variables including porosity in the dynamically densified powder compacts, powder particle size, and the degree of shock activation. In the following sections, the experimental procedure will be described first, then the results of activation energy, reaction fraction measurements, and their correlation with reaction kinetics models will be presented, and finally, the model predictions of the reaction behavior based on thermal and mass transport balance will be discussed.

## II. EXPERIMENTAL PROCEDURE

Elemental Ti and Si powders (CERAC, -325 mesh, ~20- to 40- $\mu\text{m}$  average size) were used in the present work. The Sandia Momma Bear and Poppa Bear recovery fixture with Baratol explosives (MB-B and PB-B)<sup>[17]</sup> and the Georgia Tech single-capsule compressed-gas gun recovery fixture (SC-GG)<sup>[18]</sup> were used to shock densify the Ti-Si powders. The powders were blended in a  $\text{Ti}_5\text{Si}_3$  stoichiometry and cold-pressed to ~52 pct initial packing density. Loading in the MB-B and PB-B fixtures involves two-dimensional radial wave-focusing effects, which leads to a build up of peak pressure calculated to be ~7.5 GPa in MB-B and ~5 GPa in PB-B.<sup>[19]</sup> In the SC-GG fixture, a peak pressure of ~5 GPa builds upon reverberation of a planar shock wave in the powder sandwiched between the steel-impactor and aluminum-backer plates. Hence, even though the pressures in the PB-B and SC-GG fixtures are the same, the degree of plastic deformation and flow of the powders is somewhat greater in PB-B than in the SC-GG fixture.

A PERKIN-ELMER DTA-7\* was used to perform the

\*PERKIN-ELMER DTA 7 is a trademark of Perkin-Elmer Physical Electronics, Eden Prairie, MN.

differential thermal analysis (DTA) experiments and obtain the apparent activation energies by heating the samples at different rates. Reaction synthesis experiments to determine the fraction reacted as a function of time and temperature were also performed on samples of the dynamically densified compacts. The samples were encapsulated in quartz tubing

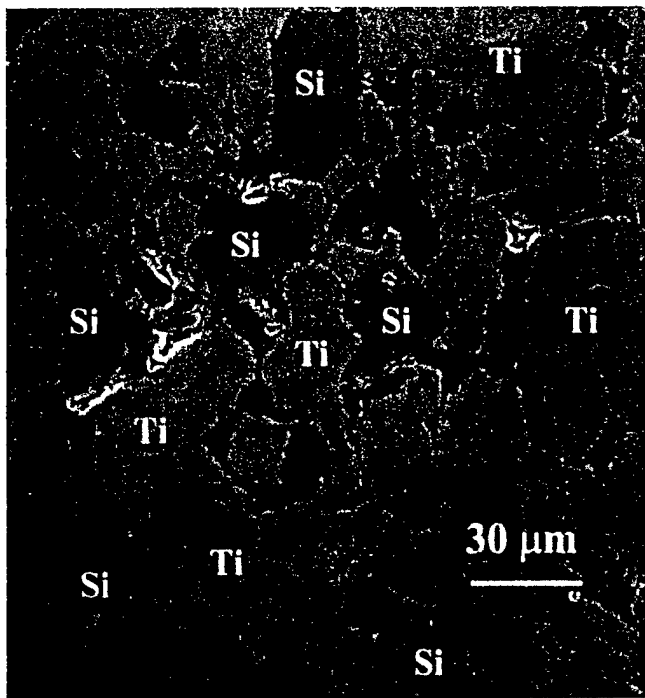


Fig. 2—SEM micrograph of shock-densified Ti-Si PB-B compact (~96 pct dense), showing a uniform distribution of intimately mixed Ti and Si powder constituents.

under  $10^{-5}$  torr vacuum and heated in a Lindberg horizontal tube furnace at varying temperatures and times. The shock-densified compacts, before and after reaction synthesis, were characterized using scanning electron microscopy (SEM) and X-ray diffraction (XRD). The Williamson–Hall analysis of the XRD patterns obtained from the shock-densified compacts was used to determine the microstrain retained in Ti and Si. Reaction fraction measurements in reacted samples were determined, based on semiquantitative XRD analysis, using the areas of the three strongest peaks of the reactants and products. Prior to the use of XRD data, the instrumental broadening error was estimated using a Si standard and subtracted from the data obtained for the samples. Peak fitting was performed using a Lorentzian mathematical function.

### III. RESULTS AND DISCUSSIONS

#### A. Characterization of Shock-Densified Ti-Si Powder Compacts

The shock-densified Ti-Si powder compacts (mixed in  $5\text{Ti} + 3\text{Si}$  stoichiometry corresponding to  $\text{Ti}_5\text{Si}_3$  intermetallic) were prepared using the MB-B, PB-B, and SC-GG shock-recovery fixtures described earlier. Figure 2 shows a typical SEM micrograph of the ~96 pct dense PB-B compact, revealing a fairly homogenous microstructure consisting of highly deformed and uniformly mixed elemental constituents. The XRD analysis of the shock-densified compacts showed only broadened peaks of elemental Ti and Si confirming that there was no evidence of chemical reaction and product formation during the shock-densification process but just plastic strain. Microstrain determined based on the Williamson–Hall line-broadening analysis<sup>[20]</sup> of XRD

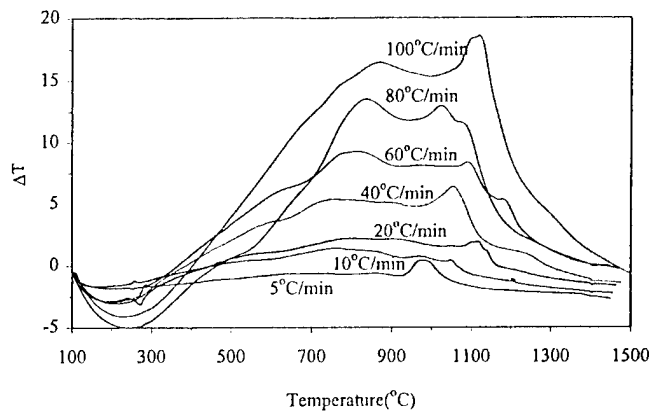


Fig. 3—DTA traces of shock-densified Ti-Si samples (PB-B compacts) at different heating rates, showing the presence of low-temperature exotherms (at  $T < 1000$  °C) corresponding to solid-state reaction and high-temperature exotherms corresponding to combustion-type reactions in each trace.

data indicated retained plastic strain to be 0.003 to 0.004 in Ti, and ~0.002 strain along with crystallite size reduction in Si, in each of the shock-densified compacts. The values of retained microstrain correspond to dislocation densities of the order of  $10^{11}$  to  $10^{12}$   $\text{cm}^{-2}$  calculated using the Williamson–Smallman approximation.<sup>[21,22]</sup>

The degree of activation caused by shock-compression during dynamic densification of Ti-Si powder mixtures was investigated by reacting samples of the compacts in the DTA at different heating rates in order to determine the apparent activation energy. Figure 3\* illustrates DTA traces at heating

\* Compression to fit all traces in the same plot results in loss of resolution of the peaks especially at lower heating rates.

rates of 5 °C, 10 °C, 20 °C, 40 °C, 60 °C, 80 °C, and 100 °C per minute for the Ti-Si samples of shock-densified PB-B compact. It can be seen that there are at least two major reaction exotherms observed in each of the DTA traces. The first, a shallow exotherm, at lower temperatures (800 °C to 1000 °C), corresponds to the reaction occurring in the solid state, while the later exotherms at temperatures  $> 1100$  °C correspond to combustion-type reactions occurring upon melting of Si (or eutectic). At lower heating rates (5 °C/min), only the solid-state reaction exotherms are present and, with increasing heating rates, exotherms corresponding to the combustion reactions become more dominant. The apparent activation energy was then determined using the method proposed by Kissinger<sup>[23]</sup> and Boswell<sup>[24]</sup> based on the following equation:

$$\frac{d \left( \ln \frac{\Phi}{T_m^2} \right)}{d \left( \frac{1}{T_m} \right)} = -\frac{E}{R} \quad [1]$$

where  $\Phi$  is the heating rate,  $T_m$  is the temperature at which the reaction peak is observed,  $E$  is the apparent activation energy, and  $R$  is the universal gas constant. The slope of a plot of  $\ln (\Phi/T_m^2)$  vs  $(1/T_m)$  corresponds to the activation energy for the reaction. Figures 4(a) through (f) show the linear plots from which the apparent activation energies were obtained for the respective reaction mechanisms in each of the three types of recovered shock-densified compacts. It

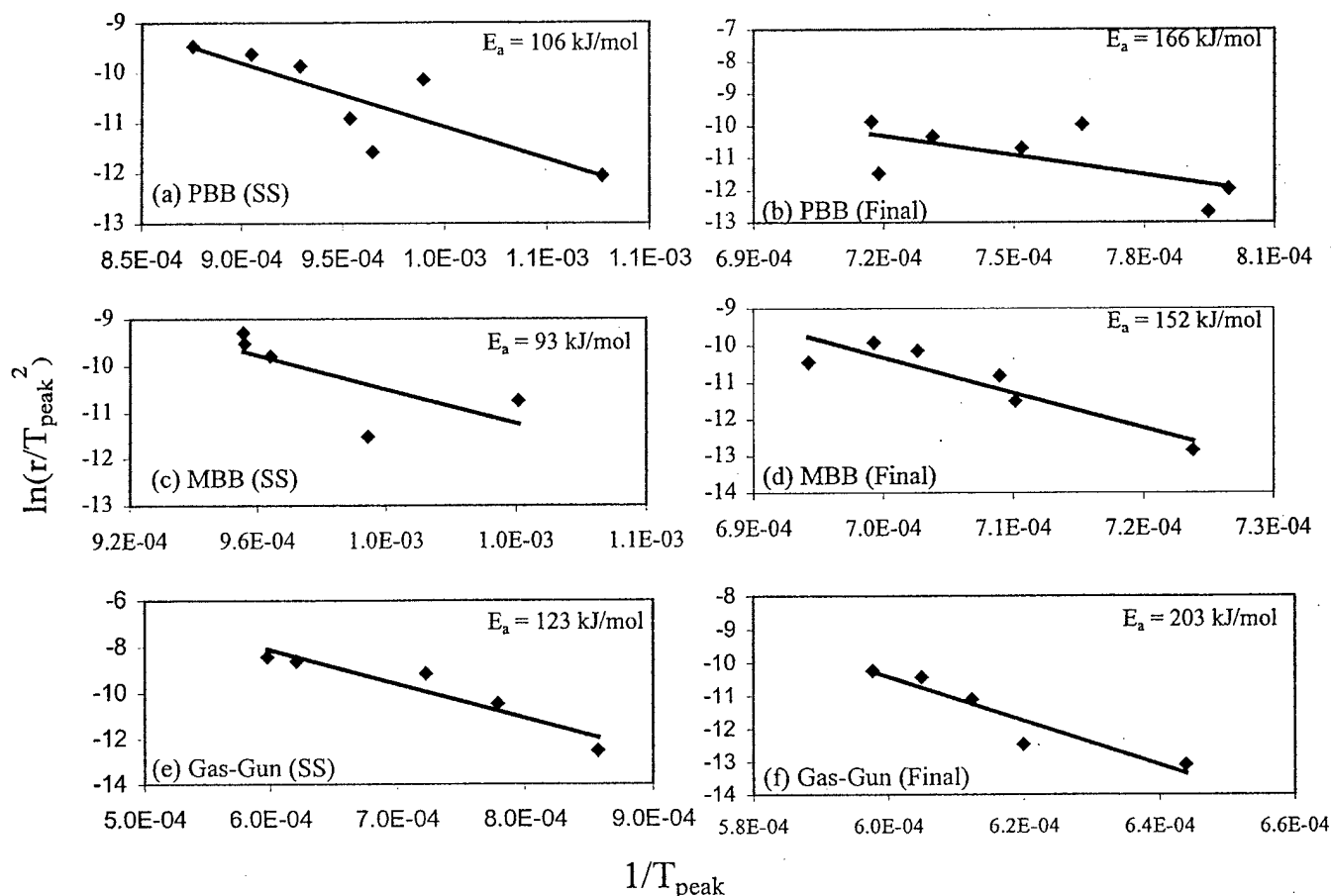


Fig. 4—Linear plots of  $\ln(\Phi/T_m^2)$  vs  $(1/T_m)$  for determining activation energies of solid-state reactions (plots (a), (c), and (e)) and combustion-type reactions (plots (b), (d), and (f)) for the three types of powder compacts.

can be seen that the apparent activation energies decrease as the densification condition become more intense. Consequently, the MB-B Ti-Si compact has the lowest activation energy in contrast to that of the PB-B and SC-GG compacts.

#### B. Determination of Reaction Kinetics

Reaction synthesis experiments were performed on encapsulated samples of the shock-densified ~96 pct dense PB-B compacts and heated in a furnace at various temperatures between 800 °C and 1200 °C with hold times of 30 minutes to 24 hours. The fraction of reaction products formed under the different thermal treatments was determined based on the semiquantitative analysis of XRD data. The fraction reacted vs time data (at various temperatures) obtained from these experiments is plotted in Figure 5. Curves of calculated fraction reacted vs time obtained based on Carters' model for solid-state diffusion<sup>[25,26]</sup> and the Johnson-Mehl-Avrami (JMA) kinetics model for dissolution and reprecipitation mechanism representing combustion-type processes,<sup>[27]</sup> are also plotted in Figure 5. According to Carter's solid-state diffusion reaction model, the fraction transformed ( $F$ ) as a function of time ( $t$ ) is given by<sup>[25,26]</sup>

$$[1 + (Z - 1)F]^{2/3} + (Z - 1)(1 - F)^{2/3} = \left[ \frac{(1 - Z)Dk}{r^2} \right] t \quad [2]$$

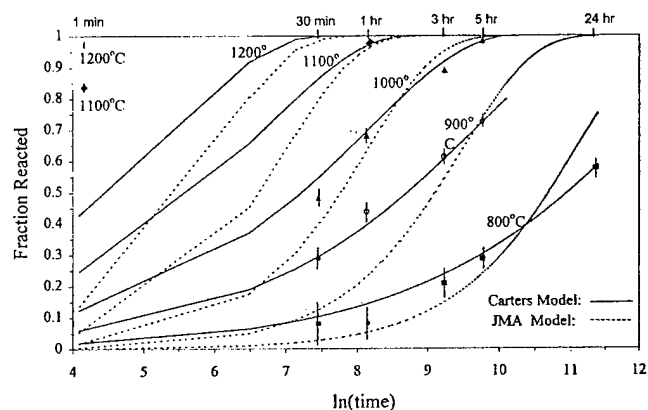


Fig. 5—Comparison of reaction fraction data obtained from reaction synthesis experiments on shock-densified Ti-Si powder mixtures performed in a furnace, correlated with data obtained from Carter's solid-state diffusion and JMA kinetics models using activation energies determined from DTA experiments.

where  $Z$  is the volume change from reactants to products for a unit amount of reactants and  $r$  is average particle size. Both  $D/k$  and  $k$  are described by an Arrhenius type of equation,  $D/k = D_0/k_0 \exp(-E_a/RT)$ , where  $D_0$  and  $k_0$  are preexponential constants, and  $E_a$  is the activation energy. The JMA model, representing dissolution/reprecipitation

processes involved during combustion synthesis, expresses fraction reacted vs time as<sup>[27]</sup>

$$F = 1 - \exp(-kt^n) \quad [3]$$

where  $n$  is the order of reaction, and the other symbols have the same meaning as in Eq. [2]. The calculated curves were generated using activation energies obtained from DTA experiments (described in the previous section) and rate constants that yielded the best fit to the experimental data. For Carter's model, the rate constant  $k_0 = 1.91$ , and for the JMA model,  $k_0 = 1.95 \times 10^3$  and  $n = 1.3$  were used for all temperatures.

It can be seen from Figure 5, that at the synthesis temperature of 800 °C, Carter's solid-state reaction model fits the experimental data more closely than the JMA kinetics model up to 24 hours of hold time at peak temperature. Extrapolating the reaction fraction with the same trend shows that the reaction would reach completion within 200 hours at 800 °C. Synthesis at 900 °C also shows the reaction behavior dominated by Carter's solid-state diffusion model with reaction completion estimated in 24 to 45 hours. The 1000 °C experimental data shows almost complete reaction with a hold time of 5 hours and reveals a combined influence of behaviors dominated by the solid-state (Carter's model) and combustion mechanisms (JMA kinetics model). Finally, synthesis at 1100 °C and 1200 °C, shows complete reaction occurring almost instantaneously *via* the combustion mechanism.

The experimental evaluation of the reaction kinetics correlated with synthesis models shows that reaction synthesis of shock-densified Ti-Si powder mixtures may be dominated by solid-state diffusion processes at temperatures up to 1000 °C, and at higher temperatures, the reaction is almost instantaneously taken over by the combustion-type process involving dissolution and a reprecipitation mechanism. As mentioned earlier, synthesis dominated by the combustion reaction results in large amounts of heat generation leading to melting of the reaction product(s) and formation of a high degree of retained porosity. A model based on thermal and mass transfer concepts, therefore, needs to be developed to predict the conditions under which reaction synthesis will be taken over by the combustion process and to also establish the influence of shock-densification parameters to ensure that reaction synthesis is dominated by solid-state diffusion.

#### IV. PREDICTIVE MODELING OF THE REACTION BEHAVIOR

Based on the Fourier heat balance relationship, the accumulation of heat (necessary for triggering combustion reaction) is dependent on the initial density of reactants ( $\rho$ ) and fraction of reactants undergoing reaction ( $\eta$ ) according to the following equation:

$$\rho C_p \left( \frac{\partial T}{\partial x} \right) = K \left( \frac{\partial^2 T}{\partial x^2} \right) + \rho Q \left( \frac{\partial \eta}{\partial t} \right) \quad [4]$$

where  $C_p$  is the heat capacity,  $K$  is the thermal conductivity,  $Q$  is the heat of reaction,  $T$  is the temperature,  $t$  is the time, and  $x$  is the coordinate along which a combustion reaction will propagate. The thermal conductivity  $K$ , a kinetically limiting parameter, and the heat of reaction  $Q$ , a thermodynamically limiting parameter, control the extent of heat accumulation and determine whether or not a combustion

reaction will be triggered and become self sustained. The amount of heat conducted is related to the density of the reactants and, hence, to the starting porosity of the compact. Increased density will increase the heat carried away and, consequently, provide a kinetic limitation to heat accumulation. Similarly, if the rate of reactants converting to products at any given time is small, then the heat generated due to reaction will also be low. Hence, a thermodynamic limitation to heat accumulation can be provided if the entire reaction is not initiated instantaneously, as in a combustion mode, but occurs as a controlled solid-state reaction over a temperature range. With shock compression, the density of the powder mixture compact and the defect density of the reactants are both increased, which lowers the activation energy for diffusion and leads to a considerable degree of reaction dominated by defect-enhanced solid-state diffusion. Consequently, at temperatures where a combustion reaction would otherwise be triggered in the absence of prior solid-state reaction, the fraction of reactants available for further reaction may not be sufficient to sustain an uncontrolled combustion reaction.

Considering the previously mentioned factors, a reaction synthesis model incorporating aspects of heat generation, dissipation, accumulation, and defect-enhanced solid-state diffusion has been developed using measured parameters wherever applicable. Based on the results of the model, the influence of processing parameters such as initial powder mixture compact density, shock-compressed configuration of reactants (size of powder constituents and degree of activation), furnace temperature for isothermal heating, and heating rate can be established. The reaction synthesis model is based on transient heat and mass transport and considers the following conditions:

- (1) initial powders (Ti and Si) form a reaction product ( $\text{Ti}_5\text{Si}_3$ ),
- (2) average particle size ( $r$ ) for the initial powders ( $\sim 30 \mu\text{m}$  for Ti and Si),
- (3) given amount of starting porosity (greater than 0),
- (4) volumetric change upon reaction ( $\sim 28$  pct for  $\text{Ti}_5\text{Si}_3$ ),
- (5) heat of reaction for the given system ( $-72.5 \text{ J/g} \cdot \text{atom}$  for  $\text{Ti}_5\text{Si}_3$ ),
- (6) furnace temperature up to  $T < T_m$  ( $T_m$  for Si = 1410 °C),
- (7) thermal conductivities of the initial components and product(s),
- (8) elemental diffusivities for the given system (e.g.,  $D_{\text{Si} \rightarrow \text{Ti}}$ ),
- (9) activation energy for diffusion of constituents for the given system, and
- (10) reaction kinetics model for the chosen system determined experimentally (e.g., Carter's solid-state diffusion or JMA solution-reprecipitation model).

The following assumptions were made during the development of the model.

- (1) Reaction initiation occurs at "hot spots" in the sample (next section discusses details).
- (2) Pores are considered to have a uniform size and are distributed homogeneously. This is reasonable given a uniform reactant particle size (see subsequent discussion).
- (3) Number and distribution of hot spots are directly related to those of porosity. This is a reasonable assumption as the thermal conductivity of air (porosity) is much lower

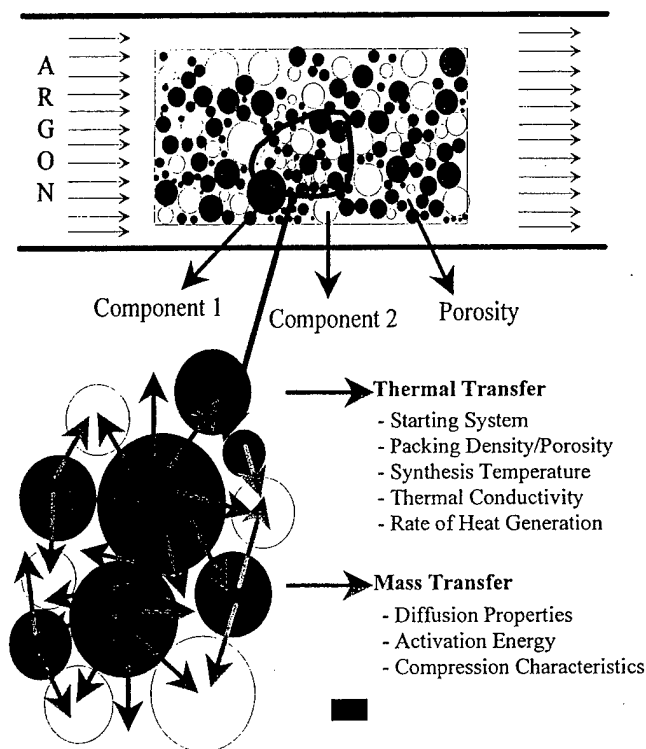


Fig. 6—Schematic of reaction synthesis of a shock-densified powder mixture compact, as it is heated in a furnace under an inert gas atmosphere. Reaction is assumed to occur between two (or more) reactant particles, with thermal transport of heat generated due to reaction into surrounding reactants and accelerated mass transport between reactants being the major events occurring during the reaction synthesis process.

than the metallic reactants and, hence, can lead to the entrapment of heat and, thus, reaction in localized hot spots.

- (4) All particles of a given reactant are assumed to have the same size ( $r$ ).
- (5) It is assumed that if the melt temperature of the lower-melting constituent is exceeded in any region, then reactants in that region will completely convert to products instantaneously. This assumption is consistent with the criterion employed for combustion-synthesis reactions occurring *via* a dissolution and reprecipitation mechanism and resulting in product formation in times scales of three to six orders of magnitude less than that for solid-state reactions.

Figure 6 shows a schematic of the reaction synthesis process in a shock-densified powder mixture compact as it is heated in a furnace under an inert gas. In the figure, a reaction is assumed to occur between two (or more) reactant particles in the region shown. Thermal transport of the heat generated due to reaction into the surrounding reactants and accelerated mass transport between reactants are considered as the major events occurring during the reaction synthesis process. Thermal transport or the rate of heat dissipation is influenced by the type and fraction of starting reactants, their thermal conductivities, initial packing density or porosity, the furnace temperature, and the degree of heat generation. Mass transport, which determines the rate of subsequent heat generation due to further

solid-state reaction, is influenced by the diffusivities of the reactants and the activation energy for diffusion, which, in turn, is influenced by the shock-densification conditions.

During isothermal heating of a powder mixture in the furnace, reaction initiation may occur at many locations in a compact. If these locations of reaction initiation are considered as reaction hot spots that generate heat, an increase in temperature of the reactants surrounding these is expected. This increase in temperature results in an increased rate of solid-state reaction in the reactants and, hence, generation of more heat. As discussed before, if thermal transport is slow and the heat accumulated is sufficient to melt one of the reactants, then a self-sustained combustion reaction will be initiated. Hence, the model first calculates the increase in temperature of the reactants upon equilibration of the heat generated from the reaction hot spots to surrounding reactants as the reactant powder compact is heated in a furnace at any given temperature.

In the model, the number of hot spots per unit volume of the bulk sample is given by  $N_v = 3V_v/4\pi r^3$ , where  $V_v$  is the volume fraction of porosity in the compact, and  $r$  is the average radius of the pores, both of which are determined experimentally. The average distance between the hot spots is considered to be  $\lambda = 4(1 - V_v)/S_v$ , where  $S_v (=4\pi r^2 N_v)$  is surface area of porosity per unit volume.<sup>[28]</sup> The region affected due to the heat generated at a hot spot is defined as the affected reactant region (ARR). For calculation purposes, the model assumes that the average dimension of the ARR is equal to the average distance between two hot spots. However, for the equilibrium temperature calculation, the ARR is considered to have the same distribution as that of the porosity present in the starting compact, in which case the average porosity size is expected to be smaller. The temperature calculation assumes that all the heat generated due to reaction initially heats up the product. Thermal equilibrium is then reached between the hot product and the surrounding ARR. The average increase in local temperature is calculated by numerically solving the following equation for thermal equilibrium between the product and the ARR:

$$m_{\text{reactants}} \Delta H_{\text{reaction}} = \left[ \int_{T_{\text{furnace}}}^{T_{\text{product}}} m_{\text{product}} C_p^{\text{product}}(T) dT \right] + \Delta H_{\text{fusion}}^{\text{product}} \quad [6]$$

$$= \int_{T_{\text{furnace}}}^{T_{\text{equilibrium}}} \sum_{i=\text{reactant}-l}^{i=\text{reactant}-n} m_i C_p^i(T) dT$$

where  $m_i$  is the mass of the  $i$ th (reactant(s) or product(s)),  $\Delta H_{\text{reaction}}$  is the heat of reaction for the system,  $C_p^i$  is the heat capacity of constituent  $i$ , and  $\Delta H_{\text{fusion}}$  is the heat of fusion of the product. The  $\sum_{\text{reactants}}$  indicates the constituents of the ARR, which includes the two reactants and the porosity (containing air).

Figure 7 shows the calculated equilibrium temperature of the ARR, at various furnace temperatures, as a function of porosity for Ti-Si powder compacts (with an average particle size of 25  $\mu\text{m}$ ). It can be seen from the figure that the equilibrium temperature of the ARR increases with increasing porosity, and at any given furnace temperature, the equilibrium temperature will exceed the melting point of silicon if the porosity in a sample exceeds a critical amount. For example, with a furnace temperature of 1000  $^{\circ}\text{C}$ , a compact with a porosity greater than  $\sim 18$  vol pct will

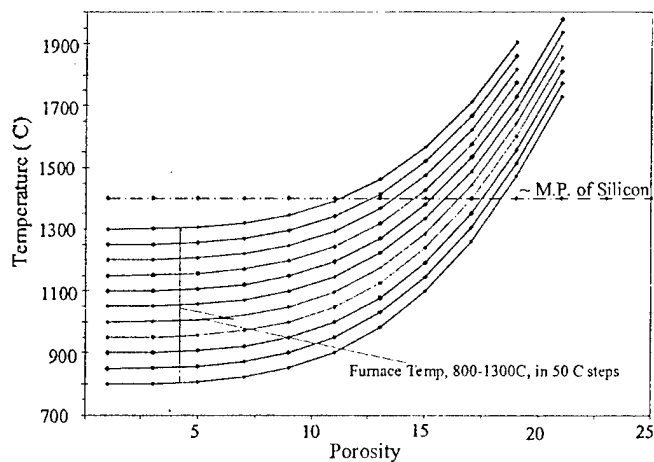


Fig. 7—Equilibrium temperature reached by the ARR, as a function of porosity in the compact, at different furnace temperatures.

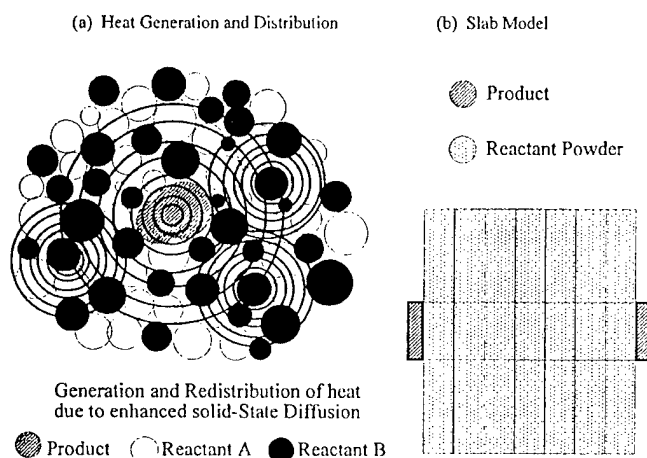


Fig. 8—(a) Schematic showing additional solid-state reaction occurring in the ARR and the subsequent generation of heat due to this reaction. (b) Schematic showing the definition of the slab as the ARR, for calculation of fraction reacted as a function of time at various furnace hold temperatures.

show an equilibrium temperature exceeding the melting temperature of silicon and will consequently undergo a self-sustained combustion-type reaction. Similarly, for a compact with porosity of ~11 vol pct, a furnace temperature exceeding ~1300 °C will raise the equilibrium temperature above the melting point of silicon and initiate the combustion-type reaction. In all cases, it is assumed that there is no reaction occurring until the furnace temperature is reached.

The preceding calculation of the equilibrium temperature gives a qualitative representation of the temperature range in which a combustion-type reaction may be initiated. However, more accurate conditions can be obtained if the accelerated solid-state diffusion occurring in the ARR, as it is being heated, is considered. This aspect is incorporated, as shown in Figure 8, by considering the ARR as a slab of material occupying space between  $y = -b$  and  $y = +b$  initially at a temperature  $T_0$ . At time,  $t = 0$ , the temperature of the surfaces  $y = \pm b$ , is raised and maintained at  $T_1$ . This is considered equivalent to the material between two hot spots in the powder mixture compact. As reaction initiates, the

temperature ( $T$ ) in such a slab can be obtained as a function of time, from heat transfer fundamentals, as<sup>[29,30]</sup>

$$\frac{T_1 - T}{T_1 - T_0} = 2 \sum_{n=0}^{\infty} \frac{(-1)^n}{\left(n + \frac{1}{2}\right)\pi} \exp \left[ -\left(n + \frac{1}{2}\right)^2 \pi^2 \frac{\alpha t}{b^2} \right] \cos \left[ \left(n + \frac{1}{2}\right) \frac{\pi y}{b} \right] \quad [7]$$

where  $\alpha$  is the thermal diffusivity defined as  $k/\rho C_p$ ,  $b$  is the dimension of the slab,  $k$  is the thermal conductivity,  $\rho$  is the density, and  $C_p$  is the heat capacity of the solid. The incorporation of the additional reaction due to the increase in the temperature of the ARR and consideration of the subsequent heat generation in the ARR gives the model a capability to predict the reaction fraction as a function of time and temperature. Because there are many important parameters affecting the reaction kinetics and, hence, the dominant mechanism(s), it is important to understand the effect of each of these process variables.

The model developed in this work was used to separate and, hence, better understand the effect of variables such as furnace hold temperature, activation energy, particle size, and porosity. The results of the predictions are shown in Figures 9 through 11 as plots of fraction reacted as a function of time to obtain the influence of the previously mentioned variables. The experimentally determined reaction fractions obtained from experiments on the Ti-Si system are also shown for comparison purposes.

Calculated plots of fraction reacted as a function of time at synthesis temperatures of 800 °C, 900 °C, and 1000 °C, respectively, based on an apparent activation energy,  $E_a = 106$  kJ/mol and porosity of 3.5 pct, are shown in Figures 9(a) through (c). The solid curves correspond to particle sizes of 20 and 40  $\mu\text{m}$ , and the dotted line represents the 30  $\mu\text{m}$  average particle size consistent with the Ti-Si powders used in the present work. It can be seen from the plots in Figures 9(a) and (b) that the model predictions for 800 °C and 900 °C show S-shaped curves with a gradual increase in the rate of fraction reacted at these synthesis temperatures. The model prediction correlates well with the trend observed in the reaction synthesis experiments based on the close matching of the experimental data points with the dotted curve calculated for the average particle size.\* The gradual

\*The deviation of the experimental points from the model predictions is mostly at lower reaction fractions, where reaction during the heating and cooling cycles is expected to influence the fraction reacted during the hold time.

slope representing fraction reacted suggests that the reaction is occurring in the solid state.

The model calculations for 1000 °C and their correlation with the experimental data for the average 30- $\mu\text{m}$  particle size (shown in Figure 9(c)) reveal S-shaped curves that start out with a shallow slope up to about 30 pct reaction fraction followed by an increase in the rate of reaction. Completion of reaction at 1000 °C occurs in less than five hours hold time. The overall trend, therefore, suggests reaction synthesis in dynamically densified Ti-Si powders (with ~3.5 pct porosity) at 1000 °C involves a combined influence of solid-state and combustion reactions without the latter catastrophically taking over the synthesis process. At temperatures

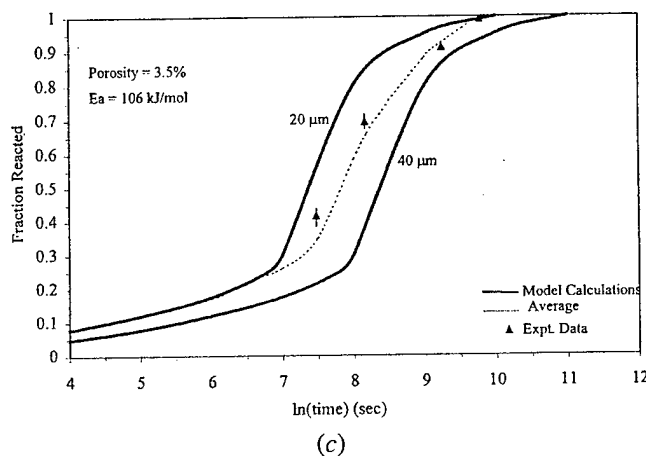
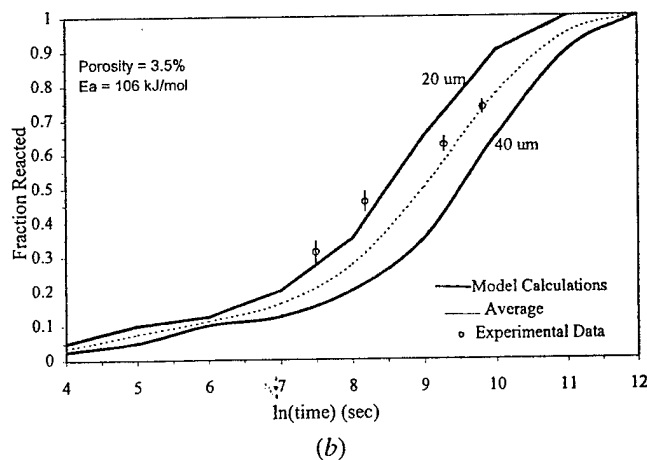
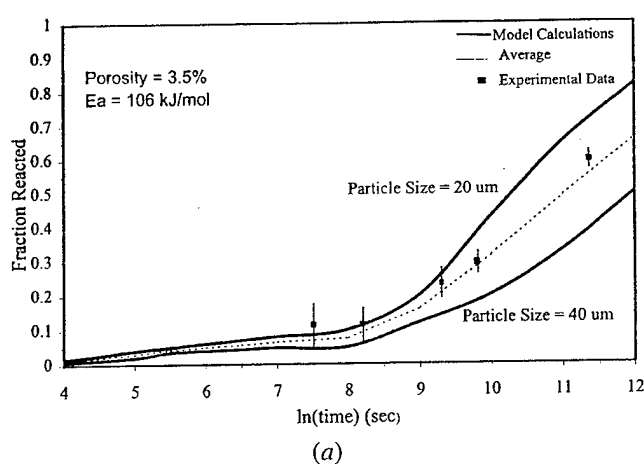


Fig. 9—Model calculations of fraction reacted as a function of time for Ti-Si powder mixture compacts with 3.5 pct porosity, activation energy for solid-state diffusion  $E_a = 106$  kJ/mol, and particle size range from 20 to 40  $\mu\text{m}$  (30  $\mu\text{m}$  average) at (a) 800 °C, (b) 900 °C, and (c) 1000 °C.

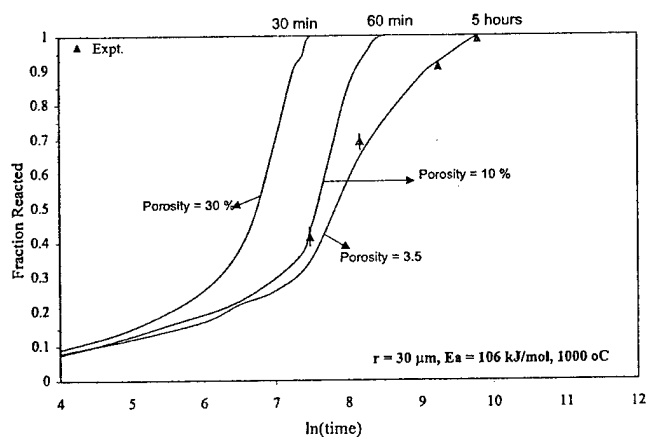


Fig. 10—Plot of reaction fraction as a function of time, for constant reaction temperature, particle size, and activation energy, showing the influence of compact porosity on the reaction mechanism.

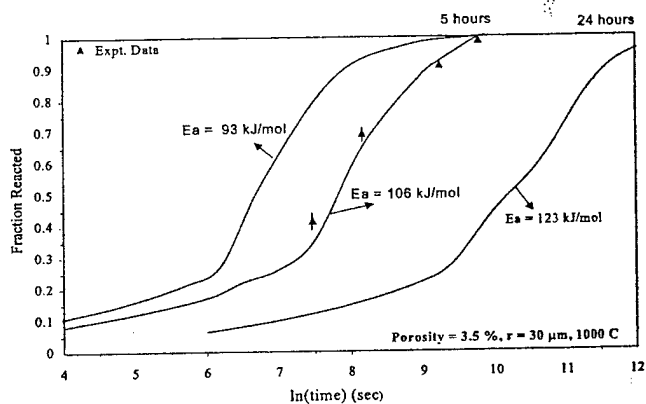


Fig. 11—Plot of reaction fraction as a function of time, for constant reaction temperature, particle size, and compact porosity, showing the influence of activation energy on the reaction mechanism.

greater than 1000 °C, however, synthesis of the shock-densified powders will be dominated by the self-sustained combustion mechanism.

The predictive model also provides the ability to separate the effects of individual variables like activation energy and density (porosity) to further the understanding of the reaction process. The effect of varying initial density (or porosity)

on the reaction fraction as a function of time, at a temperature of 1000 °C, constant activation energy of 106 kJ/mol, 30  $\mu\text{m}$  (average) particle size, and with the porosity ranging between 3.5 and 30 pct, is shown in Figure 10. As can be seen from the plot, a porosity of 10 pct and greater shows a takeover by the combustion reaction indicated by the steep slope revealing a rapid increase in the rate of reaction and completion of reaction in less than 1 hour. In contrast, the

denser (3.5 pct porosity) sample shows a more continuous increase in the rate of reaction and completion in ~5 hours. With increasing density (and decreasing porosity), the dissipation of heat generated due to the solid-state reaction is more efficient, leading to lack of heat localization and, consequently, the sample shows a reaction behavior dominated by solid state diffusion.

The apparent activation energy, calculated from differential thermal analysis, decreases with increasing shock-densification pressure, as illustrated in Figure 4. Hence, increasing densification "activates" the powder mixture by introducing dislocations, reducing the particle size, and bringing the reactants in more intimate contact because of increased flow and fracture caused by shock compression, which is expected to influence the subsequent reaction behavior. Figure 11 shows plots of fraction reacted as a function of time at 1000 °C revealing the effects of varying activation energy for a constant porosity (3.5 pct) and average particle size (30  $\mu\text{m}$ ). It can be seen that the activation energy influences the total time required for reaction completion, without significantly altering the slopes of the curves (change in reaction rate) at this temperature, thereby retaining the same dominant reaction mechanism (*viz.*, solid-state diffusion). Thus, lowering the activation energy for solid-state diffusion to 93 kJ/mol (because of shock densification) results in faster diffusion and, hence, shorter times for reaction completion.

Comparing the influence of apparent activation energy with that of particle size and compact density (or porosity) in Ti-Si compacts, it can be seen that the activation energy affects the time for reaction completion to a greater degree as compared to the effects of increasing particle size and density. At the same time, variation of activation energy maintains the same trend in reaction behavior, ensuring that reaction synthesis is dominated by solid-state diffusion at temperatures up to 1000 °C. On the other hand, changes in porosity influence the trend in reaction behavior, showing the reaction at 1000 °C being taken over by the combustion process at higher values of porosity.

## V. CONCLUSIONS

The reaction behavior of dynamically densified Ti-Si powder compacts was modeled to predict optimized conditions required to ensure that bulk synthesis occurs in the solid state, generating reaction products free from defects (predominantly porosity) associated with combustion-type reactions. The predictive model is based on mass and heat balance with the kinetics of the solid-state and dissolution-precipitation processes obtained using experimentally determined activation energies of the respective processes. The apparent activation energy for solid-state diffusion in the dynamically densified powder compacts was determined to be 93 to 123 kJ/mol for the Ti-Si compacts made under different shock-densification conditions. Complete reaction was observed to occur in the solid state at temperatures as low as 1000 °C, and hold time of 5 hours. At higher synthesis temperatures, the reaction almost instantaneously reached completion due to being taken over by the combustion process. The predictive model yields results consistent with those observed experimentally. It also enabled the study of the effects of individual variables,

which showed that the particle size and porosity dominate the reaction mechanism (solid state vs dissolution and reprecipitation) by controlling the temperature above which the reaction may be taken over by combustion synthesis. In contrast, reduction of the activation energy *via* shock compression influences the kinetics of the solid-state diffusion reaction. The predictive model can easily be applied to any type of reactive powder mixture compact to determine the reaction synthesis conditions required to ensure that bulk synthesis occurs in the solid state and to establish the influence of porosity, particle size, and degree of activation on the reaction behavior.

## ACKNOWLEDGMENTS

The work performed in this study was supported by the United States Army Research Office, under Grant No. DAAG55-97-1-0163, Dr. William Mullins, Program Monitor.

## REFERENCES

1. Z.A. Munir and U. Anselmi-Tamburini: *Materials Science Reports*, North-Holland, Amsterdam, 1989, vol. 3 (7-8), pp. 277-365.
2. Z.A. Munir: *Ceram. Bull.*, 1988, vol. 67 (2), pp. 342-48.
3. H.C. Yi and J.C. Moore: *J. Mater. Sci.*, 1990, vol. 25, p. 1159.
4. A.G. Merzhanov: in *Combustion and Plasma Synthesis of High-Temperature Materials*, Z.A. Munir and J.B. Holt, eds., VCH Publishers, New York, NY, 1990.
5. B.H. Rabin, B.E. Korth, and R.L. Williamson: *J. Am. Ceram. Soc.*, 1990, vol. 73 (7), pp. 2156-57.
6. H.A. Grebe, A. Advani, N.N. Thadhani, and T. Kottke: *Metall. Trans. A*, 1992, vol. 23A, pp. 2365-72.
7. J.C. LaSalvia: Ph.D. Dissertation, University of California at San Diego, San Diego, CA, 1994.
8. K.S. Vecchio, J.C. LaSalvia, M.A. Meyers, and G.T. Gray: *Metall. Trans. A*, 1992, vol. 23A, pp. 87-97.
9. R.A. Graham: *Proc. 3rd Int. Symp. on High Dynamic Pressures*, R. Cheret, ed., Association Francaise de Pyrotechnie, Paris, 1989, pp. 175-80.
10. N.N. Thadhani: *Progr. Mater. Sci.*, 1993, vol. 37, pp. 117-226.
11. R.A. Graham and N.N. Thadhani: in *Shock Waves in Materials Science*, A.B. Sawaoka, ed., Springer-Verlag, New York, NY, 1993, pp. 35-65.
12. E. Dunbar, N.N. Thadhani, and R.A. Graham: *J. Mater. Sci.*, 1993, vol. 28, pp. 2903-14.
13. J.H. Lee: Ph.D. Thesis, Georgia Institute of Technology, Atlanta, GA, 1997.
14. S.A. Namjoshi and N.N. Thadhani: *Scripta Mater.*, 1999, vol. 40 (12), pp. 1347-52.
15. J. Trambukis and Z.A. Munir: *J. Am. Ceram. Soc.*, 1990, vol. 73 (5), pp. 1240-45.
16. A. Calka and A.P. Radlinski: *Mater. Sci. Eng.*, 1991, vol. A134, pp. 1376-79.
17. R.A. Graham and D.M. Webb: in *Shock Waves in Condensed Matter—1983*, J.M. Asay, R.A. Graham, and G.K. Straub, eds., Elsevier Science Publishers, New York, NY, 1984, pp. 211-14.
18. S.A. Namjoshi: Ph.D. Dissertation, Georgia Institute of Technology, Atlanta, GA, 1999.
19. R.A. Graham: in *High-Pressure Explosive Processing of Ceramics*, R.A. Graham and A.B. Sawaoka, eds., Trans Tech Publications, Aedermannsdorf, Switzerland, pp. 29-64.
20. G.K. Williamson and W.H. Hall: *Acta Metall.*, 1953, vol. 1, p. 22.
21. G.K. Williamson and R.E. Smallman: *Phil. Mag.*, 1956, vol. 1, pp. 34-36.

22. G.K. Williamson and R.E. Smallman: *Acta. Cryst.*, 1954, vol 7, p. 574.
23. H.E. Kissinger: *Anal. Chem.*, 1957, vol. 29 (11), pp. 1703-06.
24. P.G. Boswell: *J. Thermal Anal.*, 1980, vol. 18, pp. 353-58.
25. R.E. Carter: *J. Chem. Phys.*, 1961, vol. 35, pp. 2010-15.
26. R.E. Carter: *J. Chem. Phys.*, 1961, vol. 35, pp. 1137-38.
27. R.F. Speyer: *Thermal Analysis of Materials*, Marcel-Dekker, New York, NY, 1994.
28. H.P. Klug and L.E. Alexander: *X-Ray Diffraction Procedures for Polycrystalline and Amorphous Materials*, John Wiley & Sons, New York, NY, 1974.
29. H.S. Carslaw and J.C. Jaeger: *Conduction of Heat in Solids*, Oxford Science Publications, Oxford, United Kingdom, 1960.
30. R.B. Bird, S.E. Stewart, and E.N. Lightfoot: *Transport Phenomenon*, John Wiley & Sons, New York, NY, 1976.

## **APPENDIX A4 - PREPRINT**

P.J. Counihan, A. Crawford, and N.N. Thadhani,  
“Influence of Dynamic Densification on Nanostructure  
Formation in  $\text{Ti}_5\text{Si}_3$  Intermetallic Alloy and Its Bulk  
Properties,” Materials Science and Engineering, A267, pp.  
26-35, 1999.

Reprinted from

# **MATERIALS SCIENCE & ENGINEERING**

**A**  
**Structural Materials: Properties,  
Microstructure and Processing**

---

Materials Science and Engineering A267 (1999) 26–35

Influence of dynamic densification on nanostructure formation in  
 $\text{Ti}_5\text{Si}_3$  intermetallic alloy and its bulk properties

P.J. Counihan, A. Crawford, N.N. Thadhani \*

*School of Materials Science and Engineering, Georgia Institute of Technology, Atlanta GA 30332-0245, USA*

Received 30 November 1998; received in revised form 18 January 1999



# Influence of dynamic densification on nanostructure formation in $\text{Ti}_5\text{Si}_3$ intermetallic alloy and its bulk properties

P.J. Counihan, A. Crawford, N.N. Thadhani \*

*School of Materials Science and Engineering, Georgia Institute of Technology, Atlanta GA 30332-0245, USA*

Received 30 November 1998; received in revised form 18 January 1999

## Abstract

Dynamic densification was used to consolidate mechanically amorphized Ti–Si alloy powders, using a three-capsule, plate–impact, gas–gun loading system at velocities of 300, 500, and 700 m s<sup>−1</sup>. The dense compacts were subsequently crystallized at annealing temperatures in the range of 800–1200°C, for time periods of 1–12 h. The compacts were observed to crystallize to a typically single-phase  $\text{Ti}_5\text{Si}_3$  compound and an ultra-fine grain microstructure, based on TEM and XRD analysis. The average grain size changed from ~50 nm upon heat treatment at 800°C for 1 h, to ~160 nm at 1200°C for 3 h, however, it remained stable (~115–125 nm) during annealing at a constant temperature of 1000°C and increasing heat treatment time from 1 to 12 h. In-situ crystallization studies performed by heating the dynamically-densified samples in the TEM at temperatures up to 900°C, revealed that the increase in fraction of amorphous to crystalline phase was occurring by an increase in the number density of nucleating crystallites, and not via significant growth of existing crystallites since their growth is inhibited by the impingement of the crystals. Vickers microhardness measurements showed values of 1200–1400 kg mm<sup>−2</sup> for grain size ranging from ~60 to 160 nm. While these microhardness values are ~80% higher than those for microcrystalline shock-densified  $\text{Ti}_5\text{Si}_3$  alloy, the fracture toughness values measured using the indentation method were observed to be ~2–4 MPa√m, which is typical of that of brittle ceramics. © 1999 Published by Elsevier Science S.A. All rights reserved.

**Keywords:** Ti–Si alloy; Dynamic densification; Nanostructure formation

## 1. Introduction

Nanostructured materials have unique properties which are derived from the fact that a high percentage of atoms (5–40%) are located at the grain boundaries [1–3]. The  $\text{Ti}_5\text{Si}_3$  titanium silicide intermetallic compound has properties that make it desirable for high-temperature, oxidation resistant structural applications, although it has limitations imposed by its brittle nature. It has been suggested that the mechanical properties of this intermetallic can be improved and sufficient ductility obtained by refinement of the grain structure to a nanoscale size [4]. However, fabrication of such nano-crystalline materi-

als in bulk form is difficult, since inter-particle friction and surface contaminants associated with fine scale powders can inhibit densification during static pressing, and hot-pressing can cause grain growth beyond the nano size range.

In recent studies, dynamic application of pressure has been used to overcome the problems associated with static densification methods. Aizawa et al. [5] have employed bulk mechanical deformation which involves repeated mechanical alloying and forging (termed ‘MA-forging’). This process combines mechanical mixing, microstructural refinement, and consolidation into one process, for simultaneous synthesis and consolidation of nanocrystalline intermetallic alloys. Milligan et al. [6] have used a rapid forging process employing an Instron testing machine with an heating chamber to consolidate nano-grain powders at ~550°C temperature and 525 MPa pressure.

\* Corresponding author. Tel.: +1-4048942651; fax: +1-4048949140.

E-mail address: naresh.thadhani@mse.gatech.edu (N.N. Thadhani)

Shock compaction of powders is a dynamic consolidation technique [7] which provides a viable method for densification of amorphous [8] as well as ultra-fine powders [9,10], without subjecting them to long term thermal excursions, thereby retaining the metastable structure. High densities of linear and planar defects can also be introduced during shock-compression of powders [11], which has been shown to enhance the density of nucleation sites during subsequent crystallization [12,13], and precipitation [14] treatments. Amorphous-to-crystalline phase transformation studies [15] on Ti–Si alloys at high (static) pressures, have shown formation of three types of products: (a) a supersaturated solid solution; (b) a single-phase intermetallic; or (c) a mixture of intermetallic phases. While the thermodynamic stability of the transformation products under dynamic pressure application would be expected to be similar to that during static densification, the rapid kinetics associated with dynamic densification process can inhibit phase separation and favor polymorphous phase changes [16]. In the present work the influence of dynamic (shock) densification on post-densification crystallization be-

havior of mechanically amorphized Ti–Si powders was investigated. Mechanical properties, including hardness and toughness of the resulting bulk nanocrystalline  $\text{Ti}_3\text{Si}_3$  alloy compacts were also determined.

## 2. Experimental procedure

Commercially acquired elemental titanium (Ti) and silicon (Si) powders were blended in a 5Ti:3Si molar ratio using a slow-speed V-blender, and subsequently mechanically amorphized using a SPEX 8000 ball mill. An AISI 304 stainless steel vial and hardened steel balls were used for milling. A ball-to-powder weight ratio of 5:1 was used for alloying 5 g batches of powders. Three types of powder mixtures were prepared: Mix I-titanium with crystalline silicon powder; Mix II-titanium with amorphous silicon powder; and Mix III-titanium with crystalline silicon plus 5 wt% amorphous carbon. Handling of the powders before and after milling, was performed in a controlled-atmosphere glove-box under a positive pressure of high-purity argon gas, although the loading (pressing) of the powders in the shock densification assembly was done under atmospheric conditions. Characteristics of the various starting powders are listed in Table 1, along with their vendor-provided purity levels.

The shock densification experiments were performed on the three different powder mixtures (Mix I, Mix II, and Mix III), using a three-capsule plate-impact gas-gun fixture (shown schematically in Fig. 1). Measured impact velocities of  $\approx 300$ , 500, and 700  $\text{m s}^{-1}$  were used to make 10 mm diameter by 3 mm thick final compacts. The shock impedance (product of density and wave speed) difference between the powder and the solid steel containment generates radial wave-focusing effects, which can result in non-uniform pressure distribution in the compact. As such a two-dimensional numerical simulation computer program, AUTODYNE-2D [17], was used to predict the stress-histories at different locations in the sample. Data for the bulk modulus, shear modulus, and yield strength of the various components used in the simulation were obtained from literature. The pressure-density compressibility curves used for determining the powder crush-strength were measured on the mechanically amorphized Ti–Si powders under static conditions. The autodyne-2D calculations showed that the peak pressure generated varies through the compacts, such that it is highest along the axial core and decreases to a more uniform pressure along the bulk of the outer regions. The peak shock pressure range in these 'axial' and 'bulk' regions of the compacts, calculated for the various impact conditions, are listed in Table 2. In the present

Table 1  
Starting powder characteristics

Material	Source	Morphology	Size	Purity (%)
Ti	Cerac (T-1147)	Crystalline	–325 mesh	99.5
Si	Cerac (S-1053)	Crystalline	–325 mesh	99.5
Si	Cerac (S-1049)	Amorphous	–325 mesh	99.999
C	Alfa (39274)	Amorphous	–200 mesh	99.99

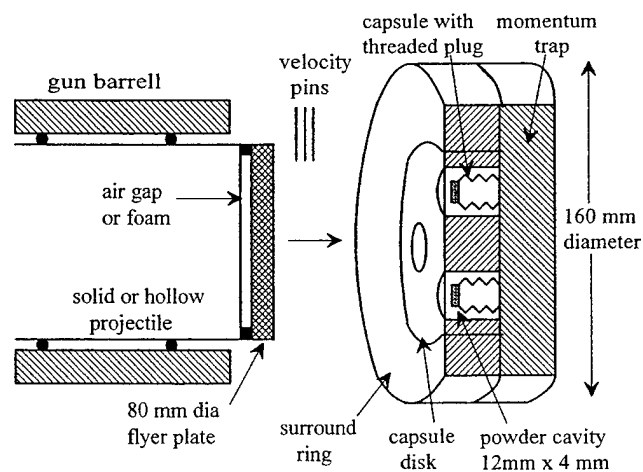


Fig. 1. Schematic of three-capsule plate-impact recovery fixture used with the 80 mm diameter gas-gun for dynamic densification experiments.

Table 2  
Calculated peak pressures and measured densities of recovered compacts

Impact velocity (m s <sup>-1</sup> )	Bulk pressure (GPa)	Axial pressure (GPa)
300	2–2.5	3.5–4.5
500	6–8	12–15
700	11–12	17–21

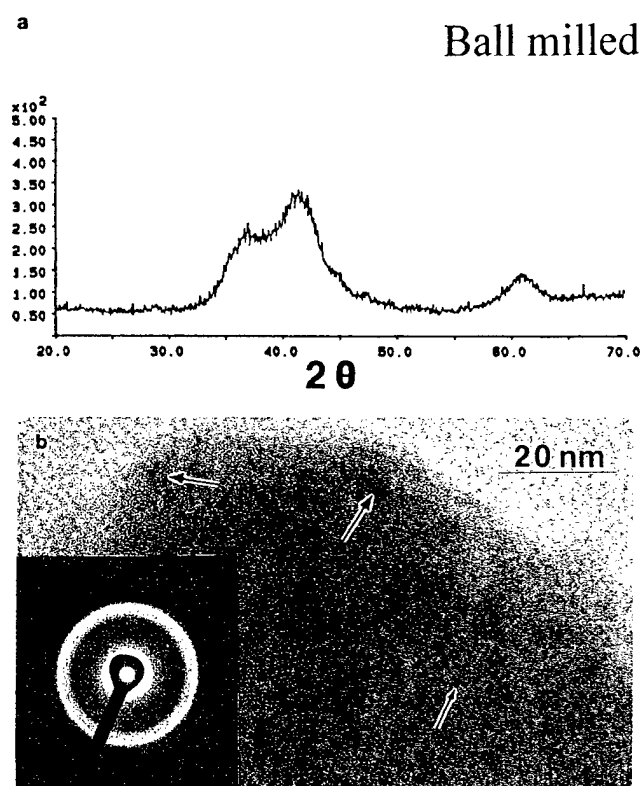


Fig. 2. Characteristics of ball-milled mechanically-amorphized powder. (a) XRD trace showing diffuse pattern, and (b) TEM bright field image showing a generally amorphous structure with < 10 nm interdispersed crystallites (marked by arrows).

Table 3  
Measured Densities of Recovered Dynamically Densified Compacts

Sample number	Contents	Impact velocity (m s <sup>-1</sup> )	Density (g cm <sup>-3</sup> )
I-1	Ti + x-Si	300	3.64 (84.3%)
I-2	Ti + a-Si	300	3.60 (83.5%)
I-3	Ti + x-Si + C	300	3.53 (81.8%)
II-1	Ti + x-Si	500	4.15 (96.2%)
II-2	Ti + a-Si	500	4.11 (95.3%)
II-3	Ti + x-Si + C	500	4.26 (98.7%)
III-2	Ti + a-Si	700	4.36 (100%)

work, all characterization of shock-densified compacts, as well as all post-densification crystallization treatments, were performed on samples cut from the outer 'bulk' regions.

The crystallization heat treatments were performed in a tube furnace, using high-purity argon gas. The structural characteristics, including grain size and lattice parameter, were determined using X-ray diffraction analysis. XRD analysis was performed using step sizes of 0.04° and count time of 250–350 s per step. The profiles were then corrected by stripping the  $K\alpha_2$  doublet and subtracting the contribution from instrumental broadening, and fit using a Peakfit™ software. The grain size was then determined using the Williamson–Hall approach [18]. Transmission electron microscopy (TEM) was also performed to estimate the crystallite size and observe the evolution of crystallites. For TEM analysis, samples of the mechanically amorphized as well as shock-densified compacts were prepared by grinding into powder form, while the heat-treated (crystallized) compacts were sectioned into 3 mm diameter disks and ion milled to electron transparency. In-situ crystallization experiments were also performed at temperatures of up to 900°C, using a hot-stage in the TEM, to investigate the crystallization behavior of the shock-densified Ti–Si amorphous powder compacts. The properties of the crystallized shock-densified materials were characterized based on microhardness and fracture toughness measurements using the indentation method.

### 3. Results and discussion

#### 3.1. Mechanical alloying and dynamic densification

In the present work mechanical alloying of elemental Ti and Si powders was employed to form an amorphous compound of stoichiometry corresponding to the  $Ti_5Si_3$  intermetallic. Ball milling of the powders for 24 h, using a ball-to-powder weight ratio of 5:1, resulted in formation of mechanically-alloyed polycrystalline aggregates of  $\sim 1 \mu\text{m}$  diameter. The aggregate particles had a generally amorphous structure as revealed by the diffuse XRD pattern in Fig. 2 (a). TEM imaging and selected area diffraction shown in Fig. 2 (b) revealed a generally amorphous matrix with a few interdispersed < 10 nm size crystallites (marked by arrows). Chemical analysis of oxygen and nitrogen was performed on the mechanically alloyed amorphous Ti–Si powder mixture at a commercial lab (National Science Laboratories). The analysis showed presence of as much as 1.82 wt% O and 0.66 wt% N. These contamination levels are greater than those present in the starting powders as listed in Table 1, indicating pick up of O and N possibly during handling of the powders in the glove box, or during ball milling, since the adsorbed gases can dissolve rapidly in the amorphous Ti–Si compound.

The mechanically amorphized Ti–Si alloy powders were dynamically (shock) densified using the three-capsule plate–impact gas–gun geometry, and recovered as single-piece disks. Table 3 lists the measured densities of the various dynamically densified compacts. The compacts recovered at  $300 \text{ m s}^{-1}$  impact velocity were  $\sim 82\text{--}84\%$  dense, while those obtained upon compaction at  $500 \text{ m s}^{-1}$  were  $\sim 95\text{--}99\%$  dense and those at  $700 \text{ m s}^{-1}$  were  $\sim 100\%$  dense. The number of cracks in the consolidated compacts was found to increase with in-

creasing impact conditions, with the  $300 \text{ m s}^{-1}$  sample showing only a few axial cracks, while the  $700 \text{ m s}^{-1}$  sample showed both radial and circumferential cracks. Amongst the different Mix I, II, and III types, only minor differences in compact characteristics (density and number of cracks) were observed.

XRD characterization of the shock densified compacts revealed that the generally amorphous state had been retained in the 300 and  $500 \text{ m s}^{-1}$  samples, as shown in Figs 3 (a) and (b), respectively, while the compact

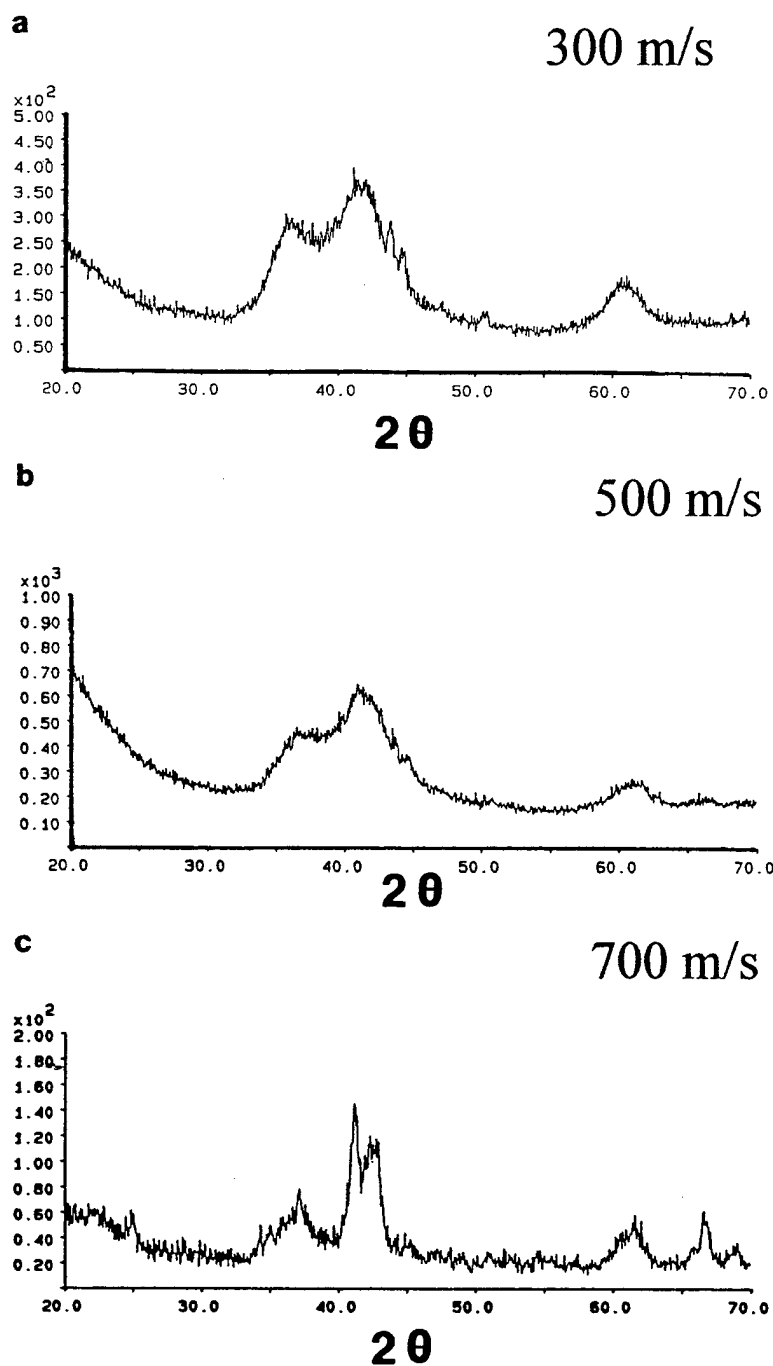


Fig. 3. XRD characterization of mechanically amorphized and subsequently dynamically densified powder compacts at (a) 300; (b) 500; and (c)  $700 \text{ m s}^{-1}$  impact velocity, showing partial crystallization of amorphous Ti–Si compound.

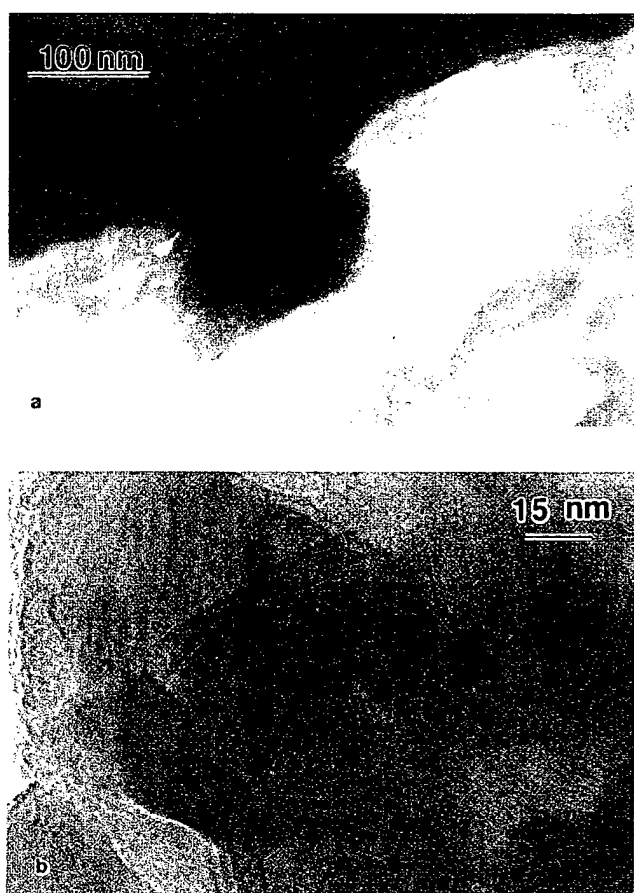


Fig. 4. Dark field TEM image revealing (a) inter-dispersed crystallites of  $\sim 10$ – $40$  nm size in the generally amorphous matrix and (b) bright field image showing presence of planar defects in crystalline regions of the compact dynamically densified at  $500 \text{ m s}^{-1}$ .

consolidated at  $700 \text{ m s}^{-1}$  showed a number of broad crystalline peaks, as illustrated in Fig. 3(c). TEM imaging of the shock densified  $500 \text{ m s}^{-1}$  compact revealed inter-dispersed crystallites of  $\sim 10$ – $40$  nm size in the generally amorphous matrix, as shown in the bright field image in Fig. 4 (a). At higher magnifications, evidence of planar defects was also observed in some of the crystalline grains of the compact, as shown in Fig. 4 (b).

### 3.2. Crystallization characteristics of dynamically densified compacts

Differential thermal analysis (DTA) of the mechanically amorphized powder revealed primary crystallization with a peak at  $\sim 630^\circ\text{C}$ , followed by a secondary crystallization at  $\sim 760^\circ\text{C}$ , as shown in Fig. 5 (a). In contrast, the shock-densified amorphous powder compacts typically revealed a single exotherm at  $\sim 630^\circ\text{C}$ , as shown in Fig. 5 (b), corresponding to polymorphous crystallization to a single phase com-

pound. Consequently, all crystallization heat treatments on the shock densified compacts were performed at temperatures of  $800^\circ\text{C}$  and above, for time periods of 1–12 h.

The average crystallite size of the  $\text{Ti}_5\text{Si}_3$  phase in the annealed shock-densified compacts was obtained from XRD line-broadening analysis. The  $500 \text{ m s}^{-1}$  compacts of the three types of mixtures, were annealed for 1 h at 800, 1000 and  $1200^\circ\text{C}$ , and at a constant temperature of  $1000^\circ\text{C}$ , for different times (1, 3 and 12 h). The overall variation of average crystallite size with annealing temperature and time for the various powder mixture types, is plotted in Fig. 6 (a, b). It is interesting to note that while the grain size changes from  $\sim 46$  to  $60$  nm at  $800^\circ\text{C}$  to about  $127$ – $157$  nm at an annealing temperature of  $1200^\circ\text{C}$  at a constant time of 1 h, it remains stable at  $\sim 114$ – $124$  nm as a function of annealing time between 1 and 12 hours at a constant  $1000^\circ\text{C}$  temperature. In addition, the dependence of annealing temperature and time on grain size was relatively independent of the powder mixture type (Mix I, II, and III).

### 3.3. In-situ crystallization

In-situ crystallization of the shock-densified mechanically-amorphized Ti–Si powder compacts was performed to more clearly delineate the evolution of crystallites. Heating of a thin-foil sample was carried out in the TEM, from  $500$  to  $900^\circ\text{C}$  in steps of  $50^\circ\text{C}$ . The sample was held at each temperature for  $\approx 10$  min. Bright field images and selected area diffraction patterns were taken from the same location at different temperatures to monitor the progress of the crystallization process. Fig. 7 shows bright field images of the region viewed at six different temperatures, revealing interdispersed crystallites (few to  $40$  nm) in the generally amorphous matrix, and Fig. 8 shows the corresponding diffraction patterns of this same region at different temperatures. In general, as shown in Fig. 7, it can be seen that with increase in temperature, the dispersed  $\text{Ti}_5\text{Si}_3$  crystallites undergo limited growth and their size changes to about twice their original size, e.g. the fine  $\sim 15$  nm crystals grow to  $\sim 25$  nm size, and the coarser  $60$  nm crystallites grow to no more than  $\sim 80$  nm in size. At the same time, the diffraction patterns shown in Fig. 8, reveal significant increase in the sharpness and number of diffraction spots in the rings, indicating significantly increased crystallinity. This suggests that with increasing annealing temperature, crystallization of the shock-densified amorphous Ti–Si compacts is occurring mainly via increase in the number density of nucleating crystallites, rather than significant growth of the existing crystals. It is possible that linear and planar defects introduced during shock compression,

provide the nucleation sites for crystallite formation during subsequent annealing, and their large number density limits the growth of existing crystallites due to impingement. More detailed analysis of the role of shock formed defects on the evolution of crystallites, and influence of shock loading conditions on defect generation in the densified amorphous powder compacts, is currently underway.

### 3.4. Microstructure and microhardness correlation

Microhardness measurements were made on the samples of fully crystallized shock densified compacts, using a Leco Vickers microhardness tester. At least ten measurements were made on relatively clean (crack-free) regions of the compacts. The standard deviations of the hardness values were in the range of 2–5% of the average values. The correlation of hardness versus grain size is illustrated in Fig. 9, showing (a) Hall-Petch inverse-square root dependence and (b) direct linear dependence. The average microhardness values of the different compacts were observed to be

in the range of 1200–1400 kg mm<sup>-2</sup> in the fully annealed and crystallized (at 800–1200°C, 1 to 12 h) samples. Samples of 300 m s<sup>-1</sup> compacts showed lower hardness values which may be due to the presence of porosity in this sample. In fact, the hardness was observed to increase along with increase in grain size at higher temperatures because of sintering. Thus, ignoring the data for points for the 300 m s<sup>-1</sup> compacts, and considering that the standard deviation in hardness measurements is ~2–5%, it appears that the hardness increases from 1200 to 1400 kg mm<sup>-2</sup> with grain size increase from ~60 to 140 nm, following which the hardness decreases slightly with further increase in grain size to ~160 nm. The lack of data points beyond the 160 nm grain size (due to limited grain growth up to temperatures as high as 1200°C, precludes the determination of the Hall-Petch effect. However, as indicated in Fig. 9, it is clear that maximum hardness values obtained for the shock-densified Ti<sub>5</sub>Si<sub>3</sub> compacts with 60–160 nm grain size are ~80% higher than those for microcrystalline (~2–5

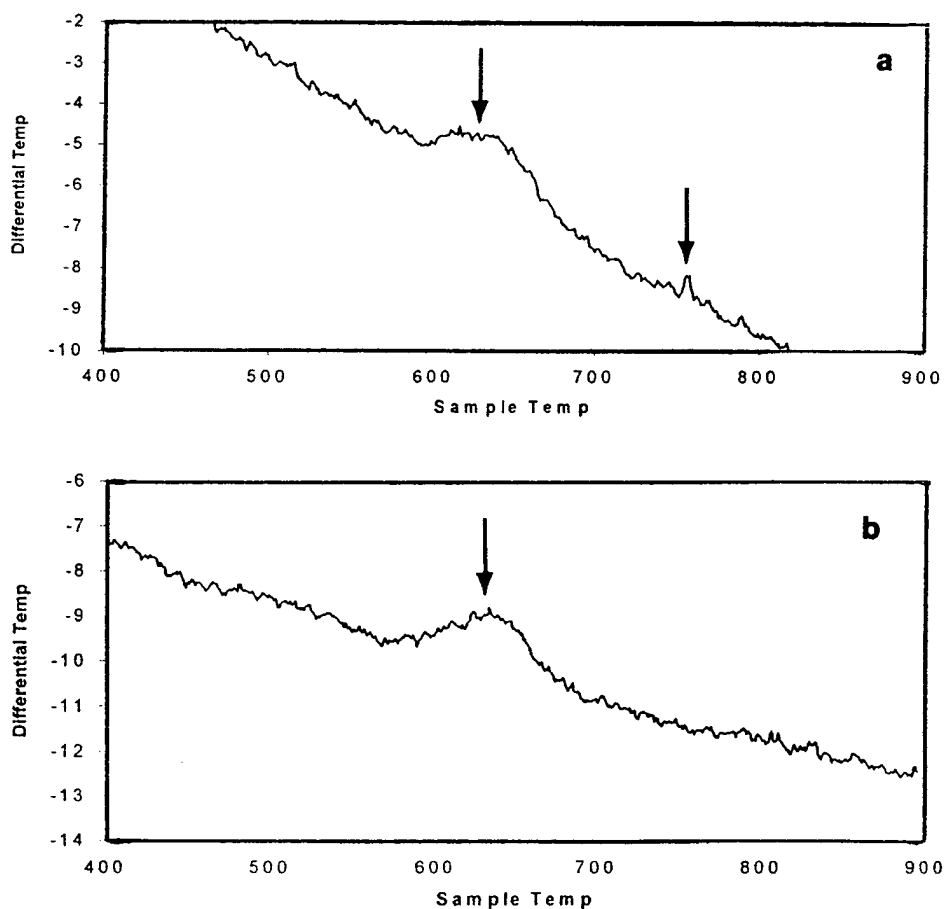


Fig. 5. DTA traces showing (a) primary and secondary crystallization in unshocked mechanically amorphized powders and (b) single polymorphous crystallization in shock densified powder compact. Peaks of crystallization exotherms are indicated by arrows.

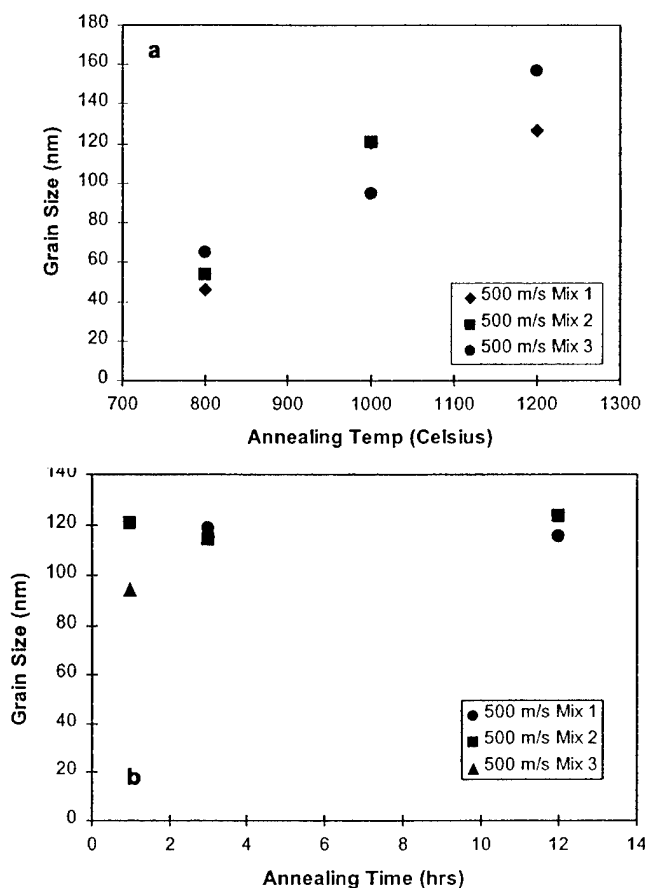


Fig. 6. Plot showing crystallite size variation with (a) annealing temperature at constant time (1 h), and with (b) annealing time at constant temperature (1000°C).

$\mu\text{m}$  grain size)  $\text{Ti}_5\text{Si}_3$  alloy prepared by shock densification and reaction synthesis [19].

Similar increase in microhardness values has been observed by Yamasaki et al. [12], on shock-densified mechanically-amorphized compacts (at 32.6 GPa) of  $\text{Ti}_{50}\text{Si}_{50}$  alloy annealed at 750°C, in which they observed a maximum value as high as 1700 kg mm<sup>-2</sup>. However, with further annealing at 1000°C, their microhardness values dropped to less than 1000 kg mm<sup>-2</sup>, which was attributed by the authors to be due to the formation of a significant fraction of the  $\text{TiSi}_2$  phase upon complete crystallization of the  $\text{Ti}_{50}\text{Si}_{50}$  amorphous compound. In the present work, the mechanically amorphized compound was observed to polymorphously crystallize to the  $\text{Ti}_5\text{Si}_3$  phase.

The fracture toughness of the shock-densified and crystallized compacts was also determined using the indentation method. Vickers indentations made with a 5 kg load exhibited corner cracks. The indentations and cracks were photographed with an optical microscope at 200–300 times magnification, and further enlarged to a magnification of 940 $\times$ , to better determine the crack termination locations. At least

three indentations were considered for each sample, and the average crack lengths were then used to calculate the fracture toughness for both Medial and Palmqvist type of cracks [20]. The fracture toughness equations used for the corresponding types of cracks are:

$$\text{Palmqvist cracks: } (K_{IC}\Phi/Ha^{1/2})(H/E\Phi)^{2/5} \\ = 0.035(l/a)^{-1/2}$$

$$\text{Medial cracks: } (K_{IC}\Phi/Ha^{1/2})(H/E\Phi)^{2/5} \\ = 0.129(c/a)^{-3/2}$$

where,  $K_{IC}$  is the fracture toughness;  $\Phi$  represents the constraint factor  $\cong 3$ ;  $H$  is the hardness;  $a$  is half the indent diagonal;  $E$  is Young's modulus;  $c$  is the crack length measured from the center of the indentation;  $l$  is the crack length measured from the corner of the indentation. Based on a Young's modulus of 156 GPa [21], the fracture toughness was determined to be around 2–3 MPa m<sup>-1/2</sup> in the various samples.

Table 4 lists values of fracture toughness reported for coarse-grained  $\text{Ti}_5\text{Si}_3$  intermetallic alloys. In general, it can be seen that for these coarse-grained  $\text{Ti}_5\text{Si}_3$  intermetallic, the fracture toughness appears to increase with decreasing grain size. While the fracture toughness values of the nanocrystalline  $\text{Ti}_5\text{Si}_3$  produced in the present work are typical of those of the coarse-grained alloy and similar other intermetallics having complex crystal structures, an increase in the fracture toughness due to the nanocrystalline grain size is not observed. This lack of increase in toughness could be attributed to the presence of oxygen and nitrogen impurities present in the  $\text{Ti}_5\text{Si}_3$  compacts. It was not totally confirmed if the impurities are in solution or are forming precipitates (nitrides/oxide). No evidence of extraneous peaks was observed in the X-ray diffraction scans. Values of the lattice parameters for  $\text{Ti}_5\text{Si}_3$  obtained from the XRD scans of the various crystallized compacts showed ' $a$ ' = 0.7431 to 0.7445 nm and ' $c$ ' = 0.5135–0.5196 nm. These values are slightly different from those reported in the literature (' $a$ ' = 0.7444 nm and ' $c$ ' = 0.5143). Hence, it is possible that the oxygen and nitrogen contaminations are present primarily as dissolved impurity phases in the nanocrystalline  $\text{Ti}_5\text{Si}_3$  intermetallic, which may influence both the fracture toughness and the microhardness values of the nanocrystalline  $\text{Ti}_5\text{Si}_3$  compacts. Further work is necessary to obtain compacts free from oxygen and nitrogen contamination to fully deduce the influence of nano and ultra-fine grain structure on the mechanical properties of the dense  $\text{Ti}_5\text{Si}_3$  intermetallic alloys.

#### 4. Summary and conclusions

Shock densified compacts of mechanically amorphized Ti–Si alloy powder were polymorphously crystallized to  $\text{Ti}_5\text{Si}_3$  compound with ultra-fine grain microstructure. The average grain size changed from

~ 50 nm upon heat treatment at 800°C to a maximum of ~ 90 nm at temperatures as high as 1200°C, for time periods of up to 12 h. In-situ crystallization in the TEM revealed that continued crystallization occurred by increase in the number density of the crystallites and not via growth of crystallites. The autocatalytic crystalliza-

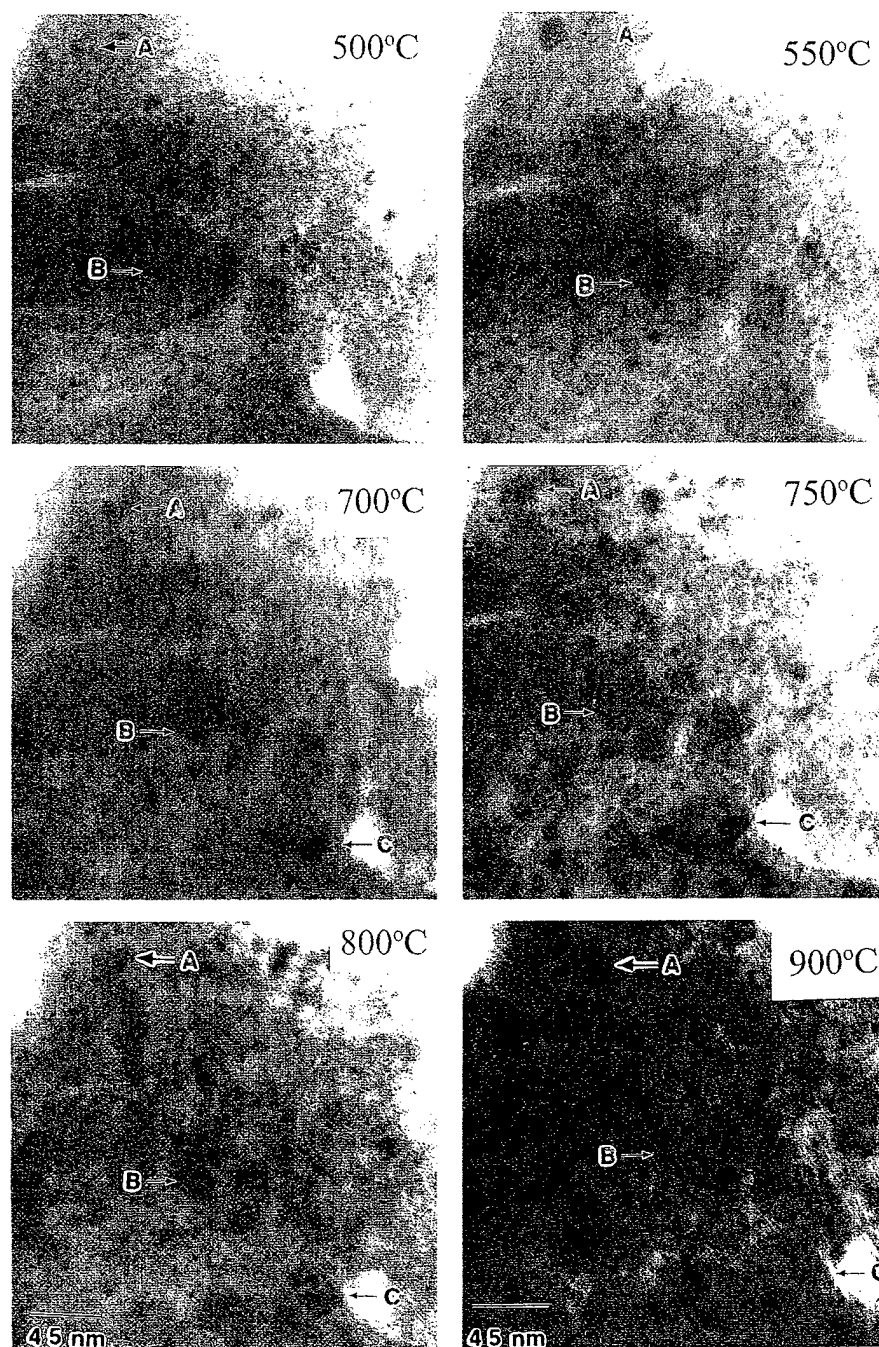


Fig. 7. Bright field images of a region of a shock densified powder compact revealing interdispersed crystallites (marked by arrows at 'A', 'B', and 'C') in a generally amorphous matrix at different temperatures between 500 and 900°C, showing only limited growth of crystallites from approximately 15–25 nm size.

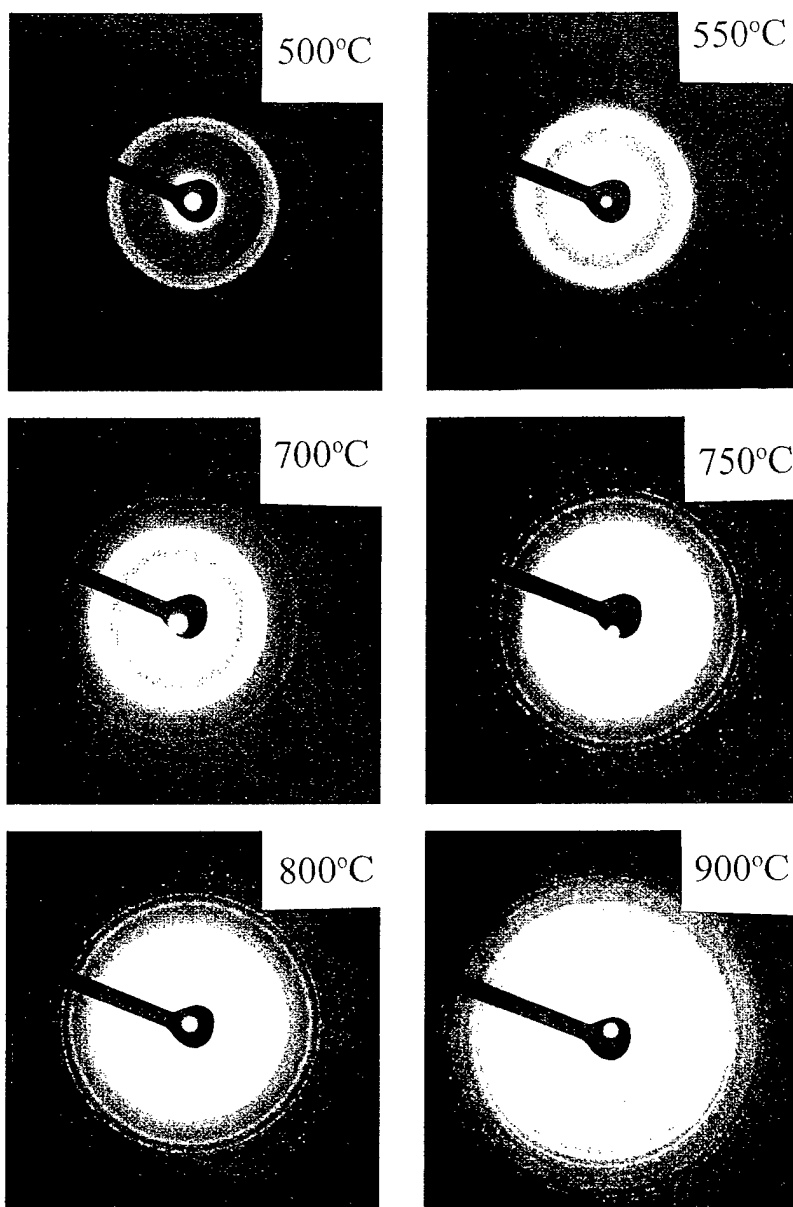


Fig. 8. Diffraction patterns corresponding to the bright field images of the region shown in Fig. 8, at different temperatures between 500 and 900°C, showing increasing degree of crystallization.

tion during annealing results in impingement of the grains thereby inhibiting their growth. Vickers microhardness measurements showed a peak value of  $\sim 1400 \text{ kg mm}^{-2}$  for a grain size of  $\sim 80 \text{ nm}$ , following which a decrease in hardness to  $\sim 1300 \text{ kg mm}^{-2}$  was observed with further increase in grain size. These Vickers microhardness values are  $\sim 80\%$  higher than those for microcrystalline shock-densified  $\text{Ti}_5\text{Si}_3$  alloy. The fracture toughness values measured using the indentation method were observed to be

$\sim 2\text{--}4 \text{ MPa}$ , typical of coarse-grained microcrystalline  $\text{Ti}_5\text{Si}_3$  intermetallics.

#### Acknowledgements

Funding for this research was provided by ARO Grant No. DAAH04-93-0062 and DAAGSS-97-1-0163. The help of Professor Z.L. Wang, and Yolande Berta with the TEM analysis is much appreciated.

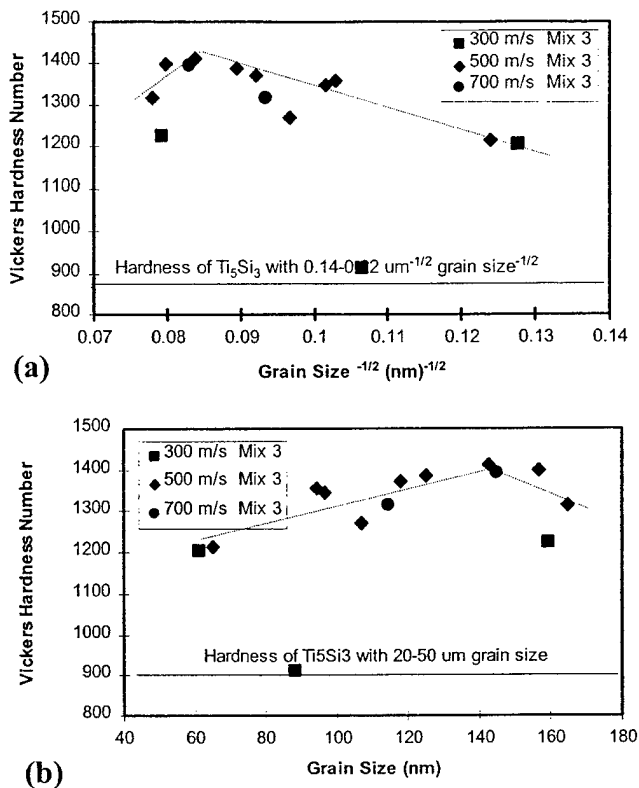


Fig. 9. Variation of hardness with crystallite size based on (a) inverse-square root (Hall-Petch) dependence and (b) direct linear dependence.

Table 4

Fracture toughness of coarse-grained Ti<sub>5</sub>Si<sub>3</sub>

Grain size (μm)	Fracture toughness (MPa √m)	Reference
20–50	2.1	Rosenkranz et al., 1992, Ref. [22]
10–30	2	Ruess and Vehoff, 1990, Ref. [23]
6–10	3.2	Mitra, 1998, Ref. [24]
6	5	Ruess and Vehoff, 1990, Ref. [23]

## References

- [1] H. Gleiter, Prog. in Mater. Sci. 33 (4) (1989) 223–315.
- [2] R. Rosenkranz, G. Frommeyer, W. Smarsly, Mater. Sci. Eng. A152 (1992) 288–294.
- [3] R.S. Averbach, Mater. Sci. Eng. A166 (1,2) (1993) 169–177.
- [4] A. Calka, J. Mater. Sci. Lett. 10 (1991) 1330–1333.
- [5] T. Aizawa, Mater. Trans. JIM 36 (2) (1995) 138–149.
- [6] W.W. Milligan, S.A. Hackney, M. Ke, E.C. Aifantis, Nanostructured Mater. 2 (1993) 267.
- [7] W.H. Gourdin, Prog. Mater. Sci. 30 (1) (1986) 39–80.
- [8] D. Raybould, D.G. Morris, G.A. Cooper, J. Mater. Sci. 14 (1979) 2523.
- [9] M. Jain, T. Christman, Acta Metall. 42 (1994) 1901–1911.
- [10] G. Korth, R.L. Williamson, Dynamic Consolidation of Metastable Nanocrystalline Powders, EG&G Idaho National Labs., unpublished results, 1994.
- [11] T. Chen, J.M. Hampikian, and N.N. Thadhani, Acta Met and Mater. 1999, in press.
- [12] T. Yamasaki, Y. Ogino, K. Morishita, K. Fukuota, T. Atou, Y. Syono, Mater. Sci. Eng. A179/A180 (1994) 220–223.
- [13] S.C. Glade, N.N. Thadhani, Metall. Mater. Trans. 26A (1995) 2565–2569.
- [14] N.N. Thadhani, A.H. Mutz, T. Vreeland, Acta Metall 37 (3) (1989) 897–908.
- [15] W.K. Wang, H. Iwasaki, C. Suryanarayana, T. Matsumoto, J. Mater. Sci. 18 (1983) 3765.
- [16] R.L. Freed, Acta Metall. 28 (1980) 103.
- [17] AUTODYN-2D/2.8, Non-Linear Dynamic Modeling Software, Century Dynamics, 1995.
- [18] G.K. Williamson, W.H. Hall, Acta Metall. 1 (1953) 22.
- [19] S. Namjoshi, N.N. Thadhani, Reaction Synthesis of Shock Densified Ti-Si Powder Mixtures, in: S.C. Schmidt, D.P. Dandekar, J.W. Forbes (Eds.), Shock-Compression of Condensed Matter-1997, AIP, 1998, pp. 659–663.
- [20] A.G. Evans, T.R. Wilshaw, Acta Metall. 24 (1976) 939–952.
- [21] G. Frommeyer, R. Rosenkranz, W. Smarsly, Mater. Sci. Eng. A152 (1992) 290.
- [22] R. Rosenkraz, G. Frommeyer, W. Smarsly, Mater. Sci. Eng. A152 (1992) 288–294.
- [23] S. Ruess, H. Vehoff, Scripta Metall. Mater. 24 (1990) 1021–1026.
- [24] R. Mitra, Metall. Mater. Trans. 29A (1998) 1629–1641.

## **APPENDIX A5 - PREPRINT**

T. Chen, J. Hampikian, and N.N. Thadhani, "Synthesis, Microstructure, and Properties of Shock Compacted Nanocrystalline NiAl alloy," Acta Mater., Vol. 47(8), 2567-2579, 1999.



PERGAMON

Acta mater. Vol. 47, No. 8, pp. 2567–2579, 1999

© 1999 Acta Metallurgica Inc.

Published by Elsevier Science Ltd. All rights reserved

Printed in Great Britain

1359-6454/99 \$20.00 + 0.00

PII: S1359-6454(99)00059-2

## SYNTHESIS AND CHARACTERIZATION OF MECHANICALLY ALLOYED AND SHOCK-CONSOLIDATED NANOCRYSTALLINE NiAl INTERMETALLIC

T. CHEN, J.M. HAMPIKIAN† and N.N. THADHANI

School of Materials Science and Engineering, Georgia Institute of Technology, 778 Atlantic Drive, Atlanta, GA 30332-0245, U.S.A.

(Received 28 April 1998; accepted in revised form 4 February 1999)

**Abstract**—The synthesis, microstructural characterization and microhardness of nanocrystalline B2-phase NiAl intermetallic are discussed in this paper. Nanophase NiAl powders were prepared by mechanical alloying of elemental Ni and Al powders under an argon atmosphere for different times (0–48 h). The alloyed nanocrystalline powders were then consolidated by shock compaction at a peak pressure of 4–6 GPa, to 83% dense compacts. Characterization by transmission electron microscopy (TEM) revealed that the microstructure of the shock-consolidated sample was retained at the nanoscale. The average crystallite size measurements revealed that mechanically alloyed NiAl grain size decreased from  $48 \pm 27$  to  $9 \pm 3$  nm with increasing mechanical alloying time from 8 to 48 h. The long-range-order parameters of powders mechanically alloyed for different times were determined, and were observed to vary between 0.82 for 5 h and 0.63 for 48 h of milling time. Following shock compaction, the long-range-order parameter was determined to be 0.76, 0.69 and 0.66, respectively, for the 16, 24 and 48 h alloyed specimens. Both the mechanically alloyed nanocrystalline NiAl powder and the shock-consolidated bulk specimen showed evidence of grain boundary dislocations, subgrains, and distorted regions. A large number of grain boundaries and defects were observed via high resolution TEM (HRTEM). Shear bands were also observed in the mechanically alloyed NiAl intermetallic powders and in the shock-consolidated compacts. Microhardness measurements of shock-consolidated material showed increasing microhardness with increasing crystallite size refinement, following Hall–Petch behavior. © 1999 Acta Metallurgica Inc. Published by Elsevier Science Ltd. All rights reserved.

**Keywords:** Powder consolidation, dynamic compaction; Mechanical alloying; Hardness; Shear bands

### 1. INTRODUCTION

Nanocrystalline materials, defined as polycrystalline solids having crystallite sizes usually less than 100 nm, can exhibit unique properties due to the large fraction of grain boundaries that they possess. In particular, the strength, ductility, and diffusion kinetics, among other mechanical and chemical properties, may be significantly enhanced for nanocrystalline materials in comparison with materials with conventional grain sizes [1–4].

In the nickel–aluminum alloy system, equiatomic NiAl (B2-phase) exhibits a high melting temperature (1640°C), a low density (5.9 g/cm<sup>3</sup>, which is approximately 2/3 that of Ni based superalloys), metal-like electrical and thermal conductivity, and a lower DBTT relative to other intermetallics. NiAl has potential applications such as in hot sections of gas turbine engines for aircraft-propulsion systems, bond coats under thermal barrier coatings, electronic metallization compounds in advanced semi-

conductor heterostructures, and surface catalysts [5]. Most research efforts on improving the ductility of NiAl have been focused on the addition of metal-oids (e.g. B) to pin the grain size.

The synthesis of nanocrystalline alloys and intermetallic compounds by ball milling has been successfully achieved by several researchers [6–10]. In the case of nanocrystalline NiAl alloy powders, subsequent consolidation has been accomplished by means of hot pressing [10], vacuum hot pressing [10], and extruding [11] at elevated temperatures (1275–1473 K). Long-term temperature excursions associated with these processes can allow primary recrystallization and grain growth. Smith has reported sinter-forging of mechanically alloyed nanocrystalline NiAl alloy [8], with a retained grain size of  $72 \pm 41$  nm.

Shock-wave compaction has been employed for consolidation of powders of nanocrystalline alloys [1,12], as well as metastable (amorphous) compounds [13,14]. The application of a shock-wave produces a high pressure of microsecond duration and temperatures moderate enough to attain

†To whom all correspondence should be addressed.

bonding between powders, resulting in compacted samples with high density and retained parent structure [15]. In this study, nanocrystalline NiAl alloy powders were first obtained by ball milling elemental Ni and Al powders, which were subsequently shock-consolidated to produce dense compacts for microstructural characterization and hardness measurements.

## 2. EXPERIMENTAL

Ni and Al powders of nominal purity of 99.9% and 99.97%, and particle sizes ranging between 45–150  $\mu\text{m}$  and 45–75  $\mu\text{m}$ , respectively, were mixed at a 1:1 mole ratio and sealed in a plastic bottle, which was placed in a V-blender for blending the powders for 24 h. For mechanical alloying, approximately 5 g of powder, with two steel balls (ball-to-powder weight ratio of approximately 3.3 to 1), were put into the AISI 304 stainless steel milling vial. The milling was performed in a Spex 8000 laboratory ball mill for time periods ranging between 0 and 48 h at room temperature. It was found that the 5 h run was sufficient for the Ni and Al to alloy and form intermetallic NiAl. Powders alloyed for 16, 24 and 48 h were used for compaction experiments. At all times the powders were handled and sealed in containers in a glove box under argon atmosphere in order to minimize exposure to the ambient.

Shockwave compaction was accomplished with a three-capsule, plate impact fixture, using the Georgia Tech 80 mm diameter single-stage gas gun. Details of the fixture and gun loading technique are described elsewhere [16]. The powders were packed in capsules, prior to shock consolidation, at about 70% of theoretical maximum density. Impact experiments were performed using an aluminum projectile and a 5 mm thick stainless steel flyer plate accelerated in the 80 mm diameter gas gun, at an impact velocity measured to be approximately 400 m/s. Peak pressures corresponding to these loading conditions were computed using a two-dimensional AUTODYNE-2D hydrodynamic code [16]. The hydrodynamic properties of a mechanical mixture of Ni and Al were considered for the simulation. Following an initial pressure wave of 1 GPa, a bulk peak pressure of 4–6 GPa was predicted due to two-dimensional radial wave-focusing effects. Since two-dimensional wave-focusing effects dominate the loading conditions, the peak pressures generated are independent of material properties. The samples were recovered in the form of 10 mm diameter by 3 mm thick discs. The density of the samples following shock compaction was determined by the Archimedes method.

X-ray diffraction analysis was performed with a Philips X-1800 diffractometer in step scanning mode using Ni-filtered  $\text{CuK}\alpha$  radiation to determine the crystal structure and crystallite size. Scanning electron microscopy (SEM) was carried out with a

Hitachi S-800 field emission scanning electron microscope to characterize the milled powder morphology and the compact surfaces. Transmission electron microscopy (TEM) characterization utilized using a 200 kV field emission transmission electron microscope. TEM samples were prepared by ultrasonically dispersing the mechanically alloyed NiAl powder in ethanol and then placing one drop onto a holey carbon support grid. The shock-consolidated samples were cut longitudinally along the direction of shock-wave propagation, for characterization of the cross-section and for preparing TEM samples which were made using an ion polishing system at low incident angle (Gatan PIPS).

Shock-consolidated samples were tested for Vickers microhardness using a Leco DM-400F Hardness Tester. The indentations were made in regions of the specimens that appeared to have nearly full density.

The crystallite sizes of both mechanically alloyed powder and shock-compacted bulk NiAl specimen were measured by the ASTM linear intercept method on the bright and dark field TEM micrographs, which yields an area-weighted average grain size.

## 3. RESULTS

In this work nanocrystalline NiAl intermetallic alloy powders were prepared by mechanical alloying elemental powders for a period of 0–6 h (at 1 h intervals) 8, 16, 24 and 48 h. The 16, 24 and 48 h ball-milled powders were subsequently shock-consolidated to obtain bulk compacts, at a peak pressure of approximately 4–6 GPa using a gas gun system for impact loading.

### 3.1. Mechanical alloying of nanocrystalline NiAl intermetallic alloy

The synthesis of nanocrystalline NiAl alloy, by ball milling (from 0–48 h) elemental Ni and Al powders mixed in a 1:1 atom ratio, was confirmed by X-ray diffraction analysis. As shown in the XRD traces in Fig. 1(a), almost complete alloying is achieved beyond 5 h of milling time. The degree of order of the NiAl powder was calculated from the square root of the intensity ratio of the superlattice reflection (100) to the fundamental reflection (110), by normalizing this ratio to the calculated intensity ratio for completely ordered NiAl [17]. The variation of long-range-order parameter ( $S$ ) for the mechanically alloyed NiAl, as a function of milling time is shown in Fig. 1(b).

The morphology of alloyed powders produced at different alloying times was investigated via SEM analysis. As shown in Figs 2(a)–(f), the early stages of mechanical alloying (2 h and 5 h) result in the formation of powder agglomerates having a wide range in size (from 5  $\mu\text{m}$  to 430  $\mu\text{m}$ ). The particles agglomerate as a result of the repeated welding

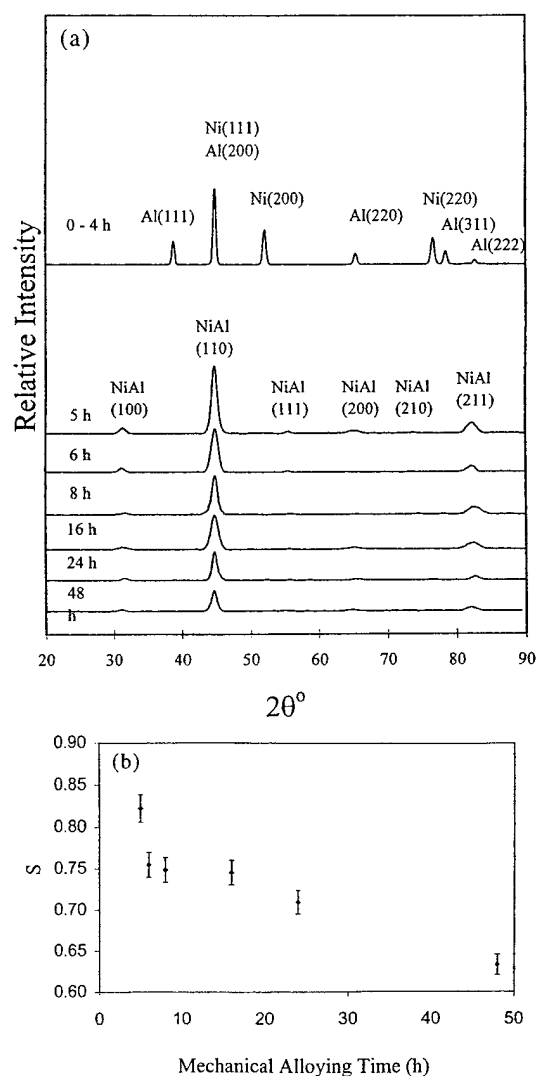


Fig. 1. (a) X-ray diffraction patterns of ball-milled NiAl powders showing the progress of mechanical alloying as a function of milling time; (b) plot of long-range-order parameter of mechanically alloyed NiAl alloy powders as a function of alloying time.

during milling. Further milling leads to increased deformation and work hardening, and the agglomerated powders then disintegrate into fragments producing finer particles of approximately  $0.7 \pm 0.3 \mu\text{m}$  in size [Figs 2(c)–(f)]. The particles shown in Figs 2(c)–(f) consist of nanosized crystallites.

The nanocrystalline structure of the powders was confirmed by TEM imaging, as shown in the dark field images in Figs 3(a)–(d). The representative electron diffraction pattern shown in Figs 3(a)–(d) confirms that NiAl was the only crystalline phase detected in the mechanically alloyed powders that received more than 5 h of ball milling. The size of the diffraction crystallites determined from TEM images of the ball-milled particles shows that the grain size decreases from approximately 50 nm to

Table 1. Contamination of Fe for NiAl alloyed for different times

Mechanical alloying time (h)	Fe (at. %)
8	0.35
16	0.22
24	0.84
48	3.21

10 nm with increasing milling time from 8 h to 48 h. The variation in average grain size (obtained from TEM micrographs) plotted as a function of alloying time is shown in Fig. 4.

Some iron contamination of the powders was observed by TEM analysis using EDS. The variation of Fe impurity concentration, determined via quantitative EDS analysis, was found to be approximately 0.8 at.% after 8 h milling, and increased to approximately 3.2 at.% with 48 h of mechanical alloying time, as shown in Table 1.

High resolution TEM (HRTEM) imaging of the mechanically alloyed powders was used to characterize the substructure of the crystallites. During the process of ball milling, large deformation is introduced, which can produce distorted regions, within subgrains, grain boundaries, and even across entire grains. The distorted regions are generated by an accumulation of dislocations from other regions. This sort of distortion is not commonly observed in coarse-grained materials. HRTEM imaging of the mechanically alloyed powders (milled for 24 h) revealed the presence of moiré fringes, stacking faults and distorted grains, as shown in Fig. 5(a). Figure 5(b), an enlarged image of region A in Fig. 5(a), shows the deformation substructure in the grains more clearly. Edge dislocations were also identified in the HRTEM images [circled in Fig. 5(b)], indicated by the presence of an extra half plane. The bands shown in the grains in Fig. 5(b), as well as in the grains in Fig. 5(a), have also been observed in other studies [18], and have been identified as shear bands. It has been reported that the formation of these shear bands is responsible for breakdown of the grains and generation of nanostructure during mechanical alloying.

### 3.2. Shock consolidation of mechanically alloyed nanocrystalline NiAl powders

Shock compaction of the mechanically alloyed nanocrystalline NiAl powders, performed at an impact velocity of 400 m/s (4–6 GPa peak pressure), produced single piece discs approximately 10 mm in diameter and 3 mm in thickness. The shock-densified NiAl powder compacts had both micro- and macro-cracks propagating radially outward from the compact axis, and were clearly observed from optical microscopy. The radial cracks in the compacts are produced due to two-dimensional radial wave-focusing effects. The densities of the shock-compacted NiAl powders mechanically alloyed for 16, 24 and 48 h were measured to be 4.81–4.88 g/

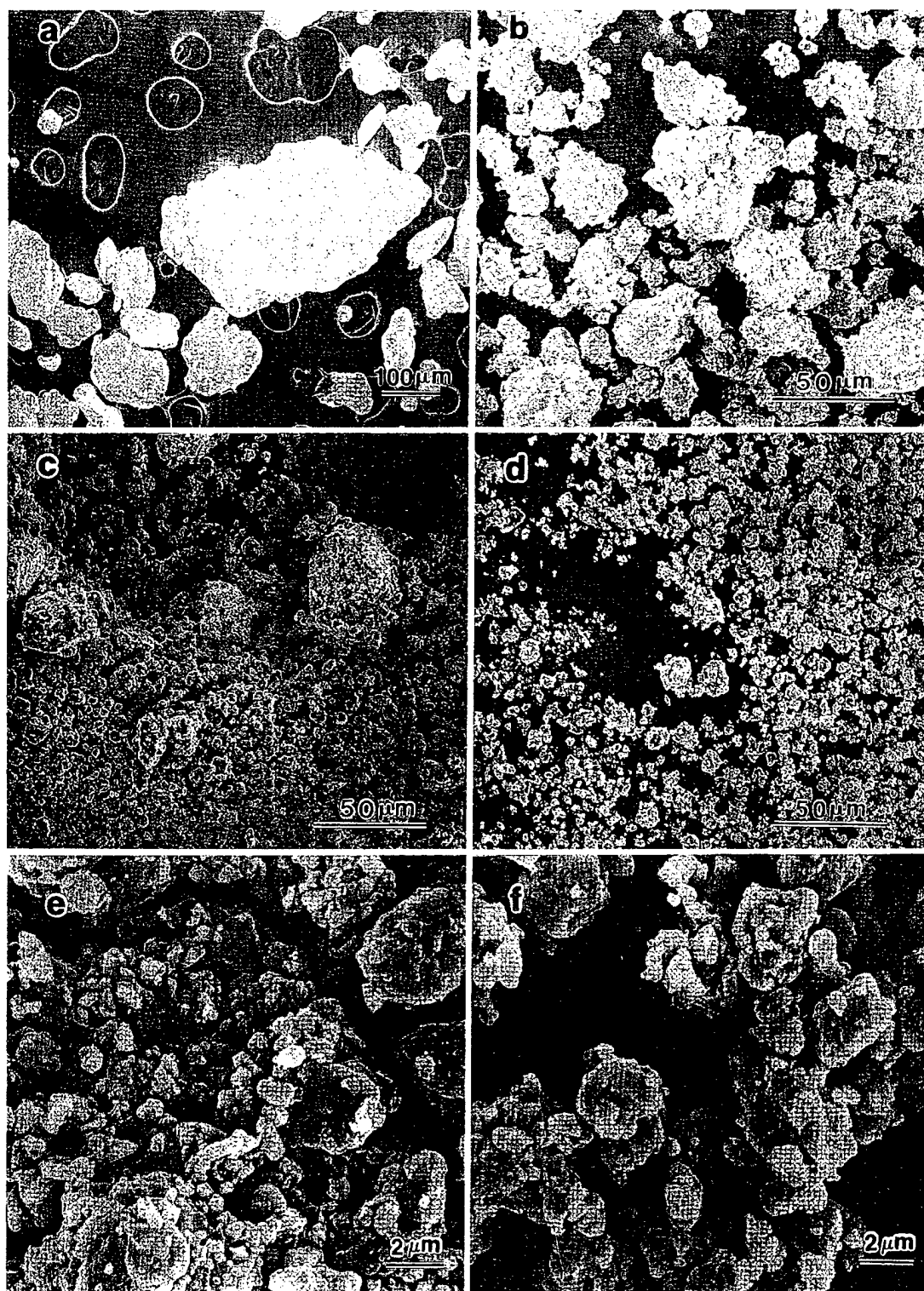


Fig. 2. Morphology of Ni-Al powders milled for (a) 2 h, (b) 5 h, (c) 8 h, (d) 16 h, (e) 24 h, and (f) 48 h.

$\text{cm}^3$ , which is approximately 83% of the theoretical maximum density of B2-NiAl, as shown in Table 2. Since nanocrystalline NiAl possesses a larger volume fraction of grain boundaries than conventional NiAl, its theoretical solid density value may be lower, and thus the relative density of the shock-

consolidated compacts may be somewhat higher. It should also be noted that the shock-consolidation conditions employed in this work were by no means optimized.

The X-ray diffraction patterns of the shock-consolidated compacts of powders alloyed for 16, 24

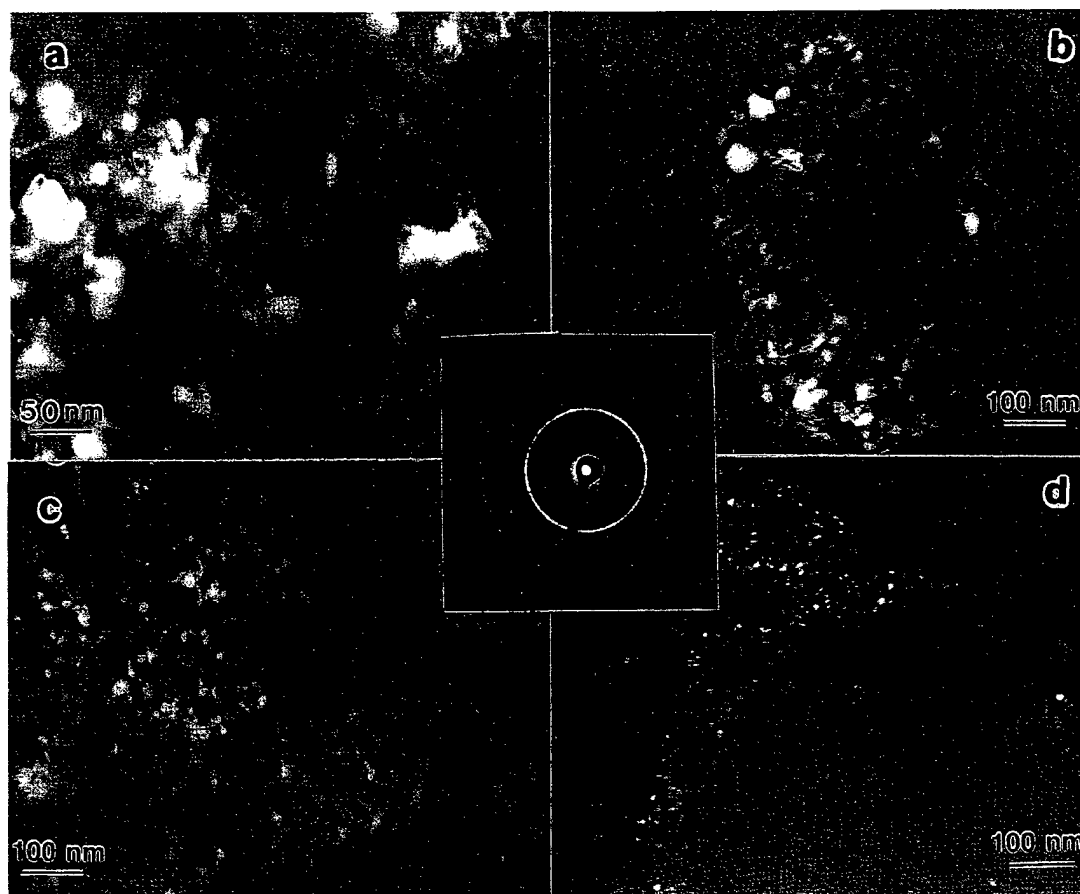


Fig. 3. Dark field images of nanocrystalline NiAl particles ball-milled for (a) 8 h, (b) 16 h, (c) 24 h, (d) 48 h and a typical electron diffraction pattern.

Table 2. Density of shock-compacted NiAl

Mechanical alloying time (h)	Measured density ( $\text{g/cm}^3$ )	Relative density (%)
16	4.88	83
24	4.87	83
48	4.81	82

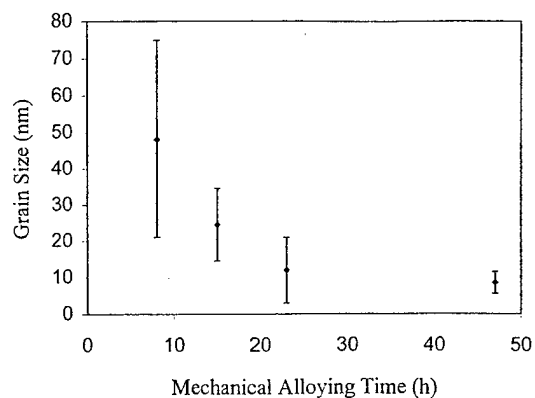


Fig. 4. Plot of average grain size varying as a function of mechanical alloying time.

and 48 h are shown in Fig. 6(a). It can be seen that the nanocrystalline NiAl phase of the mechanically alloyed powder was retained after shock compaction. The broadened diffraction patterns are attributed to the effects of the nanoscale crystallite size and retained residual stress. The long-range-order parameter ( $S$ ), calculated from these shock-densified samples and plotted as a function of milling time, is shown in Fig. 6(b). The degree of order for the shock-compacted samples is observed to remain practically unchanged relative to the mechanically alloyed powders shown in Fig. 1(b). However, for the hot pressing consolidation method employed by Pyo *et al.* [10] the degree of order was observed to increase, as compared to the mechanically alloyed sample, from 0.56 to 0.77. This has been explained as being due to the homogenization effect of hot pressing on the composition, in addition to the annealing of the defects.

An SEM micrograph of a cross-section of the shock-compacted sample, shown in Fig. 7(a), reveals the presence of voids, indicating that under the consolidation conditions used, complete densification is not achieved. The SEM micrograph of the fracture surface of the shock-compacted sample, shown in Fig. 7(b), reveals that the fracture occurs

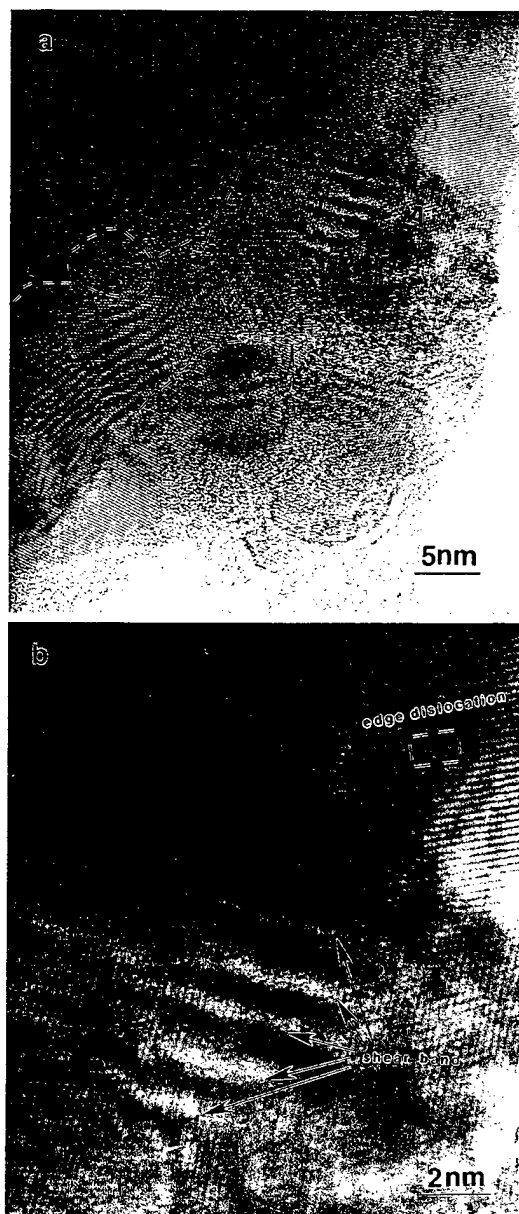


Fig. 5. High resolution images of mechanically alloyed (milled for 24 h) nanocrystalline NiAl particles: (a) grains are marked using dashed lines; (b) an enlarged image of region A from (a). Edge dislocation is marked.

along inter-particle boundary regions, leaving particles intact, confirming the lack of complete metallurgical bonding.

TEM analysis of shock-densified compacts of 16, 24 and 48 h alloyed powders, shown in Figs 8(a)–(c), reveals a distribution of diffracting crystallites, which is consistent with a reduction in size observed with mechanically alloyed powders as a function of milling time. Average grain sizes range from  $27 \pm 18$  nm at 16 h ball milling to  $9 \pm 6$  nm at 48 h ball milling. The representative electron diffraction pattern shown in the Fig. 8(d) confirms that the only phase present is crystalline B2-phase nickel-aluminide, in agreement with X-ray diffraction

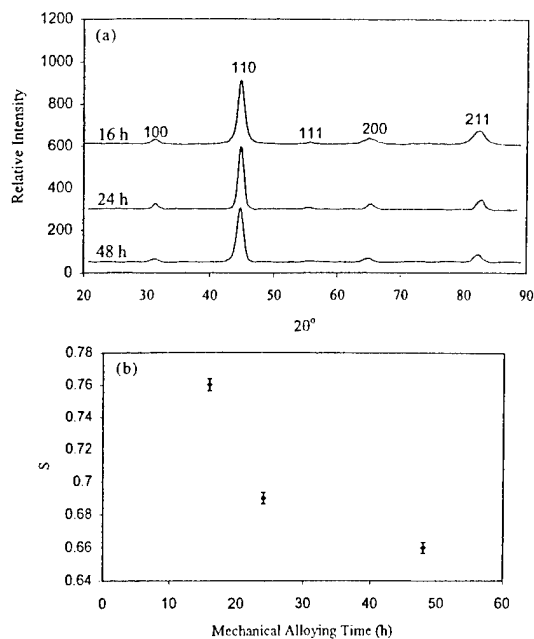


Fig. 6. (a) X-ray diffraction pattern of shock-consolidated NiAl; (b) plot of long-range parameter of shock-compacted NiAl alloy as a function of mechanical alloying time.

results. The TEM results, therefore, demonstrate that the nanocrystalline B2-NiAl microstructure is maintained in the shock-consolidated compacts.

HRTEM images shown in Figs 9(a) and (b), taken from the shock-consolidated NiAl (alloyed for 24 h), illustrate presence of moiré fringes, distorted grain regions, and shear bands in the interior of the grains, similar to that observed in the mechanically alloyed powders. Shear bands spanning across several grain dimensions are also observed as shown in Fig. 9(b). High magnification bright field TEM imaging in Figs 10(a)–(c) further revealed interesting deformation and shear band patterns. The shear bands in Fig. 10(a) are approximately 15 nm in thickness and those in Fig. 10(b) are approximately 100 nm thick. A multitude of even finer grains appears to be formed inside these shear band region, supporting the hypothesis that shear bands provide the mechanism for grain size refinement [18]. The TEM micrographs of the shock-consolidated specimen, shown in Figs 10(a) and (b), indicate preferred orientation of grains along the direction of band formation. The shear bands also include grains showing lattice rotation and flow. The shear bands in the shocked samples span several grain dimensions and are 100–500 nm long in contrast to those observed in the powders, which were 12 nm in length and confined to a single grain. Selected area diffraction patterns (SADP) taken from bands A and B, in Fig. 10(b), show the diffraction spots to be highly streaked indicating extensively strained crystallites. The formation of shear bands in the shock-densified compacts is con-

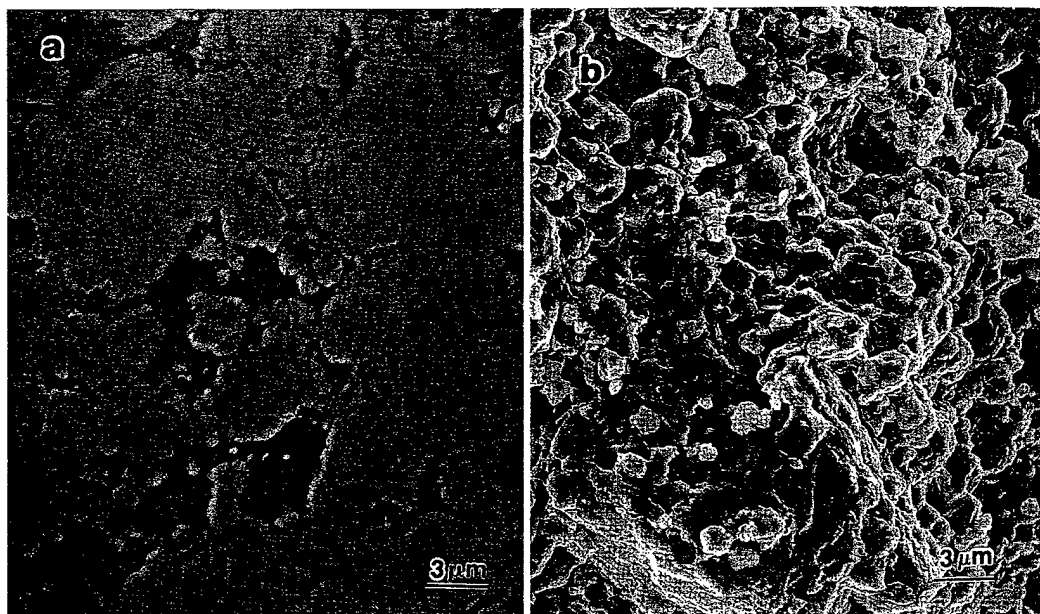


Fig. 7. SEM micrographs of shock-consolidated nanocrystalline NiAl: (a) cross-section, (b) fracture surface.

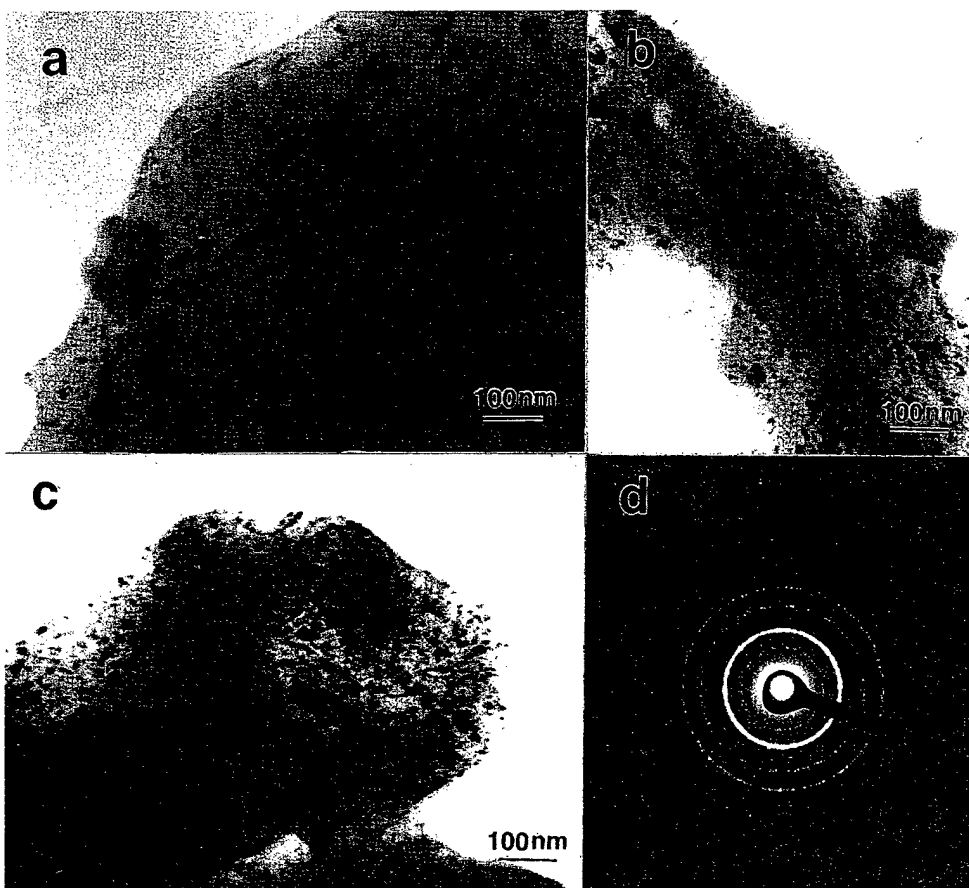


Fig. 8. TEM bright field images of shock-densified NiAl intermetallic compacts of (a) 16 h, (b) 24 h, (c) 48 h alloyed powders, and (d) a typical electron diffraction pattern.

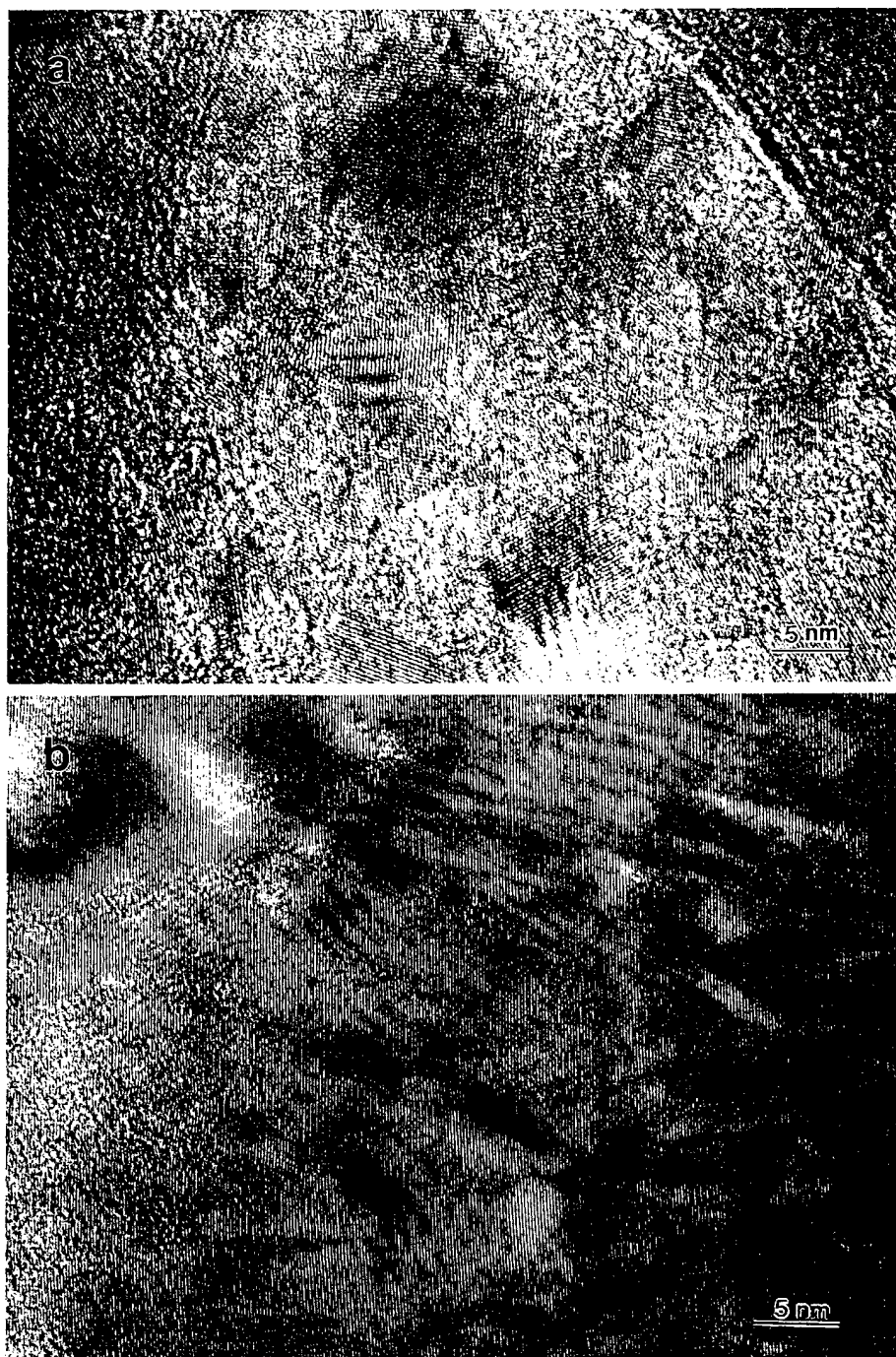


Fig. 9. HRTEM images of shock-consolidated NiAl compacts (alloyed for 24 h): (a) moiré fringes, distorted regions, and shear bands in the interior of grains are identified; (b) shear bands span several grain dimensions.

sidered to be induced by non-homogeneous deformation at high strain rate [19].

The results of Vickers microhardness measurements performed on metallurgically polished consolidated specimens are shown in Fig. 11. It is observed that the microhardness increases with increasing grain size refinement, from approximately 650 to 800 HV as average grain size changed

from  $27 \pm 18$  nm (with 16 h ball milling) to  $9 \pm 6$  nm (with 48 h ball milling). These measured microhardness values are much higher than the hardness of coarse-grained polycrystalline NiAl (330 HV reported by Haubold *et al.* [20]). Cracking was not observed around the indentations, which suggests that significant plastic deformation can be accommodated. This is similar to the results

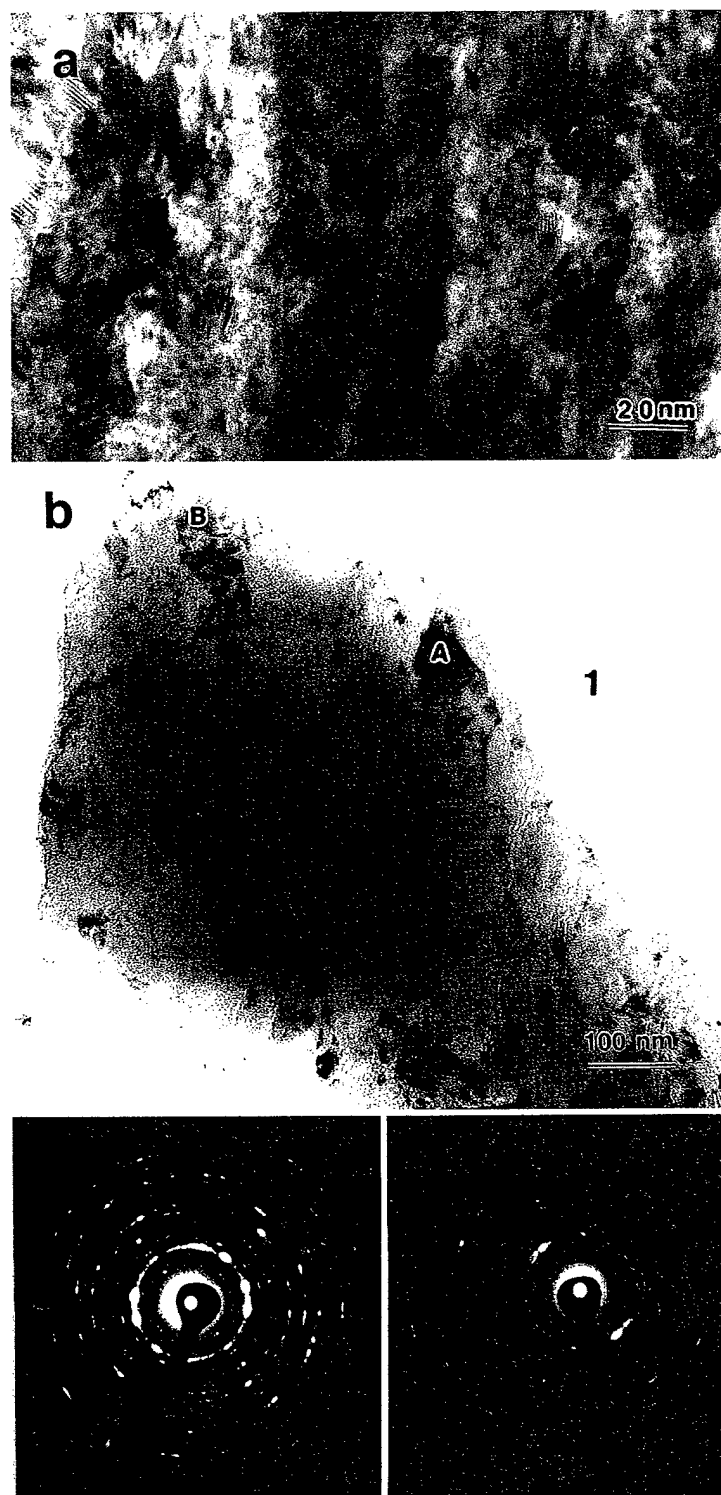


Fig. 10. TEM micrographs of interesting deformation and shear band patterns: (a) shear bands are about 15 nm in thickness; (b) shear bands are about 100 nm thick. SADPs from region A and B indicate extensively strained crystallites.

observed by Jain *et al.* [21] on nanocrystalline titanium–aluminide. The Vickers microhardness of nanocrystalline NiAl compacts has been measured to be in the range of 460–480 HV for sinter-forged

NiAl [8], 603 HV for vacuum hot-pressed NiAl and 564 HV for hot-pressed NiAl [10], 550–575 HV for NiAl with grain size of 0.5  $\mu\text{m}$ . The differences in the hardness values are associated with differences

in retained porosity as well as actual crystallite size. Haubold *et al.* [20] observed that 78% dense NiAl compacts prepared via inert gas condensation and subsequent compaction at 1 GPa showed a hardness of 540 HV. However, annealing of the porous compacts at 750°C for 5 h increased the density to 80% TMD and correspondingly the hardness changed to 723 HV. Further hot pressing (at 450°C) increased the hardness to 887 HV. Smith found 650–697 HV for mechanically milled and double-forged NiAl (grain size about  $72 \pm 41$  nm, 94% dense) [32, 33].

#### 4. DISCUSSION

##### 4.1. Synthesis of nanocrystalline B2-phase NiAl inter-metallic

Mechanical alloying is a high energy operation involving repeated welding, fracturing, and rewelding of powder particles. During mechanical alloying of NiAl, the powders agglomerate first, then disintegrate and reweld together at a fine scale. The repetitive welding and fracturing of the powders is a common mechanism for mechanical alloying of powders. In the case of a highly exothermic powder mixture, an abrupt self-sustained reaction can also occur resulting in alloy formation. The XRD patterns of the mechanically alloyed powders, shown in Fig. 1(a), indicate that synthesis of NiAl from elemental Ni and Al powders takes place by a solid state reaction. These results reveal a very abrupt reaction with no alloying up to 4 h of milling and complete alloying in 5 h. Increasing milling time results in further reduction of average crystallite size and microstrain storage, which is in agreement with early studies on mechanical alloying of NiAl. The synthesis of nanoscale crystallites of NiAl by mechanically alloying using ball milling has also been shown by other researchers [8, 9]. Atzmon demonstrated that NiAl is produced via ball milling as a result of an explosive, exothermic reaction, driven by a large heat of compound formation (–59 to –72 kJ/mol), instead of a gradual solid state layer diffusion [9]. With continued milling of the alloyed powders, the formation of shear bands results in regions of extensive deformation in which grains undergo further reduction in size and ultimately

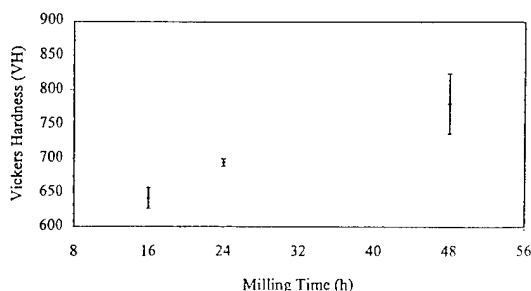


Fig. 11. Microhardness of shock-consolidated NiAl.

produce a nanocrystalline structure with extensive disorder.

Disordering by mechanical alloying is a common phenomenon for b.c.c. compounds. The degree of ordering obtained in mechanically alloyed intermetallics is a balance between disordering from the mechanical alloying process and thermally activated reordering. The ordering energy ( $\Delta H$ ) of an intermetallic compound can be approximately predicted from the enthalpies of formation by the Bragg-Williams theory [23] under the assumption of homogeneous disordering, and ignoring entropy effects.

$$\Delta H = \frac{1}{2} \epsilon H_f S^2. \quad (1)$$

In this equation,  $\epsilon$  is the pair exchange energy, which equals unity in this case,  $H_f$  is the formation energy, and  $S$  is the long-range-ordering parameter. The enthalpy of formation for NiAl has been reported to be approximately –59 kJ/mol, and recent studies report a value near –72 kJ/mol [5]. Compared to non-stoichiometric Ni–Al alloys, stoichiometric Ni–Al has the lowest formation enthalpy as shown by Fig. 12 [5, 24–27], which leads to the conclusion that stoichiometric NiAl has the greatest tendency to reorder, and that complete disordering of the B2 NiAl is energetically unfavorable. This may explain the finding that NiAl did not amorphize under the mechanical alloying conditions used in the present work, but did change to a metastable partially disordered state accompanied by a reduction in particle and crystallite sizes and microstrain storage. The enthalpy change associated with the reduction of the ordering parameter from 1 to 0.63 (milled for 48 h) is calculated to be –26.6 kJ/mol, using  $H_f = -72$  kJ/mol. The final state of mechanically alloyed NiAl will be a dynamic equilibrium between thermal reordering from the stored enthalpy and mechanical disordering introduced during ball milling.

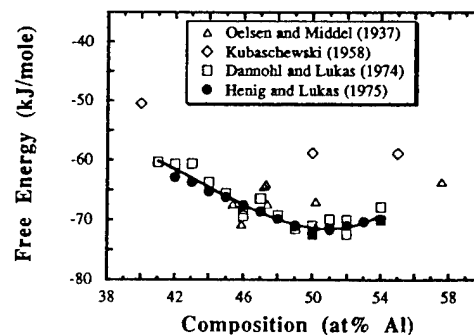


Fig. 12. The free energy of formation of NiAl as a function of composition [5]. Reprinted from *Acta Metallurgica et Materialia*, Volume 43, D. B. Miracle, "The physical and mechanical properties of NiAl", pp. 649–684, 1993, with permission from Elsevier Science Ltd.

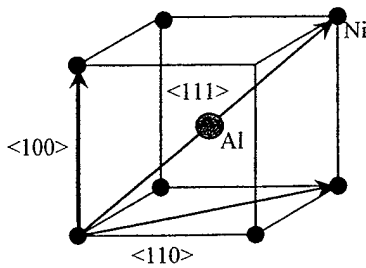


Fig. 13. B2 crystal structure.

The disorder generated by continued ball milling of Ni–Al alloy powders is a complex process, which involves destruction of chemical order, reduction of crystallite size, and an increase of lattice strain and defects. Aluminides with the B2 ordered structure (Fig. 13) can accommodate very high concentrations of vacancies in their lattice. In the present work, a large number of grain boundaries, distorted subgrains, distorted grain boundaries, grain boundary dislocations, and shear bands, in addition to Fe impurities, were detected in the mechanically alloyed powders.

The adiabatic temperature rise produced by plastic deformation under high strain is approximately:

$$\Delta T = \frac{\beta \sigma \varepsilon}{\rho C_v} \quad (2)$$

where  $\beta$  is a constant representing the fraction of plastic deformation work converted to heat, usually taken to be 0.9;  $\rho$  is the density of the material,  $\sigma$  is the plastic flow stress,  $\varepsilon$  is the plastic strain, and  $C_v$  is the heat capacity at constant volume. For the present work,  $\rho$  is assumed to be 5.9 g/cm<sup>3</sup>,  $C_v$  is approximately 500 J/kg·K,  $\sigma$  ranges between approximately 4 and 6 GPa,  $\varepsilon = \frac{4}{3} \ln \frac{\rho_1}{\rho_2}$  [28],  $\varepsilon$  is approximately 0.22 (with  $\rho_1$ , or initial density, and  $\rho_2$ , or shock density, respectively, being 4.13 and 4.88 g/cm<sup>3</sup>). Using equation (2), the maximum adiabatic temperature rise ( $\Delta T$ ) in the powder compacts is approximately 602 K, which is not sufficient to anneal the disorder in the shocked compacts.

#### 4.2. Dynamic recovery and shear band formation

The adiabatic shear bands (ASBs) observed in mechanically alloyed NiAl particles and in the shock-consolidated bulk samples indicate the occurrence of dynamic recovery. ASBs [29] are formed during high strain deformation processes, and are typically observed during shock compaction, machining, grinding, forging, and even rolling. They are characterized in appearance by bands spanning across grain boundaries without preferred crystallographic orientation and are planar in form, with planes which are related to the specimen geometry and the deformation process rather than to the crystallography of the deforming material [30]. Insufficient time for the heat associated with the deformation to dissipate from the deformed area

causes the heat to soften this localized region. If the strength loss is greater than the strength gain due to deformation hardening, localized deformation will become unsteady, and deformation by ASBs can occur. ASBs are typically observed in a compressive stress state rather than in a state of tension.

The crystal structure of B2–NiAl (as shown in Fig. 13) should have 48 slip systems. However, NiAl is only reported to deform by {110}<001> slip [31]. The three independent slip systems are not enough to accommodate uniform plastic deformation by dislocation movements. In the case of high strain generated from ball milling and shock compaction, once crystallographic slip commences at a grain where the condition for slipping is satisfied, the slip will propagate into adjacent grains by cooperative slip or cross-slip, leading to the formation of shear localization across several grains. No evidence of twinning was observed in either the ball-milled or shock-compacted NiAl, which seems in agreement with the theory that shear bands for b.c.c. metals are associated with deformation by slip alone [30].

#### 4.3. Strengthening mechanisms for shock-compacted NiAl intermetallic

In the present work, the hardness of NiAl was observed to increase with grain size refinement. The high hardness values obtained for shock-compacted mechanically alloyed nanostructured NiAl are attributed to the Hall–Petch strengthening effect [32]. The Hall–Petch strengthening mechanism is based on dislocation pile up at grain boundaries, or dislocation slip being impeded at grain boundaries. According to Jain and Christman [1], who studied the Fe–28Al–2Cr system, the grain boundary strengthening mechanism more appropriate for nanosized materials is the one developed by Li [33] based on dislocation generation from grain boundary ledges. According to this model, the macroscopic shear yield strength is expressed by the following equation:

$$\sigma = \sigma_0 + \alpha \mu b \left( \frac{8m}{\pi d} \right)^{\frac{1}{2}}$$

where  $\sigma_0$  is the shear flow strength for coarse-grained material,  $\alpha$  is a material constant,  $\mu$  is the shear modulus,  $m$  is the ledge density, and  $d$  is grain size. The yield stress is still inversely proportional to the square root of grain size. However, dislocation pile ups and grain boundary stress concentrations are not required. It is believed the grain boundary dislocations form a Taylor dislocation forest, which inhibits dislocation motion and provide strengthening.

Hardness measurements as a function of grain size in the nanocrystalline NiAl compacts of the present work were combined with a series of hardness measurements obtained by other

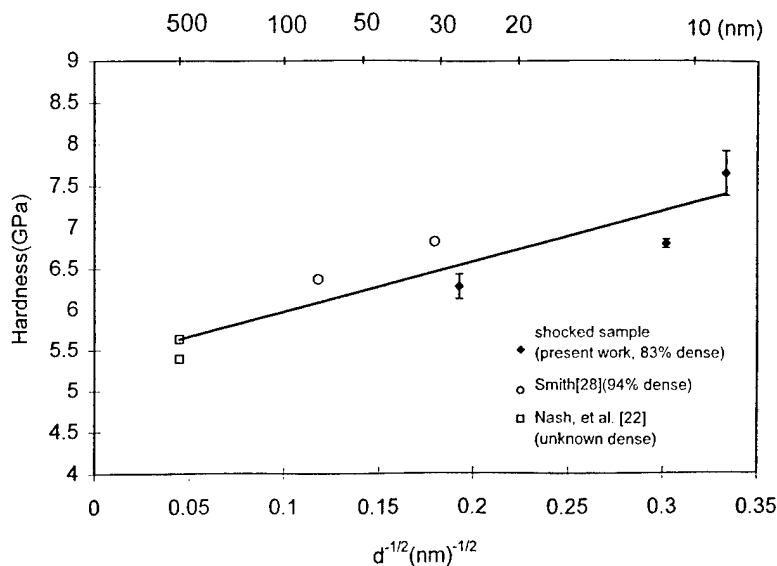


Fig. 14. Hall-Petch plot for NiAl based on present work on nanocrystalline NiAl compacts and data from Smith [32] and Nash *et al.* [22].

researchers [21,22,32]. As shown in the Hall-Petch plot in Fig. 14, a slope of approximately  $6.14 \text{ GPa}(\text{nm})^{1/2}$  is indicated for the combined data. Considering  $\alpha$  to be in the range of 0.2 to 0.4,  $b$  equal to 0.29, and  $\mu$  approximately 77 GPa [36], Hall-Petch slope of  $6.14 \text{ GPa}(\text{nm})^{1/2}$ , results in  $mb$  equal to 0.1–0.2, consistent with the ledge mechanism model [29]. Further experiments are currently in progress, in which the grain size will be changed via heat treatment to obtain a much better correlation of hardness with grain size. The results of these experiments will be published at a later time. The Hall-Petch behavior for NiAl with grain sizes ranging from 13  $\mu\text{m}$  to 70  $\mu\text{m}$  at room temperature has been studied by Nagpal and Baker [34], who found it to be independent of grain size within this grain size range. However, Bowman *et al.* [35] have observed yield strength dependence on grain size over the 10 to 200  $\mu\text{m}$  grain size range, a Hall-Petch slope of  $0.522 \text{ MPa}(\text{m})^{1/2}$  [or  $49.5 \text{ GPa}(\text{nm})^{1/2}$  for hardness]. Comparison of the Hall-Petch behavior in the nano- and micro-meter grain size range for Ni–Al indicates different slopes, but a similar strengthening mechanism.

The presence of Fe is also expected to contribute to the strengthening of NiAl, due to solution strengthening. In the present work iron was detected as a contaminant ( $\approx 0.35\text{--}3.2 \text{ at.}\%$ ), a result of the abrasion of the steel balls and vial. The Fe content increases with increasing ball milling time. The effects of iron on the mechanical and physical properties of NiAl have been investigated by others [37–41]. According to Hosoda [37] and Fu *et al.* [38], ternary elements such as iron have site preference in aluminides because of their electronic structure. It is also reported that the site position of Fe additions in Ni-rich NiAl depends

on both temperature and on the amount of iron. In Al-rich (i.e.  $x \geq 50$ ) alloys, the Fe atoms exist as substitutional antisite defects, i.e. the Fe atoms occupy Ni sublattices exclusively, which can hinder their detection during XRD and electron diffraction analysis. According to Lim *et al.* [39], the effect of iron doping is to stabilize the hardness of NiAl, and sometimes even increase the hardness at appropriate concentrations. Baker *et al.* [42] studied the lattice resistance ( $\sigma_0$ ) and the Hall-Petch slope ( $k$ ) as a function of aluminum, and found that both  $\sigma_0$  and  $k$  are the smallest at the stoichiometric composition and increase with decreasing aluminum concentration. Hence, the contamination of iron is expected to contribute to the solute strengthening of NiAl.

## 5. CONCLUSIONS

Stoichiometric nanocrystalline B2-phase NiAl intermetallic was synthesized by 5 h or more of mechanical alloying via ball milling, using an elemental mixture of Ni and Al powders with a ball-to-powder weight ratio of approximately 3.

The nanostructured NiAl powders were consolidated into bulk compacts with a relative density of 83%, using shock compaction at a peak pressure of 4–6 GPa.

The microstructure of both mechanically alloyed particles and shock-densified compacts exhibits defects that include distorted regions, dislocations, grain boundaries, subgrains, and shear bands. The disordering induced in both mechanically alloyed and shock-compacted material ranges between 0.82 and 0.63.

Inhomogeneous deformation by shear bands appears to be the cause of dynamic recovery occur-

ring during ball milling and shock consolidation of NiAl, resulting in grain size refinement.

The Vickers hardness of NiAl increases with grain size refinement, and was found to be significantly greater than conventional NiAl intermetallic alloys. The Hall-Petch strengthening (dominated by dislocation ledge mechanism), as well as solute strengthening (due to Fe contamination), appear to contribute to the very high hardness of the nanocrystalline NiAl compacts.

**Acknowledgements**—This material is based upon work supported by the National Science Foundation under Grant No. DMR 9624927, and also by the U.S. Army Research Office, Grant No. DAAG55-97-1-0163. The authors gratefully acknowledge the assistance from K. Vandersall and R. Russell with the shock compaction experiments.

## REFERENCES

- Jain, M. and Christman, T., *Acta mater.*, 1994, **42**, 1901.
- Siegel, R.W. and Fougere, G.E., *Mater. Res. Soc. Symp. Proc.*, 1995, **362**, 219.
- Chang, H., Hofer, J., Altstetter, C. and Averbach, R.S., *Mater. Sci. Engng*, 1992, **A153**, 676.
- Huang, B.-L. and Lavernia, E.J., *J. Mater. Syn. Proc.*, 1995, **3**, 1.
- Miracle, P.B., *Acta metall.*, 1993, **41**, 649.
- Davis, R.M., McDermott, B. and Koch, C.C., *Metall. Trans.*, 1988, **19A**, 2867.
- Fecht, H.J., Hellstern, E., Fu, Z. and Johnson, W.L., *Metall. Trans.*, 1990, **21A**, 2333.
- Smith, T.R., *Mater. Res. Soc. Symp. Proc.*, 1994, **350**, 219.
- Atzmon, M., *Phys. Rev. Lett.*, 1990, **64**, 487.
- Pyo, S.G., Kim, N.J. and Nash, P., *Mater. Sci. Engng*, 1994, **A181-A182**, 1169.
- Haff, G.R. and Schulson, E.M., *Metall. Trans.*, 1982, **13A**, 1563.
- Glade, S.C. and Thadhani, N.N., *Metall. Trans.*, 1995, **26A**, 2565.
- Gomdin, W.H., *Prog. Mater. Sci.*, 1986, **30**, 39-80.
- Thadhani, N.N. and Vreeland, T., *Acta mater.*, 1986, **34A**, 2323.
- Raybould, D., Morris, D.G. and Cooper, G.A., *J. Mater. Sci.*, 1979, **14**, 2523.
- Connihan, P., Nanostructured single-phase  $\text{Ti}_5\text{Si}_3$  produced by crystallization of mechanically amorphized and shock-densified powder compact. M.S. thesis, Georgia Institute of Technology, Atlanta, GA, 1997.
- JCPDS Card Index Number 2-1261, JCPDS International Center for Diffraction Data, 1986.
- Huang, J.Y., Yu, Y.D., Wu, Y.K., Li, D.X. and Ye, H.Q., *Acta mater.*, 1997, **45**, 113.
- Cottrell, A.H., *Dislocations and Plastic flow in Crystals*. Clarendon Press, Oxford, 1972, p. 162.
- Haubold, T., Bohn, R., Birringer, R. and Gleiter, H., *Mater. Sci. Engng*, 1992, **A153**, 679.
- Christman, T. and Jain, M., *Scripta metall.*, 1991, **25**, 767.
- Nash, P., Ur, U.C. and Dollar, M., in *Proc. 2nd Int. Conf. Struct. Appl. Mech. Alloying*. Vancouver, Canada, 1993. ASM International, Materials Park, OH, p. 192.
- Bragg, W.L. and Williams, E.J., *Proc. R. Soc. A*, 1935, **151**, 540.
- Kubaschewski, O., *Trans. Faraday Soc.*, 1958, **54**, 814.
- Oelsen, W. and Middel, W., *Mitt. K. Wilhelm-Inst. Eisenforsch.*, 1937, **19**, 1.
- Dannohl, H.D. and Lukas, H.L., *Z. Metallk.*, 1974, **65**, 642.
- Henig, E.T. and Lukas, H.L., *Z. Metallk.*, 1975, **66**, 98.
- Meyers, M.A., *Dynamic Behavior of Materials*. Wiley, New York, 1994, p. 388.
- Zener, C. and Hollomon, J.H., *J. appl. Phys.*, 1944, **15**, 22.
- Hatherly, M. and Malin, A.S., *Scripta metall.*, 1984, **18**, 449.
- Baker, I. and Schulson, E.M., *Metall. Trans.*, 1980, **15A**, 1129.
- Smith, T.R., *Mater. Res. Soc. Symp. Proc.*, 1995, **362**, 245.
- Li, J.C.M., *Trans. metall. Soc. A.I.M.E.*, 1963, **227**, 247.
- Nagpal, P. and Baker, I., *Scripta metall.*, 1990, **24**, 2381.
- Bowman, R.R., Noebe, R.D., Raj, S.V. and Locci, I.E., *Metall. Trans.*, 1992, **23A**, 1493.
- Viswanadham, R.K., Mannan, S.K., Kumar, K.S. and Wolfenden, A., *J. Mater. Sci. Lett.*, 1989, **8**, 409.
- Hosoda, H., Inoue, K. and Mishima, Y., *Mater. Res. Soc. Symp. Proc.*, 1995, **364**, 437.
- Fu, C.L. and Zou, J., *Mater. Res. Soc. Symp. Proc.*, 1995, **364**, 91.
- Lim, Y.J., Hong, K.T., Levit, V. and Kaufman, M.J., *Mater. Res. Soc. Symp. Proc.*, 1995, **364**, 273.
- Darolia, R., Lahrman, D.F. and Field, R.D., *Scripta metall.*, 1992, **26**, 1007.
- Liu, C.T., *Mater. Res. Soc. Symp. Proc.*, 1993, **288**, 3.
- Baker, I., Nagpal, P., Liu, F. and Munroe, P.R., *Acta mater.*, 1991, **39**, 1637.

## **APPENDIX A6 - PREPRINT**

X. Xu and N.N. Thadhani, "Shock Synthesis and Characterization of Ultrafine Grained NiTi Shape Memory Alloy," Scripta Materialia, 2001 (**in press**).

*{ACCEPTED FOR PUBLICATION IN SCRIPTA MATERILIA, 2001}*

## **SHOCK SYNTHESIS AND CHARACTERIZATION OF ULTRAFINE GRAINED NiTi SHAPE MEMORY ALLOY**

Xiao Xu and Naresh N. Thadhani  
School of Materials Science and Engineering  
Georgia Institute of Technology, Atlanta, GA 30332-0245

*Keywords:* Dynamic compaction; Martensitic transformation; Nickel-titanium alloys

### **Introduction**

Near-equiatomic NiTi alloys are considered to be the most important intermetallic compounds for applications based on shape-memory and super-elasticity effects. The shape memory effect observed in well-annealed equiatomic NiTi alloys is due to the martensitic transformation from an initial high-density B2-CsCl structure to a low-density monoclinic B19' structure [1,2]. A so-called "premartensitic transformation" into a commensurate phase (R phase) that appears prior to the main martensitic transformation, proceeding the route of B2→R→B19' [3-6], is often also observed in thermally cycled or thermo-mechanically treated NiTi alloys. The extent of shape recovery and the martensitic transformation characteristics have been shown to be influenced by grain size [7]; however, it is not known if these effects of grain size extend in the nano-scale range. Nanocrystalline alloys possess unique properties that materials with conventional grain sizes do not have, because of the large number of atoms residing at and near grain boundaries as the grain size approaches the nano regime. In particular, the mechanical, chemical, and physical properties are expected to be significantly enhanced for such nanocrystalline materials [8].

Mechanical fabrication techniques including equi-channel processing of bulk solids [9] and mechanical alloying of elemental powder mixtures [10] have been used for fabrication of ultra-fine grained and nanocrystalline materials. Shock compression has been employed to consolidate powders of ultrafine grained [11] as well as amorphous alloys [12], to retain the fine grain size or metastable non-crystalline state. In the case of amorphous powders, the compacts can also be subsequently devitrified to obtain nanocrystalline structure [13,14]. Devitrification is characterized by a nucleation and growth process, in which the crystallites nucleate randomly at favorable sites within the amorphous material and grow until they meet and consume all the material. During shock compaction, large numbers of defects are generated which provide sites for heterogeneous nucleation during post-shock devitrification. Consequently, the high density of nucleation sites results in impingement of crystallites that limits grain growth and permits retention of ultrafine grained or nanocrystalline structure [14]. In the present work, shock compaction was used to densify mechanically amorphized NiTi alloy prepared by ball-milling pre-alloyed nitinol powder. The compacts were subsequently annealed above the devitrification temperature to obtain a nanocrystalline alloy. The transformation characteristics of the nanocrystalline NiTi alloy were determined based on measurements of transformation temperatures using differential scanning calorimetry.

### Experimental

Nanocrystalline NiTi alloy was prepared by shock compaction of mechanically amorphized powder. Pre-alloyed nitinol powder with an average size of 10-37  $\mu\text{m}$  and composition of Ni=50.88 at%, Ti=49.12 at%, S=0.0002max and O=613 ppm was obtained from Special Metals in Kentucky. The powder was ball milled for 1/2 to 10 hours under argon atmosphere in the SPEX 8000 Mixer/mill (using the procedure recommended by Schwarz et al [15]), while the vial was cooled by dripping liquid nitrogen to prevent formation of deposits on the wall. Stainless steel vial and balls were used and the ball-to-powder weight ratio was 3-to-1.

Shock compaction was performed using a 3-capsule, plate-impact shock recovery fixture with an 80-mm diameter single stage gas-gun at a measured velocity of 508 m/s, to produce 10-mm diameter by 3-mm thick compacts. The powders were pressed in the capsules to about 60-63% of their theoretical maximum density (TMD), and capped with the plugs. Since the powders are subjected to 2-D radial wave-focusing effects, the shock loading conditions were numerically simulated with a P- $\alpha$  powder compaction model using AUTODYN-2D [16]. The bulk shock pressure was calculated based on impact of a 5-mm thick steel flyer plate on the powder (encapsulated in steel capsules) at the measured impact velocity. The pressure towards the back surface and axis was calculated to be slightly higher (8-9 GPa) than in the surrounding region close to the impact surface (5-7 GPa).

X-ray diffraction analysis of the shock densified and de-vitrified compacts was performed in the Philips 1800 APD, using Cu  $K\alpha$  radiation for the nanoscale structure characterization and phase identification. The density of the compacts following shock compaction was determined by the Archimedes water immersion method using a Fisher Scientific density measurement kit. Differential thermal analysis using Perkin-Elmer DTA7 was used to determine the devitrification

temperature and degree of amorphization of ball milled powders. Differential scanning calorimetry analysis was performed on the recovered compacts, using a Perkin-Elmer DSC Pyris 1, with flowing helium gas and a heating rate of 10°C/min, to determine the martensitic transformation and reversal temperatures, as well as the transformation energies. TEM characterization of the ball milled powders was done with a Hitachi HF2000 microscope.

## Results and Discussion

### 1. Synthesis and Characterization of Nanocrystalline NiTi Alloy

Ball milling of pre-alloyed nitinol powder over 1/2 to 10 hr time period, with liquid nitrogen dripping on the vial, showed evidence of mechanical amorphization during the first half-hour of ball milling. Figure 1(a) shows the XRD traces of the as-received nitinol powder, and the powder ball milled for 1/2, 3 and 10 hr. It can be seen that the diffraction peaks for all except the B2-(110) reflection begin to disappear within the first half hour of ball milling. Following ball milling for 10 hr, the powder appears fully amorphized. Bright field TEM imaging of ball milled powders showed presence of fine crystallites in an otherwise amorphous matrix, as illustrated by the diffuse rings in selected area diffraction pattern shown in Figure 1(b). The bright spots in the diffraction pattern correspond to the diffracting crystallites that are observed (in the TEM image) to be <40 nm size in the 3 hr powder.

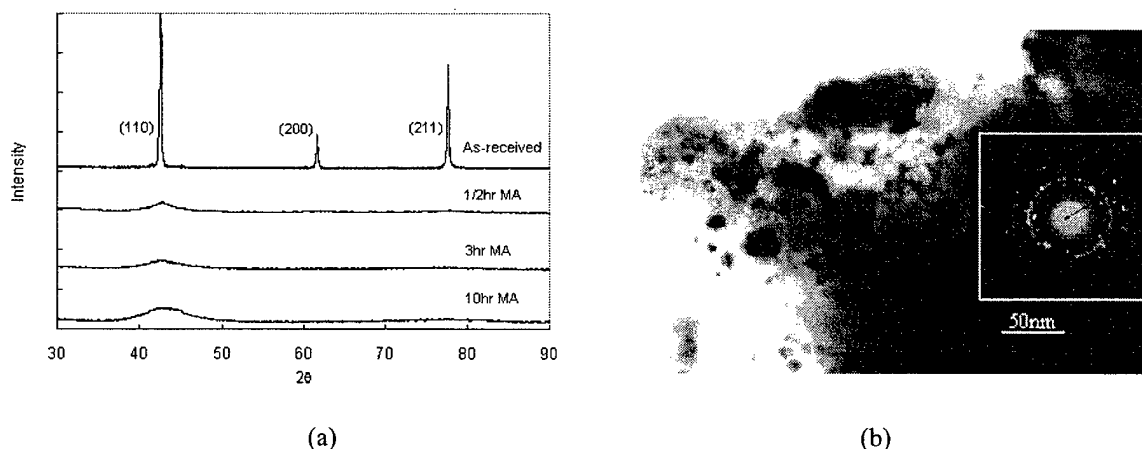


Figure 1. (a) XRD traces of nitinol powder ball milled for different duration and (b) TEM micrograph of 3hr MA nitinol powder

DTA analysis revealed that the devitrification temperature of the amorphous powders was 347±4°C. The heat evolved (based on exotherm area) was observed to increase with milling time, indicating a greater fraction of amorphous to crystalline phase transformation (and therefore, a greater degree of prior amorphization) in 10 hr MA powder than in 1/2 hr MA powder. Shock compaction was then performed on the 3 hr MA and 10 hr MA powders to obtain bulk samples of ~12 mm diameter by 3 mm thickness. The compact densities were measured to be 5.95-5.97 g/cc, which is ~92% T.M.D. of B2-NiTi. The actual density may be even higher, considering that the density in amorphous and nanocrystalline material is lower than its crystalline counterpart.

Following shock compaction, all compacts were annealed (de-vitrified) at 420°C and 30-minutes hold time to obtain nanocrystalline structure. XRD trace of the 3 hr MA compact shown in

Figure 2 illustrates the fully crystalline structure with broad peaks of B2-NiTi. XRD line-broadening analysis performed using the Williamson-Hall method [17], yielded an average crystallite size of  $58 \pm 10$  nm for the 3 hr MA compact, and  $44 \pm 7$  nm for 10 hr MA compact.

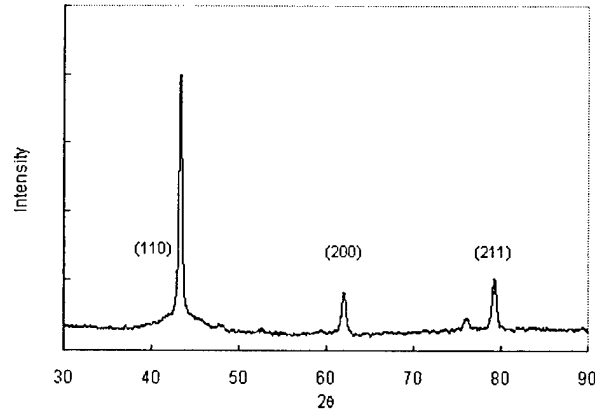


Figure 2. XRD trace of annealed 3hr MA compact, showing broadened peaks corresponding to nano-scale crystallite size of NiTi-B2 phase

## 2. Martensitic and Reversal Transformations in Nanocrystalline Nitinol Alloy

The transformation characteristics of nanocrystalline NiTi alloy were determined on the shock-densified and annealed (devitrified) compacts by measuring the martensitic transformation and reversal temperatures, as well as transformation energies, using a Perkin-Elmer Pyris 1 DSC. As illustrated in Figure 3(a), the as-received nitinol powder shows both R phase and martensitic transformations upon cooling and heating. In the shock-densified nitinol compacts (for both 3 hr and 10 hr MA powders), only a single martensitic transformation event is observed, upon cooling and heating, as shown in Figure 3(b). The corresponding transformation temperature values for each sample are listed in Table 1.

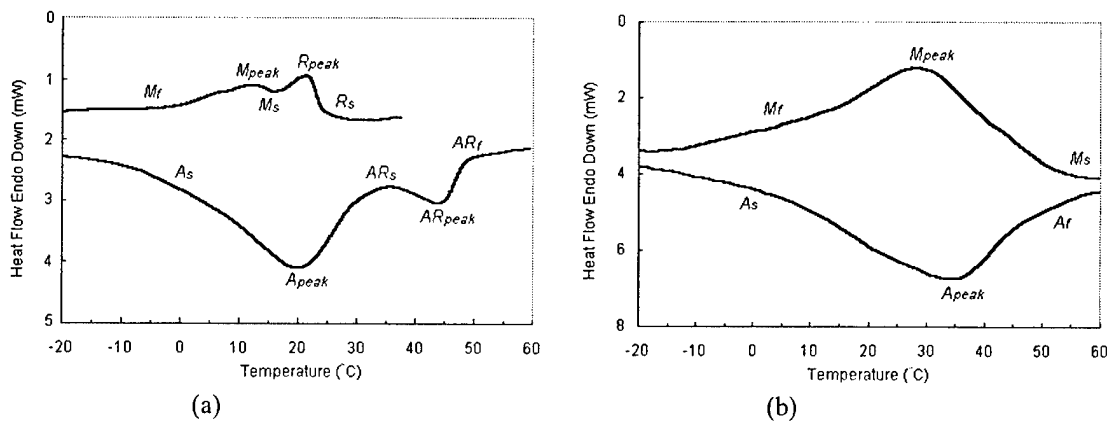


Figure 3. DSC traces showing transformation temperatures of (a) as-received powder and (b) annealed 10hr MA compacts

TABLE 1  
Transformation Temperatures (°C) of Nitinol Samples

		Cooling				Heating						
		$R_s$	$R_{peak}$	$M_s$	$M_{peak}$	$M_f$	$A_s$	$A_{peak}$	$AR_s$	$AR_{peak}$	$AR_f$	$A_f$
As-received powder	~40 $\mu$ m	29	24	17	13	0	7	23	42	49	55	--
Annealed 3hr MA compact	58nm	--	--	36	28	21	28	32	--	--	--	40
Annealed 10hr MA compact	44nm	--	--	48	30	14	6	34	--	--	--	56

It can be seen from Figure 3(b), that the peak temperature of the transformation from B2 to martensite is at 28-30°C, while the reverse martensitic transformation to B2 phase peaks at 32-34°C, for both shock-densified compacts. However, the  $M_s$  temperatures are different and are found to increase from 36°C in the 58 nm compact to 48°C in the 44 nm compact. Furthermore, the  $M_s$  and  $M_{peak}$  values of the nanocrystalline shock-densified compacts are significantly higher than those of the as-received nitinol powder.

The increase in  $M_s$  temperature in the nanocrystalline shock-densified samples can be attributed to the effect of decrease in grain size. Earlier work has reported an increase in  $M_s$  temperature with decreasing grain size in microcrystalline Ni<sub>48</sub>Ti<sub>42</sub> (weight percentage) alloy [7] and Cu-Zn-Al alloys [18,19]. Gil-Mur et al [7] showed that the increase in  $M_s$  with decreasing grain size was due to the thermodynamics of martensitic transformation being facilitated by local elastic energy. This local elastic energy arises due to the interaction between the newly formed martensitic plates and the grain boundaries. Since materials with smaller grains possess a larger portion of grain boundaries, it can be expected that there will be more local elastic energy between the martensitic plates and the grain boundaries. The elastic energy  $\Delta H_{el}$ , was thus calculated based on the method used in Gil-Mur et al's work [7]. Accordingly,  $\Delta H_{el} = \Delta H_{chem} - Q$ ; where,  $Q$  is the average heat measured during martensitic and reversal transformations, and  $\Delta H_{chem}$  is average chemical energy which can be calculated from  $\Delta H_{chem} = T_0 \Delta S$ , with  $T_0$  the equilibrium temperature estimated from the average of  $M_s$  and  $A_f$  [20], and  $\Delta S$  the average entropy change between martensitic and reversal transformations obtained by integration of the mean heat differential with respect to temperature. Table 2 lists the calculated values of  $T_0$ ,  $Q$ ,  $\Delta H_{chem}$  and  $\Delta H_{el}$  for the nitinol samples studied.

TABLE 2  
Energy Calculations of Nitinol Samples

	$T_0$ (K)	$Q$ (J/g)	$\Delta H_{chem}$ (J/g)	$\Delta H_{el}$ (J/g)
As-received powder	309	4.376	4.591	0.215
Annealed 3hr MA compact	311	1.413	1.454	0.041
Annealed 10hr MA compact	325	0.909	0.971	0.063

The calculated elastic energy for martensitic transformation in shock-densified B2-NiTi with nanocrystalline grain size is determined to be very small (negligible), in contrast to that for microcrystalline alloys. Hence, the elastic energy arising from the interaction between martensitic plates and grain boundaries, may not contributing to the increase in  $M_s$  temperature when grain size is in the nanometer range. In addition, the degree of anisotropy increases with decreasing grain size due to increasing number of different orientations of grains. This factor also contributes to greater internal stress, which may assist the martensitic transformation and result in a higher  $M_s$  temperature for NiTi alloy with nanocrystalline grain size. Or, alternatively, the increase in  $M_s$  temperature may be due to martensitic transformation in nanocrystalline NiTi alloy involving homogeneous nucleation due to effects of shock compression. Further work is currently in progress to establish the effect of nanocrystalline grain size as well as the role of shock-compaction on the transformation characteristics.

### **Conclusions**

Nanocrystalline NiTi alloy was obtained by shock compaction of mechanically amorphized nitinol powder (at a measured velocity of 508 m/s and calculated peak shock pressure of 5-9 GPa) and subsequent devitrification to fully crystallize the amorphous phase. With a reduced grain size in the nanometer range, the martensitic transformation start temperature was determined to increase with smaller grain size. This phenomenon may contribute to internal stress due to greater anisotropy, and possible homogeneous nucleation of martensitic phase, rather than the increase in elastic interaction energy between martensitic phases and grain boundaries, with decreasing grain size.

### **Acknowledgements**

The work reported in this article is funded by Army Research Office under Grant No.DAAG55-97-1-0163 (Dr. W. Mullins Program Monitor).

### **References**

1. W.J.Buehler and R.C.Wiley, Nickel Base Alloys, U.S.Patent No. 3,174,851.
2. C.M.Jackson, R.J.Wagner and R.J.Wasilewski, Report NASA-SR-5110 (1972).
3. S.Miyazaki et al., Supplement to J. de Phys. 43, C4-255 (1982).
4. W.B. Cross, A.H.Kariotis and F.J.Stimler, Report NASA-CR-1433 (1969).
5. F.E.Wang et al., J. Appl. Phys. 39, 2166 (1968).
6. G.P.Sandrock, A.J.Perkins and R.F.Hehemann, Metall. Trans. 2, 2769 (1971).
7. F.X.Gil-Mur, D.Rodriguez and J.A.Planell, Titanium'95: Sci. and Tech. 2399 (1995).
8. H.Gleiter, Prog. in Mater. Sci. 33, 223 (1989).
9. R.Z.Valiev, A.V.Korznikov and R.R.Mulyukov, Mater. Sci. Eng. A168, 141 (1993).
10. C.C.Koch and Y.S.Cho, Nanostructured Mater. 1, 207 (1992).
11. T.Christman and M.Jain, Scripta Metall. et Mater. 25, 767 (1991).
12. W.H.Gourdin, Prog. In Mater. Sci. 30, 39 (1986).
13. S.C.Glade and N.N.Thadhani, Metall. Mater. Trans. A. 26A, 2565 (1995).
14. P.J.Counihan, A.Crawford, and N.N.Thadhani, Mater. Sci. Eng. A. 267, 26 (1999).
15. R.B.Schwarz, R.R.Petrich and C.K.Saw, J. Non-Cryst. Solids 76, 281 (1985).
16. AUTODYN-2D, Century Dynamics Inc., Oakland, California (1995).
17. G.K.Williamson and W.H.Hall, Acta Metall. 1, 22 (1953).
18. J.M.Guilemany and F.J.Gil, Thermochem. Acta 167, 129 (1990).
19. F.J.Gil and J.M.Guilemany, Mater. Sci. Lett. (UK) 12, 6 (1993).
20. J.Ortin and A.Planes, Acta Metall. 36, 1873 (1988).